STOCHASTIC MODELLING OF RESIDUAL TROPOSPHERIC DELAYS

By

Hassan Elobeid Ibrahim
B.Eng. (Hons), Ryerson University, 2005

A thesis

presented to Ryerson University

in partial fulfillment of the

requirement for the degree of

Master of Applied Science

in the Program of

Civil Engineering

Toronto, Ontario, Canada, 2008

DECLARATION

I hereby declare that I am the sole author of the thesis. I authorize Ryerson University to lend this thesis to other institutions or individuals for the purpose of scholarly research.

---------- ---

Hassan Ibrahim

I further authorize Ryerson University to reproduce this thesis by photocopying or by other means, in total or part, at the request of other institutions or individuals for the purpose of scholarly research.

---------- -----

Hassan Ibrahim

ABSTRACT

Hassan Elobeid Ibrahim

STOCHASTIC MODELLING OF RESIDUAL TROPOSPHERIC DELAYS

MASc. of Civil Engineering, Ryerson University

2008

Real-time and near real-time precise point positioning (PPP) requires shorter solution convergence time. Residual tropospheric delay, which exists as a result of the limitations of current tropospheric correction models, is a limiting factor for fast PPP convergence.

To overcome the limitations of existing tropospheric models, we proposed a new approach. In this approach, the bulk of the tropospheric delay is accounted for using an empirical model, while the residual component is accounted for stochastically. The analysis of many daily tropospheric residuals data series for stations spanning North America shows that the residual component can be accounted for using an exponential cosine model. A random walk (RW) model was also developed and used along with the NOAA tropospheric corrections with Vienna Mapping Function 1. It is shown that the RW improved the accuracy of station coordinates within the PPP convergence time by a few centimetres.

ACKNOWLEDGMENT

I would like to express my sincere gratitude to my supervisor, Dr. Ahmed El-Rabbany for his continuous and unlimited support, encouragement, guidance, advice, and his wonderful friendship since I was an undergraduate student at Ryerson and through my graduate studies. I feel honoured to have had the opportunity to have him as my mentor and to be a member of his research team.

I am grateful to Pierre Héroux and Francois Lahaye from Geodetic Survey Division (GSD) of the Natural Research Canada (NRCan) for providing me with the GPSpace ® software source code. I further thank Francois for his continuous support and broadening my horizons through technical discussions.

I would also like to thank my friend Hamad Yousif from Ryerson University for providing me with Lagrange Interpolation code. My lab mates: Mohamed Elsobeiey, Abdulla Alnaqabi, and Amit Joshi were especially forthcoming with their valuable inputs and creative ideas and I would like to wish them luck for their future endeavours

Thanks to Seth Gutman and Susan Sahm from the National Oceanic and Atmospheric Administration (NOAA) Forecast Systems Laboratory (FSL), for providing me with the NOAA model software and access to the NOAA model grid files, without which my research would have been incomplete.

This research became possible by the partial funding provided by The Natural Sciences and Engineering Research Council of Canada (NSERC), The Geomatics for Informed Decisions (GEOIDE), The Network Centres of Excellence (NCE), The Ontario Graduate Scholarship for Science and Technology (OGSST), and The Ontario Graduate Scholarship (OGS).

And, lastly I would like to thank my wife, whose support and understanding got me through the toughest of times and gave me the courage to strive.

DEDICATION

To my parents, wife, and daughter

TABLE OF CONTENTS

DECLARATION.....ii

ABSTRACT.....iii

ACKNOWLEDGMENT.....iv

DEDICATION.....vi

TABLE OF CONTENTS.....vii

LIST OF TABLES.....xi

LIST OF FIGURES.....xii

1 INTRODUCTION.....1

1.1 Background on Thesis Work.....1

1.2 Problem Statement.....3

1.3 Research Objectives.....3

1.4 Thesis Outline.....4

1.5 Thesis Contributions.....5

2 OVERVIEW OF GPS.....6

2.1 Introduction.....6

2.2 GPS Space Segment.....7

2.3 Control Segment.....8

2.4 User Segment.....10

2.5 GPS Signal Structure.....11

2.6 GPS Errors and Biases.....12

2.6.1 Satellite Clock Error.....12

2.6.2 Receiver Clock Error.....13

2.6.3 Receiver Noise 13
2.6.4 Antenna Phase Center 14
2.6.5 GPS Ephemeris Errors 14
2.6.6 Ionospheric Delay 15
2.6.7 Tropospheric Delay 15
2.6.8 Multipath 16
2.6.9 Selective Availability 17
2.7 GPS Positioning Modes 18
2.7.1 Point Positioning 18
2.7.2 Relative Positioning 18
2.7.3 Precise Point Positioning (PPP) 19
3 TROPOSPHERIC DELAY MODELS 24
3.1 The Atmosphere 24
3.2 Neutral Atmosphere 26
3.3 Tropospheric Zenith Delay Modelling 27
3.3.1 Fundamentals 27
3.3.2 Empirical Hydrostatic and Wet Zenith Delay Models 29
3.4 The IGS Tropospheric Product 39
3.5 Mapping Functions 40
3.6 Tropospheric Delay Models in GPSpace 47
3.7 Implementation of NOAA Tropospheric Delay Corrections into GPSpace 48
4 STOCHASTIC CHARACTARICTICS OF RESIDUAL TROPOSPHERIC DELAY 49

4.1 Random Processes 50
4.1.1 Gauss-Markov (GM) Process 50
4.1.2 Periodic Random (PR) Process 52
4.1.3 Random Walk Process 52
4.2 Residual Tropospheric Delay Time Series 52
4.2.1 Data and Data Sources 52
4.2.2 Interpolation of ZTD Data 54
4.2.3 Residuals Zenith Total Tropospheric Delay 56
4.3 Linear Trend Removal 58
4.4 Assessment of Tropospheric Delay Models 58
4.5 Autocovariance Estimation 59
4.6 Empirical Autocovariance Models 60
4.7 Stochastic Modelling Results 60
4.7.1 Results for Saastamoinen- and Hopfield-Based Residuals 60
4.7.2 Results for NOAA-Based Residuals 64
4.7.3 Random Walk Modelling 74
5 RESULTS AND ANALYSIS 76
5.1 VMF1 vs. NMF 76
5.2 NOAA-VMF1 vs. Hopfield-NMF 79
5.3 Implementation of Random Walk Stochastic Model 81
6 CONCLUSIONS AND RECOMMENDATIONS 84
6.1 Conclusions 84
6.2 Recommendations for Future Research 86

REFERENCES **88**

APPENDIX I: DAILY RESIDUAL TROPOSPHERIC DELAY TIME SERIES FOR SAASTAMOINEN, HOPFIELD AND NOAA MODELS **92**

APPENDIX II: DAILY RESIDUAL TROPOSPHERIC DELAY TIME SERIES FOR NOAA MODEL **93**

APPENDIX III: ESTIMATED AUTOCOVARIANCE FUNCTION OF RESIDUAL TROPOSPHERIC DELAY **95**

APPENDIX IV: RESIDUAL TROPOSPHERIC DELAY OVER THE YEAR **97**

APPENDIX V: FITTING OF THE ESTIMATED AUTOCOVARIANCE FUNCTION **102**

APPENDIX VI: AUTOCOVARIANCE FUNCTION FITTING RMS **105**

APPENDIX VII: FLUNCTUATION OF MODELS' COEFFIEINETS **107**

APPENDIX VIII: MEAN OF AUTOCOVARIANCE FUNCTION EMPIRICAL MODELS' COEFFICIENTS **108**

APPENDIX IX: SAASTAMOINEN-, HOPFIELD- AND NOAA-BASED STOCHASTIC MODLES COEFFICIENTS MEAN **109**

APPENDIX X: DAILY MEAN OF RANDOM WALK NOISE RATE **111**

LIST OF TABLES

Table 3.1 Correction term B for the refined Saastamoinen model (Hofmann-Wellenhof et al., 2001) 31

Table 3.2 Correction term δR in meters for refined Saastamoinen model (Hofmann-Wellenhof et al., 2001) 32

Table 3.3 Coefficients of baby et al. model for wet zenith delay (Mendes, 1999) 34

Table 3.4 Niell Mapping Function coefficients (Leick, 2004) 42

Table 4.1 The ACF and correlation time for different order GM processes (Gelb, 1974) 51

Table 4.2 Correlation time based on first-order Gauss Markov for Saastamoinen- and Hopfield-based residuals (minutes) 63

Table 4.3 Coefficients mean and standard deviation of empirical ACF for Saastamoinen-based residuals 64

Table 4.4 Coefficients mean and standard deviation of empirical ACF models for Hopfield-based residuals 64

Table 4.5 Correlation time based on first-order Gauss Markov model for NOAA-based residuals (minutes) 72

Table 4.6 Coefficients mean and standard deviation of empirical ACF models for NOAA-based residuals 72

LIST OF FIGURES

Figure 2.1 GPS Segments (from AERO, 2008) 6

Figure 2.2 GPS Constellation (from AERO, 2008) 8

Figure 2.3 Positions of Master Control station and Monitor Stations (from NASA, 2008) 9

Figure 2.4 Multipath Acquisition (from GPS-System, 2008) 17

Figure 3.1 Atmosphere Regions (adapted from Leick, 1995) 25

Figure 3.2 Thickness of polytropic layers for the troposphere (adapted from Hofmann-Wellenhof et al., 2001) 35

Figure 3.3 Flowchart of NOAA tropospheric delay software processing (from Gutman et al., 2003) 39

Figure 4.1 IGS station distribution in North America (IGS, 2008) 53

Figure 4.2 Lagrange interpolation error for day 15 of 2006 at station MDO1 56

Figure 4.3 NOAA-, Hopfield -, and Saastamoinen-based residual ZTD before removing the linear trend 57

Figure 4.4 NOAA-, Hopfield -, and Saastamoinen-based residual ZTD after removing the linear trend 58

Figure 4.5 NOAA-, Saastamoinen-, and Hopfield-based residual ZTD at station ALGO on day 15 of 2006 59

Figure 4.6 Hopfield- and Saastamoinen-based residual ZTD before linear trend removed at station USNO on day 279 of 2006 61

Figure 4.7 Hopfield- and Saastamoinen-based residual ZTD after linear trend removed at station USNO on day 279 of 2006 61

Figure 4.8 Mean of model coefficients at station ALGO 62

Figure 4.9 Distribution of days processed for NOAA-based ZTD residuals at 10 stations over 2006 65

Figure 4.10 NOAA-based residual ZTD at 8 stations on day 20 of 2006 66

Figure 4.11 NOAA-based ZTD residual at station USNO over 2006 67

Figure 4.12 IGS new ZTD product at station ALGO over 2007 67

Figure 4.13 NOAA ZTD at station ALGO over 2007 68

Figure 4.14 Spike in NOAA ZTD at station USNO on day 75 of 2006 68

Figure 4.15 Autocovariance function of NOAA-based residual ZTD at 8 stations on day 20 of 2006 69

Figure 4.16 Fitting of ACF of NOAA-based residual at station NLIB on day 280 of 2006 70

Figure 4.17 Fitting RMS of NOAA-based residual at station JPLM over 2006 71

Figure 4.18 Fluctuations of coefficients of NOAA-based stochastic models at station FLIN over 2006 73

Figure 4.19 Mean of stochastic models' coefficients of the NOAA-based residual ZTD at different stations 74

Figure 4.20 Daily mean of RW noise rate at station ALGO over 2006 75

Figure 5.1 Improvement in X-coordinates when using VMF1 against NMF 77

Figure 5.2 Improvement in Y-coordinate estimates when using VMF1 against NMF 78

Figure 5.3 Improvements in Z-coordinate estimates when using VMF1 against NMF ... 78

Figure 5.4 Comparing Latitude estimates using NOAA and VMF1 one time and in another Hopfield and NMF at station PIE1 on day 15 of 2006 80

Figure 5.5 Comparing Longitude estimates using NOAA and VMF1 on time and in another Hopfield and NMF at station PIE1 on day 15 of 2006 80
Figure 5.6 Comparing height estimates using NOAA and VMF1 one time and in another Hopfield and NMF at station PIE1 on day 15 of 2006 81
Figure 5.7 Comparing Latitude estimate using RW stochastic for ZTD one time and in another for residual ZTD at station PIE1 on day 15 of 2006 82
Figure 5.8 Comparing Longitude estimates using RW stochastic model for ZWD one time and in another for residual ZTD at station PIE1 on day 15 of 2006 83
Figure 5.9 Comparing height estimates using RW stochastic model for ZWD one time and in another for residual ZTD at station PIE1 on day 15 of 2006 83
Figure I.1 NOAA-, Hopfield-, and Saastamoinen-based ZTD at station PRDS on day 201 of 2006 92
Figure II.1 NOAA-based residual ZTD at 10 stations on day 110 of 2006 93
Figure II.2 NOAA-based residual ZTD at 10 stations on day 202 of 2006 93
Figure II.3 NOAA-based residual ZTD at 9 stations on day 304 of 2006 94
Figure III.1 ACF of NOAA-based residual ZTD at 9 stations on day 110 of 2006 95
Figure III.2 ACF of NOAA-based residual ZTD at 10 stations on day 202 of 2006 95
Figure III.3 ACF of NOAA-based residual ZTD at 10 stations on day 304 of 2006 96
Figure IV.1 NOAA-based residual ZTD at station ALGO over 2006 97
Figure IV.2 NOAA-based residual ZTD at station AMC2 over 2006 97
Figure IV.3 NOAA-based residual ZTD at station FLIN over 2006 98
Figure IV.4 NOAA-based residual ZTD at station HLFX over 2006 98
Figure IV.5 NOAA-based residual ZTD at station HOLB over 2006 99

Figure IV.6 NOAA-based residual ZTD at station JPLM over 2006 99
Figure IV.7 NOAA-based residual ZTD at station MDO1 over 2006 100
..... 100
Figure IV.8 NOAA-based residual ZTD at station NLIB over 2006 100
Figure IV.9 NOAA-based residual ZTD at station PRDS over 2006 101
Figure V.1 Fitting of autocovariance of NOAA-based residual at station JPLM on day 215 of 2006 102
Figure V.2 Fitting of ACF of Hopfield-based residual at station JPLM on day 215 of 2006 102
Figure V.3 Fitting of ACF of Hopfield-based residual at station MDO1 on day 45 of 2006 103
Figure V.4 Fitting of ACF of Saastamoinen-based residual at station USNO on day 180 of 2006 103
Figure V.5 Fitting of ACF of NOAA-based residual at station HLFX on day 104 of 2006 104
Figure V.6 Fitting of ACF of NOAA-based residual at station HLFX on day 158 of 2006 104
Figure VI.1 Fitting RMS of NOAA-based residual at station AMC2 over 2006 105
Figure VI.2 Fitting RMS of NOAA-based residual at station FLIN over 2006 105
Figure VI.3 Fitting RMS of NOAA-based residual at station FLIN over 2006 106
Figure VII.1 Fluctuation of models coefficients at HOLB for NOAA based residual ... 107
Figure VII.2 Fluctuation of models coefficients at NLIB for NOAA based residual 107

Figure VIII.1 Mean of stochastic models' coefficients of the Saastamoinen-based residual ZTD at different stations 108
Figure VIII.2 Mean of stochastic models' coefficients of the Hopfield-based residual ZTD at different stations 108
Figure IX.1 Model coefficients mean of coefficient at station JPLM 109
Figure IX.2 Model coefficients mean of coefficient at station MDO1 109
Figure IX.3 Model coefficients mean of coefficient at station PRDS 110
Figure IX.4 Model coefficients mean of coefficient at station USNO 110
Figure X.1 Daily mean random walk noise rate at station AMC2 over 2006 111
Figure X.2 Daily mean random walk noise rate at station FLIN over 2006 111
Figure X.3 Daily mean random walk noise rate at station HLFX over 2006 112
Figure X.4 Daily mean random walk noise rate at station HOLB over 2006 112
Figure X.5 Daily mean random walk noise rate at station JPLM over 2006 113
Figure X.6 Daily mean random walk noise rate at station MDO1 over 2006 113
Figure X.7 Daily mean random walk noise rate at station NLIB over 2006 114
Figure X.8 Daily mean random walk noise rate at station PRDS over 2006 114
Figure X.9 Daily mean random walk noise rate at station USNO over 2006 115

1 INTRODUCTION

1.1 Background on Thesis Work

GPS is affected by a number of errors and biases, including receiver clock error, multipath, tropospheric and ionospheric delays, and satellite clock and orbital errors. Tropospheric delay represents one of the dominant errors after the availability of precise orbits and clock products from the International GNSS Service (IGS). The tropospheric delay correction is essential for unbiased GPS coordinate solutions (Vollath et al., 2003). Tropospheric delay occurs as a result of the transmission of the GPS signal through the troposphere, the lower layer of the atmosphere. It delays the carrier phase and the code measurements equally for signals with a frequency of 15 GHZ or less (Hay and Wong, 2000).

Tropospheric delay consists of two components: the first component is the hydrostatic or dry portion and the second component is the wet portion. The hydrostatic component represents about 90% of the total tropospheric delay, while the wet component represents the remaining 10%. The hydrostatic component can be estimated very precisely with empirical models (El-Rabbany, 2006), while the wet component is hard to estimate precisely with empirical models. This is because it is not easy to measure the water content along the path of the GPS signal.

In GPS Precise Point Positioning (PPP), tropospheric path delay is typically expressed as a product of unknown total zenith path delay (ZPD), which is modelled as a random walk process noise, and a known mapping function relating slant path delay to ZPD (Kouba and Héroux, 2001). Alternatively, the tropospheric path delay can be modelled as a function of zenith hydrostatic and wet delays, with two different mapping functions, plus tropospheric gradients (Gao et al., 2004). In such a case, the zenith wet delay and two gradient coefficients are to be estimated. Unfortunately, unlike the zenith hydrostatic delay, the zenith wet delay is highly correlated with the total zenith tropospheric delay (Gutman at al., 2003), which in turn is known to be highly correlated with the height component of the station coordinates (Kouba, 2003). The existence of such high cross-correlation as well as the temporal correlation of the tropospheric path delay slows down the convergence of the PPP solution. More recently, a number of regional and local monitoring networks have been established to generate tropospheric corrections. Among them is the NOAA tropospheric correction model, which incorporates GPS observations into numerical weather prediction (NWP) models (Gutman at al., 2003). The model is distributed as a 2-D grid file, which is updated hourly and contains the zenith tropospheric delay over the U.S. and surrounding regions (including a large portion of Canada). Unfortunately, however, although the model improved the positioning solution compared to the empirical tropospheric delay models (e.g., Saastamoinen and Hopfield models), a residual tropospheric error component remains unmodelled. Such a residual error component is found to be temporally correlated, which may slow down the conversion of the PPP solution.

1.2 Problem Statement

Although empirical tropospheric delay models account for the hydrostatic tropospheric delay with very high accuracy, a good model for the wet part is still not available. This is mainly because of the strong temporal and spatial variations of the water content in the atmosphere, which is difficult to measure along the GPS signal path. As a result, a residual tropospheric error component remains unmodelled. The temporal and spatial correlation of the unmodelled residual may slow down the conversion of the PPP solution.

This research attempts to model the residual tropospheric delay stochastically by utilizing ZTD residuals of three tropospheric delay models, namely the Saastamoinen, Hopfield and NOAA, are stochastically modelled. The data used in this research was obtained for stations spanning a region covering United States and part of Canada. Therefore, stochastic models obtained in this research will be valid for the region covering the United States and most of the populated portion of Canada.

1.3 Research Objectives

The main objective of this research is to improve tropospheric delay modelling, which not only speeds up the GPS solution convergence but also improves the GPS positioning accuracy. This will be fulfilled through a number of tasks as follows:

1 Estimation of total zenith tropospheric delay using empirical and NWP-based tropospheric delay models.

2 Retrieval of total zenith tropospheric delay residuals using the new IGS tropospheric product as a reference.

3 Estimation of autocovariance functions using daily time series of total zenith residuals tropospheric delay.

4 Fitting of the estimated autocovariance functions to empirical covariance models.

5 Assessing the obtained stochastic models for seasonal and geographical location variations.

6 Estimation of the random walk noise rate of NOAA-based zenith total residual tropospheric delay.

1.4 Thesis Outline

Chapter 1 presents a background on thesis work, problem statement, research objectives, thesis outlines and thesis contributions.

Chapter 2 provides an overview of the GPS in section 1. In section 2, the GPS biases and errors are discussed. In section three, the GPS point and relative positioning, and Precise Point Positioning (PPP) are presented.

Chapter 3 provides an overview of the various atmospheric layers. It also discusses a number of widely-used empirical tropospheric delay models with emphasis on the NOAA tropospheric delay model. This chapter ends with a discussion on common tropospheric mapping functions, including the recently-developed Vienna mapping function 1 (VMF1).

Chapter 4 presents the theory of stochastic modelling, and the stochastic modelling methodology followed in this thesis to model the residual tropospheric delay for each of the Saastamoinen-, Hopfield-, and NOAA-based residuals. Results of the stochastic models for the Saastamoinen- Hopfield-, and the NOAA-based residual tropospheric delay are also presented.

Chapter 5 presents the tropospheric models and the mapping functions available in the GPSpace PPP software. Also this chapter shows how the NOAA tropospheric delay correction is implemented into the GPSpace software. The results of implementation of the NOAA tropospheric delays into the GPSpace software and its effect on the positioning accuracy are also given in this chapter.

In chapter 6, the main conclusions, as extracted from the obtained results and performed analysis, are presented. In addition, recommendations for future research work are given.

1.5 Thesis Contributions

The contributions of this research can be summarized as:

- to develop stochastic models for residual tropospheric delays.
- to develop regional stochastic models for NOAA-based residual tropospheric delay that can be applied for all of United States and the southern part of Canada.
- to implement the NOAA-based model into the GPSpace software.
- to improve the accuracy of point positioning.
- to shorten the PPP solution convergence time.

2 OVERVIEW OF GPS

2.1 Introduction

The GPS is a satellite-based navigation system that was originally developed by the United States Department of Defence (DOD) in early 1970s. GPS was initially developed as a military system to fulfill military requirements but later made available for civilian use and has since become a dual-use system that is accessible by both military and civilian users (El-Rabbany, 2006). GPS provides continuous positioning and timing information worldwide no matter the weather condition is. Since GPS serves an unlimited number of users, both civilian and military, it has been designed as a one-way passive system where the users can only receive satellite signals (El-Rabbany, 2006). GPS consists of three segments: the space segment, the control segment and the user segment (Hofmann-Wellenhof et al., 2001) (Figure 2.1).

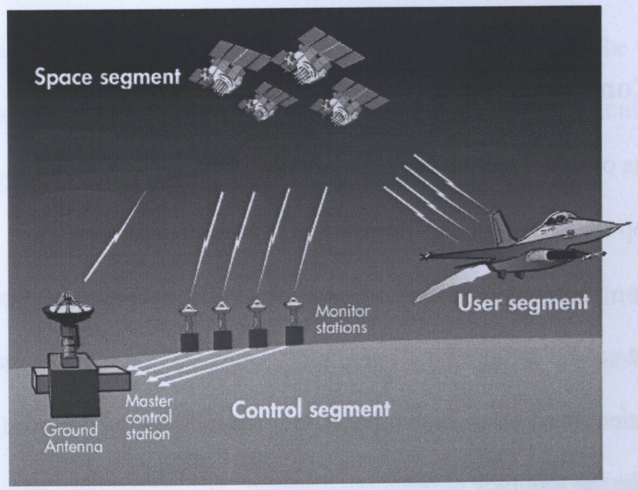

Figure 2.1 GPS Segments (from AERO, 2008)

2.2 GPS Space Segment

The GPS constellation consisted nominally of 24 operational satellites, arranged so that there were four satellites placed in each of the six orbital planes (Figure 2.2) to ensure continuous worldwide coverage, originally known as the initial operational capability (IOC) that was completed in July of 1993, which was officially confirmed on December 8, 1993 (El-Rabbany, 2006).

With this constellation geometry, four to ten GPS satellites are visible anywhere in the world at any given time if an elevation angle of 10° is considered. The GPS satellite orbits are nearly circular (an elliptical shape with a maximum eccentricity of about 0.01) with an inclination of 55° to the equator. The semi-major axis of the GPS orbit is 26578 kilometres (Xu, 2007). This has a corresponding GPS orbital period of approximately 12 sidereal hours (~ 11 hours, 58 minutes).

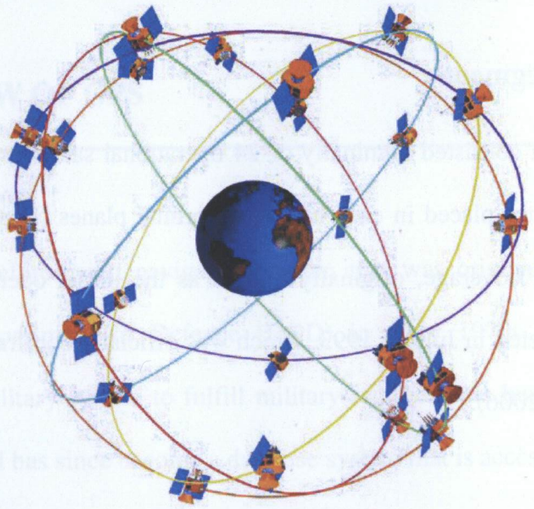

Figure 2.2 GPS Constellation (from AERO, 2008)

The current GPS constellation as of May 21, 2008 consists of 14 Block IIA, 12 Block II-R and six Block IIR-M satellites (USNO, 2008). This makes the total number of operational GPS satellites to be 32. All GPS satellites are equipped with on-board atomic clocks: Block II/IIA satellite has two Cesium (Cs) and two Rubidium (Rb) clocks while Block IIR satellite has three Rubidium atomic clocks (USNO, 2008). At any given time only one clock is selected to provide the frequency and the timing requirements for the generation of the GPS signal. The stability of these clocks is in the order of 1 to 2 parts in 10^{13} over a period of one day (El-Rabbany, 2006).

2.3 Control Segment

The GPS control segment consists of a master control station, monitor stations, and ground control antennas. The control segment is considered the 'brain' of the GPS. The

control segment manages all the satellites with the primary task being the tracking of the GPS satellites in order to determine and predict satellite positions, system integrity, behaviour of the on-board atomic clocks, atmospheric correction, satellite almanac and other considerations. The control segment also ensures that the satellite orbits and atomic clocks remain within acceptable limits.

Currently there are 12 GPS monitor stations (El-Rabbany, 2006) (Figure 2.3) located in Colorado Springs, Hawaii, Kwajalein, Diego Garcia, Washington, DC (the US Naval Observatory), United Kingdom (Hermitage), Ecuador (Quito), Argentina (Buenos Aires), Ascension Island, Bahrain (Manama), and Australia (Adelaide). These stations' locations are selected in such a way that each GPS satellite can be tracked by at least ten monitor stations (El-Rabbany, 2006). Each of the monitor stations collects GPS observations that are transmitted to the master control station for processing to produce predicted satellite navigation data (El-Rabbany, 2006). This predicted data is then transmitted to the GPS satellites through the GPS ground antennas.

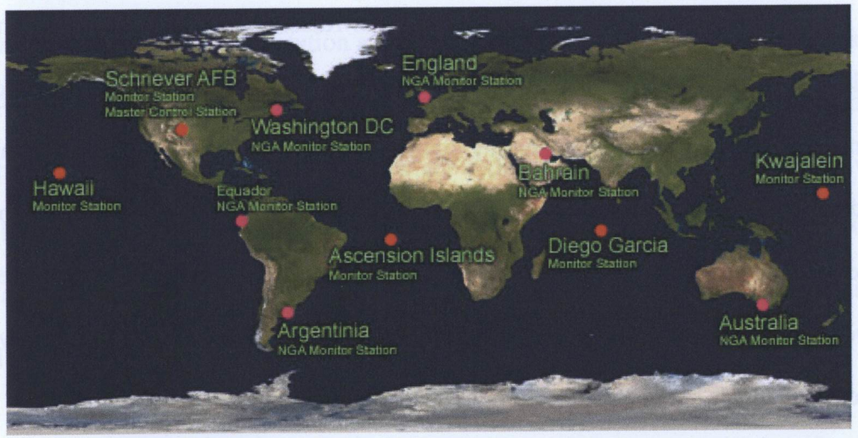

Figure 2.3 Positions of Master Control station and Monitor Stations (from NASA, 2008)

The master control station, which is located at Falcon Air Force Base in Colorado Springs, Colorado, is responsible for the overall management of the remote monitoring and transmission sites. Being the centre for support operations, it calculates any position or clock errors for each individual satellite based on information received from the monitor stations and then 'orders' the appropriate ground antennas to relay the requisite corrective information back to that satellite.

There are four ground antennas located at the same site as the monitor stations at Ascension Island, Diego Garcia, Kwajalein, and Cape Canaveral, Florida. The ground antennas are capable to transmit commands and data to the satellites and receive telemetry and ranging data from the satellites (Hofmann-Wellenhof et al., 2007).

2.4 User Segment

The GPS user segment includes all the equipment of the military personnel and civilian users of the system who receive GPS signals (El-Rabbany, 2006). These equipments include a GPS receiver and antenna. In general the GPS receiver is composed of an antenna, receiver processor and a highly stable clock. It may also include a display for providing position and speed information. A receiver is usually characterized by its number of channels. The receiver number of channels indicates how many satellites the receiver can monitor simultaneously. Now-a-days most of GPS receivers have typical number of channels between 9 and 12 (El-Rabbany, 2006).

2.5 GPS Signal Structure

Each GPS satellite transmits a signal that consists of five components. These components are two sine waves (also known as frequency carriers), two digital codes and a navigation message. The two carrier frequencies generated on the L-band are L1 with a frequency of 1575.42 MHz and a wavelength of 19 centimetres, and L2 with a frequency of 1227.60 MHz and a wavelength of 24.4 centimetres. All GPS satellites transmit the same carrier frequencies while the codes transmitted are unique to each satellite. The coarse acquisition-code (C/A-code) used to be transmitted on the L1 frequency only. Each satellite transmits a unique C/A-code that enables the GPS receiver to identify which satellite is transmitting a particular code (El-Rabbany, 2006). This code has a repeating duration of 1 millisecond consisting of a stream of 1,023 binary digits. The precision-code (P-code) is transmitted on both the L1 and L2 frequencies. Each satellite is assigned a unique one-week segment of the precision code that is 266 days in overall length. The duration of one bit is 0.1 microseconds.

As a result of the GPS modernization a civilian L2 (L2C) is transmitted by all Block IIR-M GPS satellites and later design satellites. L2C consist of two codes, civilian moderate length code (CM), which is 10230-bit in length and is repeating every 20 ms, and civilian long length code (CL), which is 767250-bit in length and is repeating every 1500 ms. Also as part of the GPS modernization, Block IIF GPS satellite will transmit a safety-of-life civilian signal (L5) of a frequency 1176.45 MHz.

2.6 GPS Errors and Biases

There are several types of random and systematic errors that affect the accuracy of GPS observations. These errors can be classified as errors related to the GPS satellite, errors related to the GPS receiver and errors related to the atmosphere (El-Rabbany, 2006).

The satellite related-errors include satellite clock errors, ephemeris errors and the effect of selective availability. Receiver related-errors include receiver clock errors, receiver noise, antenna phase center variation and multipath. The atmospheric errors include the effect of the ionosphere and the troposphere on the GPS signal. The following paragraphs discuss some of these errors mentioned above.

2.6.1 Satellite Clock Error

GPS satellites are equipped with atomic clocks (Cesium and/or Rubidium clocks). Although, atomic clocks are highly accurate, but they are not perfect. As we mentioned earlier GPS satellite clocks have a stability that is about 1 to 2 part in 10^{13} over the period of one day. This range of stability means the satellite clock error is in the range of 8.64 to 17.28 ns (El-Rabbany, 2006). One nanosecond of inaccuracy in a satellite clock results in about 30 centimetres of error in measuring the distance to that satellite. The satellite clock error can cause about 2.59 m to 5.18 m in the range between the satellite and the receiver. To resolve the satellite clock drifts, they are continuously monitored by ground stations and compared with the master control clock systems that are combinations of more than 10 very accurate atomic clocks. The errors and drifts of the satellites' clock are calculated and included in the messages that are transmitted by the satellites. In

computing the distance to the satellites, GPS receivers subtract the satellite clock errors from the reported transmit time to come up with the signal travel time.

2.6.2 Receiver Clock Error

Similar to GPS satellite clock errors, any error in the GPS receiver clock causes inaccuracy in distance between the satellite and the receiver antennas phase centres. However, the receiver clock error is much larger compared to the satellite clock error. GPS receivers are normally equipped with inaccurate clocks (crystal clocks) compared to satellite clocks. One way to remove the receiver clock error is applying the technique of differencing between satellites. Another way of dealing with the GPS receiver error is considering it as one of the estimation process unknowns (El-Rabbany, 2006).

2.6.3 Receiver Noise

GPS Receivers introduce some noise that affects the GPS observation. The level of the receiver noise varies from receiver to another. The noise comes essentially from the thermal noise, which is caused by the electrons movement within the receiver's parts (Teunissen and Kelusberg, 1998). In high quality receivers, however, the receiver noise is negligible (less than one millimetre) for carrier phase and a few centimetres for code phase (El-Rabbany, 2006).

2.6.4 Antenna Phase Center

Depending on the satellite azimuth and elevation, and the intensity of the GPS signal, the GPS signal may reaches the receiver antenna at different points. This point is called the antenna phase center. Generally, in each antenna the phase center is different from the geometrical center. The antenna phase center variation causes an error in the range between the receiver and the satellite. The size of this error is on the order of a few centimetres (El-Rabbany, 2006), and it depends on the antenna's type.

2.6.5 GPS Ephemeris Errors

Ephemeris errors are the error in the GPS satellite position. Ephemeris errors are caused as a result of the limitations in modelling the forces acting onto the GPS satellite (El-Rabbany, 2006). The GPS signal contains information about the ephemeris (orbital position) errors. The broadcast ephemerides for a satellite are the predictions of the current satellite position and velocity as determined by the Master Control Station. These are uploaded to the GPS satellites, and transmitted to the user receiver in the navigation message. The precise ephemeris are post-processed values derived by, for example, the International GNSS Service (IGS), and available to users post-mission via the Internet. Ephemeris errors are due to the slight deviations in the orbital paths of the satellites from their predicted path. Broadcast ephemeris errors are typically at the few metre level, while the precise ephemeris errors are at the decimetre-level. Ephemeris errors are largely mitigated by differential correction (in DGPS Positioning) or in double-differenced observables (formed from carrier phase measurements) when the receivers are not up to a few tens of kilometres apart. In very high precision applications and/or

where the baseline lengths are hundreds or thousands of kilometres, residual Ephemeris Errors may limit the accuracy of the baseline solution.

2.6.6 Ionospheric Delay

The ionosphere is the upper layer of the atmosphere. It extends from 50 km to 1000 km altitudes. As a result of ionizing radiation, electrons exist in the ionosphere layer (Teunissen and Kelusberg, 1998). Electrons exist in quantities that enough to influence the GPS signal. The ionosphere is a dispersive medium, it has two effects on the GPS signal, it bends the signal and changes its speed. The bending effect can be neglected since it causes negligible range error, however, it causes significant range error, it speeds up the carrier phase beyond the speed of light while it delay the code (El-Rabbany, 2006). In general, ionospheric delay can reach range error of the order of 5m to 15m, and up to 150m with severe solar activity. One way of delaying with ionospheric delay error is using empirical models such as Klobuchar, the coefficients of which are included with navigation message.

2.6.7 Tropospheric Delay

The troposphere is the lower layer of the Earth atmosphere, which contains water vapours, is known as the troposphere. The thickness of the troposphere layer is not constant. It reaches 9 and 16 km over the poles and the equator respectively (Teunissen and Kleusberg, 1998). The effect of the troposphere on the GPS signal is that it delays both the carrier and the code. Tropospheric delay can be separated into its wet and dry

components. As we mentioned earlier in chapter one, the dry component represents about 90% of the delay and can be predicted with a fairly high degree of accuracy using mathematical models (El-Rabbany, 2006). The wet component of the troposphere delay depends on the amount of water vapour that the GPS signal has to pass through on its way to the receiver. The effects of the troposphere cannot be removed using dual frequency systems. It was found that using default meteorological data (1010 mb for atmospheric pressure, 20°C for temperature, and 50% for relative humidity) for the most part gives satisfactory results (El-Rabbany, 2006).

2.6.8 Multipath

Multipath is one of the major error sources that affect the GPS signal. Multipath happens when the signal coming from the satellite antenna reaches the receiver antenna through different paths (see Figure 2.4), as a result of signal refection by surrounding objects to the antenna. The direct signal and the reflected signals interfere at the antenna.

Multipath has effect on both carrier phase and code measurements, but its error size is larger on the pseudorange measurements compared to the carrier measurements (El-Rabbany, 2006). Multipath can cause a size of error of a quarter of a cycle on the carrier measurements. The error on the pseudorange can reach tens of meters (El-Rabbany, 2006).

There is no a good general model to deal with Multipath yet, as the satellite-reflector-antenna geometry hard to predict (El-Rabbany, 2006). Methods of mitigating multipath

can be categories as: hardware and software solutions as well as careful site selection (Xia, 2004).

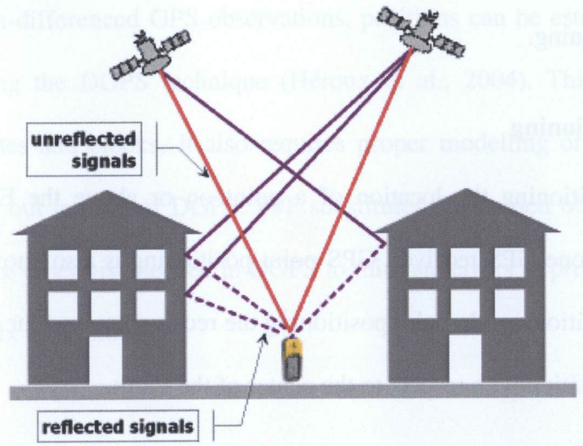

Figure 2.4 Multipath Acquisition (from GPS-System, 2008)

2.6.9 Selective Availability

Originally, GPS designed in a way that accuracy of using the P-code receiver for real-time autonomouous positioning to be superior compared to the C/A code, however, the obtained accuracy of the two receivers was almost the same (El-Rabbany). To keep the C/A code receiver accuracy degraded the US DoD had introduced the so-called selective availability (SA) on satellite Block II (El-Rabbany, 2006). This intentional degradation or SA was implemented to introduce types of errors: the first one is delta error; it results from dithering the satellite clocks. The second one is called epsilon error; it is an additional slowly varying orbital error (El-Rabbany, 2006). SA was active from March 25, 1990 till May 2nd, 2000. When the SA was on the nominal horizontal and vertical errors can reach up to 100m and 156m respectively.

2.7 GPS Positioning Modes

There are two ways to acquire position using GPS: point positioning and relative, or differential, positioning.

2.7.1 Point Positioning

In GPS point positioning the location of a point on or above the Earth's surface is obtained by using one GPS receiver. GPS point positioning is also known as standalone or autonomous positioning. In point positioning the receiver tracks four or more satellites to determine its position with respect to the center of the Earth.

2.7.2 Relative Positioning

A more accurate positioning mode compared to point positioning is relative positioning. Relative or differential GPS (DGPS) positioning is the determination of a point position using two GPS receivers. In DGPS the two GPS receivers simultaneously receive signals from the same satellites. One of the two receivers is static at a known position point and selected as a reference. The other receiver is placed at the point where we need to determine the position.

Differential GPS (DGPS) techniques have been applied for precise positioning since they cancel out receiver and satellite clock errors and reduce significantly the atmospheric delay (Héroux et al., 2004). Although DGPS can provide precise positioning, it has some disadvantages: limited applicability area, accuracy depends on baseline length, errors in reference station coordinates can be propagated to the newly established stations, and an increase in logistical complications.

2.7.3 Precise Point Positioning (PPP)

An alternative approach to DGPS is Precise Point Positioning (PPP). Using the PPP technique with un-differenced GPS observations, positions can be estimated logistically simpler than using the DGPS technique (Héroux et al., 2004). This requires precise satellite coordinates and clocks. It also requires proper modelling or estimation of the errors that cancel out in case of DGPS. PPP substitutes the burden of carrying out field procedures that are otherwise needed in DGPS to mitigate errors to proper modelling and estimation (Héroux et al., 2004).

In this chapter, the theory of PPP is reviewed with emphasis on tropospheric delay modelling and estimation within the GPSpace PPP software. GPSpace software has been developed by the Geodetic Survey Division (GSD) of National Research Canada (NRCan) for PPP. Section four of chapter three, , will give a detailed explanation of the contributions made by the present study to the GPSpace software to accommodate for the NOAA tropospheric corrections.

The point positioning ionospheric-free linear combinations of dual-frequency GPS pseudorange (P) and carrier-phase observations (Φ) can be expressed in terms of station coordinates, clock, troposphere, and ambiguity parameters as (Kouba, 2000):

$$l_p = \rho + C(dt - dT) + T_r + \varepsilon_p \quad \textbf{(2.1)}$$

$$l_\Phi = \rho + c(dt - dT) + T_r + N * \lambda + \varepsilon_\Phi \quad \textbf{(2.2)}$$

where:

l_p is the ionosphere-free combination of L1 and L2 pseudoranges (2.54P1-1.54P2),

l_Φ is the ionosphere-free combination of L1 and L2 carrier-phases (2.54Φ1-1.54Φ2),

dt is the station clock offset from GPS time,

dT is the satellite clock offset from GPS time,

c is vacuum speed of light,

T_r is the signal path delay due to the neutral atmosphere (mainly the troposphere),

λ is the carrier wave length of L1 or L2,

N is the ambiguity of the carrier-phase ionosphere-free linear combination, and

ε_p and ε_Φ are the relevant measurement noise components, including multipath and biases residuals,

ρ is the geometrical range between the satellite and the receiver antennas' phase centres it expressed as:

$$\rho = \sqrt{(X_s - x)^2 + (Y_s - y)^2 + (Z_s - z)^2}$$

where (X_s, Y_s, Z_s) are the satellite antenna phase centre coordinates and (x, y, z) are the receiver antenna phase centre coordinates.

Substituting the tropospheric path delay T_r by the *ZPD* multiplied by a mapping function and removing the satellite clock error (dT) in (2.1) and (2.2) gives the following equations:

$$f_p = \rho + C * dt + M * ZPD + \varepsilon_p - P = 0 \qquad \textbf{(2.3)}$$

$$f_\Phi = \rho + C * dt + M * ZPD + N * \lambda + \varepsilon_\Phi - \Phi = 0 \qquad \textbf{(2.4)}$$

Linearization of observation equations (2.3) and (2.4) a round a-priori parameters and observations (X_0,) become, in matrix form:

$$A\delta + W - V = 0 \qquad \textbf{(2.5)}$$

Where A is the design matrix, δ is the vector of corrections to the unknown parameters X, $W = f(X^0,)$ is the misclosure vector and V is the vector of residuals.

The design matrix is formed by taking the partial derivatives of four types of parameters: station coordinates (x, y, z), receiver clock error (dt), tropospheric *ZPD* and non-integer carrier phase ambiguities (N)

$$A = \begin{bmatrix} \frac{\partial f(X,_P)}{\partial X_x} & \frac{\partial f(X,_P)}{\partial X_y} & \frac{\partial f(X,_P)}{\partial X_z} & \frac{\partial f(X,_P)}{\partial X_{dt}} & \frac{\partial f(X,_P)}{\partial X_{zpd}} & \frac{\partial f(X,_P)}{\partial X_{N^j_{(j=1,nsat)}}} \\ \frac{\partial f(X,_\Phi)}{\partial X_x} & \frac{\partial f(X,_\Phi)}{\partial X_y} & \frac{\partial f(X,_\Phi)}{\partial X_z} & \frac{\partial f(X,_\Phi)}{\partial X_{dt}} & \frac{\partial f(X,_\Phi)}{\partial X_{zpd}} & \frac{\partial f(X,_\Phi)}{\partial X_{N^j_{(j=1,nsat)}}} \end{bmatrix} \qquad \textbf{(2.6)}$$

where

$$\frac{\partial f}{\partial X_x} = \frac{x - X_s}{\rho}, \quad \frac{\partial f}{\partial X_y} = \frac{y - Y_s}{\rho}, \quad \frac{\partial f}{\partial X_z} = \frac{z - Z_s}{\rho}, \quad \frac{\partial f}{\partial X_{dt}} = c, \quad \frac{\partial f}{\partial X_{zpd}} = M, \quad \frac{\partial f}{\partial X_{N^j_{(j=1,nsat)}}} = 0 \text{ or } 1$$

$$X = \begin{bmatrix} x \\ y \\ z \\ dt \\ zpd \\ N^j_{(j=1,nsat)} \end{bmatrix}$$

The least-squares solution is defined as:

$$\delta = -(P_{X^0} + A^T PA)^{-1} A^T PW \qquad \textbf{(2.7)}$$

Where, P is a-priori weighted constraints to the unknown parameters. Therefore, the estimated parameters are:

$$\hat{X} = X^0 + \delta$$

And the covariance matrix is:

$$C_{\hat{x}} = P_{\hat{x}}^{-1} = \left(P_{X^0} + A^T PA\right)^{-1} \tag{2.8}$$

Adjustment Procedure

In the GPSpace estimation process there are four types of parameters which need to be estimated: station coordinates receiver clock, tropospheric zenith path delay, and carrier-phase ambiguities. The adjustment procedure is a sequential filter that adjusts to different user environment or dynamics. The adjustment considers the variation of the parameters between observations epochs and accounts for it by using stochastic process for these variations.

For the adjustment a-priori estimate for the parameter is needed. For epoch *i* the initial parameter estimate can be given as:

$$X_i^0 = \hat{X}_{i-1} \tag{2.9}$$

The propagated covariance matrix at epoch *i* is given as:

$$C_{\hat{x}_i} = C_{\hat{x}_{i-1}} + C\varepsilon_{\Delta t} \tag{2.10}$$

where

$$C\varepsilon_{\Delta t} = \begin{bmatrix} C\varepsilon(x)_{\Delta t} & 0 & 0 & 0 & 0 & 0 \\ 0 & C\varepsilon(y)_{\Delta t} & 0 & 0 & 0 & 0 \\ 0 & 0 & C\varepsilon(z)_{\Delta t} & 0 & 0 & 0 \\ 0 & 0 & 0 & C\varepsilon(dt)_{\Delta t} & 0 & 0 \\ 0 & 0 & 0 & 0 & C\varepsilon(zpd)_{\Delta t} & 0 \\ 0 & 0 & 0 & 0 & 0 & C\varepsilon\left(N^j_{(j=1,nsat)}\right)_{\Delta t} \end{bmatrix} \tag{2.11}$$

Since the carrier-phase ambiguities are constant over time, therefore,

$C\varepsilon\left(N^j_{(j=1,nsat)}\right)_{\Delta t} = 0$. Also, in static mode the station coordinates are constant, and as a consequence $C\varepsilon(x)_{\Delta t} = C\varepsilon(y)_{\Delta t} = C\varepsilon(y)_{\Delta t} = 0$. The receiver clock process noise can vary as a function of frequency stability but is normally set to white noise with large$C\varepsilon(dt)_{\Delta t}$. Since the zenith path delay parameter varies in the order of a few centimetres per hour, therefore, a random walk process of 2, 3, 4 or 5 $mm/\sqrt{hour}$ can be assigned to the *ZPD*.

PPP Solution Convergence

PPP convergence time depends on many factors including: geometry and number of satellites, observations' quality, user environment and sampling rate (Héroux et al., 2004). While these factors vary, the time needed from the first epoch to reach a converged solution will vary. At the first epoch, the PPP solution depends entirely on the pseudorange observation because the carrier-phase ambiguities are not known and the solution reflects the GPS receiver code precision and the multipath at the site (Kouba, 2000). After collecting more observations the solution starts to improve. The ambiguities and the station coordinates in static mode converge to constant values while the receiver clock and the tropospheric zenith path delay parameters fluctuate as a function of their assigned process noise.

3 TROPOSPHERIC DELAY MODELS

This chapter begins with a general overview of the atmosphere in section one. Section two is about the neutral atmosphere while section three includes the fundamentals of empirical tropospheric modelling. In section four, we present a number of common dry and wet empirical tropospheric delay models with emphasis on the NOAA model. In the last section, we present a number of well-known and widely accepted mapping functions with an emphasis on the Vienna mapping function 1 (VMF1).

3.1 The Atmosphere

The atmosphere around the Earth is divided into different regions. These regions are classified based on their common physical properties such as temperature, composition, state of mixing, and ionization. The regions of the atmosphere are called spheres and the boundaries between them are called pauses (Leick 1995).

Figure **3.1** shows some of the atmosphere regions.

In the classification based on temperature, the lowest region of the atmosphere is called the troposphere. The temperature in this region decreases in a rate of 10 Kelvin/km. The first boundary above the troposphere is the tropopause: it exists at an altitude of 10-12 Km. The troposphere is the lower and nonionized part of the atmosphere; it extends from the surface of the earth up to a height of about 40 km. The effect of the troposphere or the

neutral atmosphere on the GPS signal is denoted as tropospheric refraction, tropospheric path delay, or tropospheric delay (Hofmann-Wellenhof et al., 2001).

Above the tropopause is the stratosphere, where the temperature increases and reaches the maximum at the stratopause at an altitude of 50 km. Following the stratopause is the mesosphere, where the temperature decreases until it reaches the minimum at the mesopause at an altitude of 80-85 km. The temperature increases rapidly in the beginning of the thermopause, followed by a constant or a slight increase in temperature throughout the rest of the thermosphere (Leick, 1995).

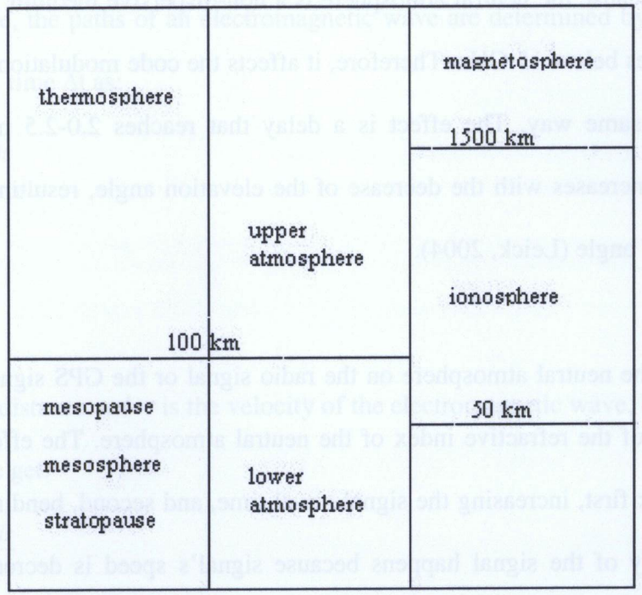

Figure 3.1 Atmosphere Regions (adapted from Leick, 1995)

There are two different regions, with regards to the ionization classification,: the ionosphere and the magnetosphere. The ionosphere exists at an altitude of 50-1500 km,

and is characterized by the high number of free electrons and positively charged atoms and molecules. The ionization is caused mainly by the effect of the ultraviolet radiation. The free electrons affect the GPS signal by advancing the carrier and delaying the code by the same amount (El-Rabbany, 2006). The magnetosphere exists above the ionosphere, where the geomagnetic field manages the particle motion.

3.2 Neutral Atmosphere

The propagation of the GPS signal through the neutral atmosphere is frequency independent because the neutral atmosphere is a non-dispersive medium for radio waves with frequencies below 15 GHz. Therefore, it affects the code modulation and the carrier phases in the same way. The effect is a delay that reaches 2.0-2.5 m in the zenith direction and increases with the decrease of the elevation angle, resulting to a delay of 20-28 m at a 5^{o} angle (Leick, 2004).

The effect of the neutral atmosphere on the radio signal or the GPS signal is a result of the variability of the refractive index of the neutral atmosphere. The effect on the GPS signal includes: first, increasing the signal travel time, and second, bending of the signal path. The delay of the signal happens because signal's speed is decreased below the speed of light as the refractive index is more than unity. The variability of the refractive index along the signal path is responsible for the signal path bending.

At any point within the atmosphere the refractive index can be expressed as a function of atmospheric pressure, temperature, and relative humidity. As the troposphere delay is

related to the refractive index, a relation between the troposphere delay and the meteorological parameters (atmospheric pressure, temperature, and relative humidity) exists.

3.3 Tropospheric Zenith Delay Modelling

3.3.1 Fundamentals

Fermat's principle states that the travel time of light (or any electromagnetic wave) between two arbitrary points is stationary with respect to neighbouring paths (Mendes, 1999). Therefore, the paths of an electromagnetic wave are determined by the condition of the minimum time Δt as:

$$\Delta t = \int_{path} dt \tag{3.1}$$

$$dt = \frac{ds}{v} \tag{3.2}$$

where ds is the distance and v is the velocity of the electromagnetic wave, by substituting (3.2) in (3.1) we get:

$$\Delta t = \int_{path} \frac{ds}{v} \tag{3.3}$$

The velocity v is related to the refractive index of the troposphere n as:

$$n = \frac{c}{v} \tag{3.4}$$

where c is the speed of light

Using Equation (3.4) into (3.3) yields

$$\Delta t = \frac{1}{c}\int_{path} nds \tag{3.5}$$

Therefore the distance along the signal path is:

$$s = c \times \Delta t = \int_{path} nds \tag{3.6}$$

and the geometrical distance is defined as:

$$l = \int_{geo} ds \tag{3.7}$$

The neutral atmospheric delay is defined by:

$$d = s - l \tag{3.8}$$

or

$$d = \int_{path} nds - \int_{geo} ds \tag{3.9}$$

By adding and subtracting the geometric length of the signal path, $\int_{path} ds$, in Equation (3.9) we get:

$$d = \int_{path} nds - \int_{path} ds + \int_{path} ds - \int_{geo} ds \tag{3.10}$$

$$d = \int_{path} (n-1)ds + \left[\int_{path} ds - \int_{geo} ds\right] \tag{3.11}$$

In Equation 3.11, the first term on the right-hand side is the delay experienced by the signal and the second is the delay due to the signal bending (Medes 1999). At zenith, the

geometric length of the signal path and the geometric path are identical, i.e. $\int_{path} ds = \int_{geo} ds$. Therefore Equation 3.11 can be written for the zenith direction as:

$$ZTD = \int_{path} (n-1)ds \tag{3.12}$$

where ZTD is the tropospheric total delay in the zenith direction. Introducing the refractivity as $N = (n-1)\times 10^6$ and back substituting it in Equation 3.5 we get:

$$ZTD = 10^{-6}\int_{path} Nds \tag{3.13}$$

3.3.2 Empirical Hydrostatic and Wet Zenith Delay Models

Separating the refractivity into hydrostatic (dry) and wet components yields

$$N = N_h + N_w \tag{3.14}$$

where the dry component results from the dry atmosphere and the wet component from the water vapour (Hofmann-Wellenhof et al., 2001). Using the dry and wet refractivity, the dry and wet zenith delays (ZHD and ZWD) can be expressed as:

$$ZHD = 10^{-6}\int N_h ds \tag{3.15}$$

and

$$ZWD = 10^{-6}\int N_w ds \tag{3.16}$$

Therefore, obtaining ZHD and ZWD require models for the refractivity and solving of the integrations in Equations (3.15) and (3.16). The hydrostatic refractivity N_h depends on the total pressure p. The equilibrium of ideal gas condition is applied in the integration of the retroactivity. Although, the hydrostatic refractivity is based on the laws of ideal gas, its integration requires assumptions about the variation of temperature and gravity along the

signal path The temporal and spatial variation of the partial water vapour pressure p_{wv}, complicates the integration of the wet refractivity. In the following paragraphs we present various models where meteorological surface data were used.

Saastamoinen Model

The Saastamoinen model was obtained using the ideal gas laws and simplified assumptions regarding variations in pressure, temperature, and relative humidity with height (Hofmann-Wellenhof et al., 2001). The hydrostatic zenith delay is given as:

$$ZHD = \frac{0.002277 P_s}{(1 - 0.0026\cos 2\phi - 0.00000028 H_s)} \tag{3.17}$$

and the wet zenith delay is given as:

$$ZWD = 0.002277\left(\frac{1255}{T_s} + 0.5\right)e_s \tag{3.18}$$

where ϕ is the latitude of the station, H_s is the orthometric height of the station in km, T_s is the surface temperature in Kelvin, P_s is the total pressure in millibars and e_s is the partial pressure due to water vapour in millibars. All the meteorological measurements are measured at the station or alternatively a standard atmospheric model can be used. The partial pressure e_s can be obtained from the relative humidity as (Feng et al., 2001):

$$e_s = RH * 6.11 * 10^{\left(\frac{7.5*T_s}{T_s+237.3}\right)} \tag{3.19}$$

where RH is the relative humidity and T_s as defined above.

Saastamoinen model was refined with additional correction terms and the total zenith delay given as:

$$ZTD = \frac{0.002277}{\cos z}\left[p_s + \left(\frac{1255}{T_s} + 0.05\right)\cdot e_s - B\tan^2 z\right] + \delta R \tag{3.20}$$

The correction term obtained with interpolation of the values in Tables 3.1 and 3.2.

Table 3.1 Correction term B for the refined Saastamoinen model (Hofmann-Wellenhof et al., 2001)

Height (km)	B (mb)
0.0	1.156
0.5	1.079
1.0	1.006
1.5	0.938
2.0	0.874
2.5	0.813
3.0	0.757
4.0	0.654
5.0	0.563

Table 3.2 Correction term δR in meters for refined Saastamoinen model (Hofmann-Wellenhof et al., 2001)

Zenith angle	Station height above sea level (km)							
	0	0.5	1.0	1.5	2.0	3.0	4.0	5.0
60° 00′	0.003	0.003	0.002	0.002	0.002	0.002	0.001	0.001
66° 00′	0.006	0.006	0.005	0.005	0.004	0.003	0.003	0.002
70° 00′	0.012	0.011	0.010	0.009	0.008	0.006	0.005	0.004
73° 00′	0.020	0.018	0.017	0.015	0.013	0.011	0.009	0.007
75° 00′	0.031	0.028	0.025	0.023	0.021	0.017	0.014	0.011
76° 00′	0.039	0.035	0.032	0.029	0.026	0.021	0.017	0.014
77° 00′	0.050	0.045	0.041	0.037	0.033	0.027	0.022	0.018
78° 00′	0.065	0.059	0.054	0.049	0.044	0.036	0.030	0.024
78° 30′	0.075	0.068	0.062	0.056	0.051	0.042	0.034	0.028
79° 00′	0.087	0.079	0.072	0.065	0.059	0.049	0.040	0.033
79° 30′	0.102	0.093	0.085	0.077	0.070	0.058	0.047	0.039
79° 45′	0.111	0.101	0.092	0.083	0.076	0.068	0.052	0.043
80° 00′	0.121	0.110	0.100	0.091	0.083	0.068	0.056	0.047

Davis et al. Model

Davis et al. model is an improved model of the Saastamoinen (Mendes, 1999) it is given as:

$$ZHD = \frac{0.0022468 P_s}{(1 - 0.0026\cos 2\phi - 0.00000028 H_s)} \tag{3.21}$$

Baby et al. Model

Baby et al. (1988) introduced the acceleration gravity as:

$$g_m = \frac{g_s}{1 + \frac{2}{r_s \sigma(\mu + 1)}} \tag{3.22}$$

where g_s is the surface gravity at the station,

$$\mu = \frac{g_s}{R_d \alpha}\left(1 - \frac{2}{r_s \sigma}\right), \tag{3.23}$$

$$\sigma = \frac{\alpha}{T_s}, \tag{3.24}$$

and $r_s = r_0 + H_s$, where r_0 is the radius of the earth, the authors used r_0 equal 6378000 m. They combined Equations 3.16 and 3.22, and substitute k_1 as provided by Bean and Dutton (Mendes, 1999) to obtain:

$$ZHD = \frac{0.022277 P_s}{g_s}\left(1 + \frac{2}{r_s \sigma(\mu + 1)}\right) \tag{3.25}$$

The wet zenith delay given by Baby et al. (1988) is:

$$ZWD = 10^{-3} \times U_s \times v \times 10^{\gamma_s} \tag{3.26}$$

where U_s is the relative humidity, v and γ are empirical coefficients related to seasonal and climate variations (Mendes, 1999). The coefficients were obtained by fitting a one-year radiosonde data and listed in Table 3.3. Their dimensions are mm.$(\%)^{-1}$ and $^\circ C^{-1}$ for v and γ respectively.

Table 3.3 Coefficients of baby et al. model for wet zenith delay (Mendes, 1999)

Latitude Interval Min - max	Climate			
	Oceanic		Continental	
	v	γ	v	γ
90° S - 70° S	0.6421	0.0290	0.4164	0.0193
70° S - 50° S	0.5864	0.0259	0.5593	0.0362
50° S - 30° S	0.6124	0.0247	0.5369	0.0285
30° S - 10° S	0.4729	0.0296	0.4229	0.0335
10° S - 10° N	1.0772	0.0192	0.6542	0.0269
10° N - 30° N	0.8063	0.0213	0.6626	0.0249
30° N - 50° N	0.6614	0.0241	0.7574	0.0224
50° N - 70° N	0.7075	0.0244	0.7652	0.0236
70° N - 90° N	0.7434	0.0256	0.7687	0.0257
Global	**0.7284**	**0.0236**	**0.7284**	**0.0236**

Hopfield Model

In 1969, Hopfield developed a tropospheric delay model using data covering the whole Earth. The model applies a single layer polytropic atmosphere model extending from the Earth's surface to altitude of about 11 km for the wet layer and 40 km for the dry layer (see Figure 3.2) (Witchayangkoon, 2000; Hofmann et al., 2001). Hopfield model is built on a relationship between dry refractivity at height h to that at the surface that was derived empirically on the bases of extensive measurements (Leick, 2004)

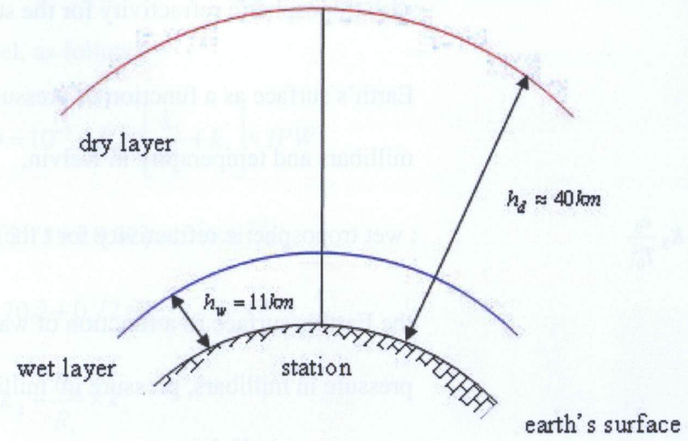

Figure 3.2 Thickness of polytropic layers for the troposphere (adapted from Hofmann-Wellenhof et al., 2001)

The Hopfield model presents the dry and wet refractivity components as a function of the receiver height above the earth's surface and is given in the following forms Witchayangkoon, 2000):

$$N_d^{Trop} = N_{d,0}^{trop}\left[\frac{H_d - h}{H_d}\right]^{\mu} \quad \textbf{(3.27)}$$

$$N_w^{Trop} = N_{w,0}^{trop}\left[\frac{H_w - h}{H_w}\right]^{\mu} \quad \textbf{(3.28)}$$

where,

$\mu = 4$ .....empirically determined power of the height ratio,

$H_d = 40136 + 148.72(T - 273.16)$: apolytropic thickness for the dry layer (m),

$H_w = 11000$: apolytropic thickness for the wet layer (m),

$N_{d,0}^{Trop} = k_1 \frac{P_0}{T_0}$: dry tropospheric refractivity for the station at the Earth's surface as a function of pressure in millibars and temperature in Kelvin,

$N_{w,0}^{Trop} = K_2 \frac{e_0}{T_0} + K_3 \frac{e_0}{T_0^2}$: wet tropospheric refractivity for t the station at the Earth's surface as a function of water vapour pressure in millibars, pressure in millibars and temperature in Kelvin,

The NOAA Model

The US National Oceanic and Atmospheric Administration (NOAA) tropospheric delay model has been developed by the NOAA Forecast Systems Lab (FSL) (Gutman et al. 2003). The model is based on numerical weather prediction (NWP) models, where surface- and space-based meteorological measurements and others, are combined into the model (Ahn et al. 2006). The NOAA model estimates the zenith hydrostatic (dry) tropospheric delay as follows:

$$ZHD = (2.2768 \pm 0.0024) \times 10^{-3} \times \frac{P_{sfc}}{f(\lambda, H)} \quad \textbf{(3.29)}$$

$$f(\lambda, H) = (1 - 0.00266 \cos 2\lambda - 0.00028H) \quad \textbf{(3.30)}$$

$$P_{sfc} = \left[Alt^{0.193} - (1.313 \times 10^{-5}) * H \right]^{5.255} \quad \textbf{(3.31)}$$

where *ZHD* is the zenith dry tropospheric delay, *H* is the orthometric height in Km, and *Alt* is the altimeter setting in mbar. The NOAA model also estimates the zenith

tropospheric wet delay from integrated precipitated water (IPW), retrieved from the weather model, as follows:

$$ZWD = 10^{-5} \times R_v \times \left[\frac{k_3}{T_m} + k_2^{'} \right] * IPW \quad \textbf{(3.32)}$$

$$k_3 = (3.739 \pm 0.02) \times 10^5 \times k^2 / P_a \quad \textbf{(3.33)}$$

$$T_m = 70.2 + 0.72 * T_{sfc} \quad \textbf{(3.34)}$$

$$k_2^{'} = k_2 - \frac{R_d}{R_v} \times k_1 \quad \textbf{(3.35)}$$

$$k_1 = (77.6 \pm 0.05) k / hPa \quad \textbf{(3.36)}$$

$$k_2 = (70.4 \pm 2.2) k / hPa \quad \textbf{(3.37)}$$

$$R_d = (287.06 \pm 0.01) JKg^{-1}K^{-1} \quad \textbf{(3.38)}$$

$$R_v = (461.525 \pm 0.0031) JKg^{-1}K^{-1} \quad \textbf{(3.39)}$$

where *ZWD* is the zenith wet tropospheric delay, *IPW* is integrated precipitated water, T_{sfc} is the temperature, R_d is the dry air constant, and R_v is the wet air constant.

The NOAA Tropospheric Delay software

The FSL of NOAA has also developed a software package that consists of a number of modules. Those modules interact together to perform a number of steps to compute and predict values of hydrostatic, wet and total zenith tropospheric delay.

The ZWD is computed by using meteorological data from a numerical weather prediction (NWP) model and Equation (3.32). The ZWD values along with the altimeter setting

values are then placed in a 20 km grid that covers part of North America. Hourly grid files are generated and stored in an FTP server. The first two lines of each grid file include the minimum longitude and latitude, respectively. Each of the subsequent lines contains the longitude, latitude, ZWD, and the altimeter setting.

The software contains the geoid code to compute the geoidal height. The input arguments of the software are latitude, longitude, ellipsoidal height, and an optional argument representing the time. If the time argument is left blank, a default gives two results keeping the current time as the datum: an analysis of one hour before the datum and a prediction of two hours after the datum.

NOAA software Flow

To generate an output from the software, the orthometric height is first estimated through a code-generated geoid height. The software then retrieves the ZWD and the altimeter setting from a grid file based on the user's longitude and latitude. The software interpolates between the longitude and latitude for the desired ZWD and altimeter setting. The altimeter setting is then used to compute the total pressure by using Equation 3.30. The total pressure is then used in Equation 3.28 to compute the zenith hydrostatic delay (ZHD). Finally, the zenith total delay is obtained by summing the ZWD to the ZHD. **Figure 3.3** represents a flowchart of the NOAA software processing flow.

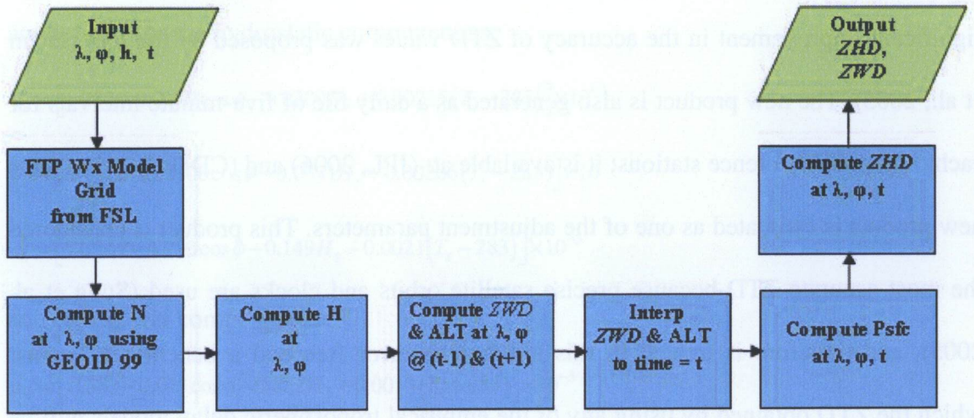

Figure 3.3 Flowchart of NOAA tropospheric delay software processing (adapted from Gutman et al., 2003)

where,

ϕ = rough latitude

λ = rough longitude

h = rough ellipsoidal height

t = time of observation

N = approximate geoidal height

H = approximate orthometric height

ZHD = zenith hydrostatic signal delay (m)

ZWD = zenith wet signal delay (m)

3.4 The IGS Tropospheric Product

Legacy IGS tropospheric product comes as a daily file, of the Zenith Total Delay (ZTD), with a sampling rate of 1-2 hours, and is based on submitted solutions from all IGS

analysis centers (AC) (Byun et al. 2005). In 2003, a new tropospheric delay product with significant improvement in the accuracy of ZTD values was proposed by the IGS (Byun et al., 2005). The new product is also generated as a daily file of five-minute intervals for each of the IGS reference stations; it is available at: (JPL, 2006) and (CDDIS, 2006). This new product is estimated as one of the adjustment parameters. This product is considered the most accurate ZTD because precise satellite orbits and clocks are used (Sung et al. 2005), and therefore is treated in this research as error free and a benchmark against which the ZTD obtained by using any of the empirical tropospheric delay models will be compared.

3.5 Mapping Functions

Tropospheric delay mapping functions relate the tropospheric zenith delay to the slant delay. The exact mapping function is complicated by the temporal and spatial variability of the troposphere (Leick 2004). A number of mapping functions have been developed, including Marini, Niell, Vienna and others.

Marini Mapping Function

Marini (1972) presented a continued fraction of the mapping function. The function then specified by Herring (1992) with three constants and normalized to unity at the zenith. For the dry and wet components, the mapping function (Hofmann-Wellenhof et al., 2001)

$$mf(e)=\frac{1+\dfrac{a_i}{1+\dfrac{b_i}{1+c_i}}}{\sin e+\dfrac{a_i}{\sin e+\dfrac{b_i}{\sin e+c_i}}} \qquad \textbf{(3.40)}$$

is used; where i is representing h (hydrostatic) or w (wet) and the coefficients a, b and c are defined for the hydrostatic component as:

$$a_h=\left[1.232+0.0139\cos\phi-0.0209H_s+0.00215(T_s-283)\right]\times10^{-3}$$

$$b_h=\left[3.1612-0.1600\cos\phi-0.0331H_s+0.00206(T_s-283)\right]\times10^{-3}$$

$$c_h=\left[71.244-4.293\cos\phi-0.149H_s-0.0021(T_s-283)\right]\times10^{-3}$$

and for the wet component as:

$$a_w=\left[0.583-0.011\cos\phi-0.052H_s+0.0014(T_s-283)\right]\times10^{-3}$$

$$b_w=\left[1.402-0.102\cos\phi-0.101H_s+0.0020(T_s-283)\right]\times10^{-3}$$

$$c_w=\left[45.85-1.91\cos\phi-1.29H_s+0.015(T_s-283)\right]\times10^{-3}$$

Niell Mapping Function (NMF)

Niell (1996) developed a mapping function given as:

$$mf(e)=\frac{1+\dfrac{a_i}{1+\dfrac{b_i}{1+c_i}}}{\sin e+\dfrac{a_i}{\sin e+\dfrac{b_i}{\sin e+c_i}}}+H_s\times10^{-3}\left[\frac{1}{\sin e}-\frac{1+\dfrac{a_{ht}}{1+\dfrac{b_{ht}}{1+c_{ht}}}}{\sin e+\dfrac{a_{ht}}{\sin e+\dfrac{b_{ht}}{\sin e+c_{ht}}}}\right] \qquad \textbf{(3.41)}$$

where e is elevation angle, H_s is the station height and a_i, b_i, and c_i are hydrostatic or wet MF coefficients. The hydrostatic MF coefficients are functions of the station latitude and day of the year. The typical formula for the three coefficients is given as:

$$a_h(\phi_i,t)=a_{h_{avg}}(\phi_i)+a_{h_{amp}}(\phi_i)\cos\left(2\pi\frac{doy-28}{365.25}\right) \qquad \textbf{(3.42)}$$

Where $a_{h_{avg}}$ and $a_{h_{amp}}$ are determined at the five latitudes corresponding to the U.S. Standard atmosphere Supplements, *doy* is the day of the year and ϕ_i is the station latitude. The second term of the right hand side of Equation 3.42 is the height correction to be applied to the hydrostatic MF only. Table 3.4 contains the NMF coefficients, where a_w, b_w and c_w are the wet MF coefficients; they are function of the station latitude only. For latitudes below or equal 15°, the coefficients are constant. The coefficient for latitudes not tabulated in Table 3.4 can be obtained by linear interpolation.

Table 3.4 Niell Mapping Function coefficients (Leick, 2004)

Coefficients	Latitude				
	15°	30°	45°	60°	75°
$a_{h_{avg}} \times 10^3$	1.2769934	1.2683230	1.2465397	1.2196049	1.2045996
$b_{h_{avg}} \times 10^3$	2.9153695	2.9152299	2.9288445	2.9022565	2.9024912
$c_{h_{avg}} \times 10^3$	62.610505	62.837393	63.721774	63.824265	64.258455
$a_{h_{amp}} \times 10^3$	0	1.2709626	2.6523662	3.4000452	4.1202191
$b_{h_{amp}} \times 10^3$	0	2.1414979	3.0160779	7.2562722	11.723375
$c_{h_{amp}} \times 10^3$	0	9.0128400	4.3497037	84.795348	170.37206
$a_w \times 10^3$	5.8021897	5.6794847	5.8118019	5.9727542	6.1641693
$b_w \times 10^3$	1.4275268	1.5138625	1.4572752	1.5007428	1.7599082
$c_w \times 10^3$	4.3472961	4.6729510	4.3908931	4.4626982	5.4736038

Isobaric Mapping Function (IMF)

In the recent years, efforts have been concentrated into developing mapping functions which are based on Numerical Weather Models (NWM). Niell (2001) proposed the Isobaric Mapping Function (IMF), which has shown significant improvements compared to NMF, especially for the dominant hydrostatic MF and in height (Vey et al. 2006). IMF is given as:

$$mf(e) = \frac{1+\dfrac{a}{1+\dfrac{b}{1+c}}}{\sin e + \dfrac{a}{\sin e + \dfrac{b}{\sin e + c}}} \tag{3.43}$$

The IMF uses input parameters based on raytracing through radiosonde data (Boehm, 2003). Niell (2001) established empirical approximation in terms of a NWM global grid of 200hPa isobaric heights, for the hydrostatic MF coefficients, and linear approximations, based on a global grid ratios of NWM slant wet delays at 3.3° elevation and its zenith delay (Kouba, 2007).

Vienna Mapping Function (VMF)

The Vienna Mapping function (VMF) was introduced by Boehm and Schuh (2004). The hydrostatic and wet VMFs are given, respectively, as:

$$mf_h(e) = \frac{1+\dfrac{a_h}{1+\dfrac{b_h}{1+c_h}}}{\sin e+\dfrac{a_h}{\sin e+\dfrac{b_h}{\sin e+c_h}}} \tag{3.44}$$

$$mf_w(e) = \frac{1+\dfrac{a_w}{1+\dfrac{b_w}{1+c_w}}}{\sin e+\dfrac{a_w}{\sin e+\dfrac{b_w}{\sin e+c_w}}} \tag{3.45}$$

where mf_h and mf_w are the hydrostatic and wet mapping functions, e is the satellite elevation angle, a_h, b_h, c_h, and a_w, b_w, c_w are coefficients for the hydrostatic and wet mapping functions, respectively. The more significant coefficients a_h and a_w are fitted to raytracing with the NWM of the European Center for Medium-Range weather forecast (ECMWF) in 6 hours intervals. The remaining coefficients (i.e., b_h, b_w, c_h, and c_w) are obtained through empirical representations (Kouba 2007). An updated version of the VMF, with improved empirical representation of the coefficients b_h, b_w, c_h, and c_w, is known as VMF1. The hydrostatic and wet coefficients b and c are given, respectively, as:

$b_h = 0.002905$

$c_h = 0.0634+0.0014 \cos 2\varphi$

where φ is the latitude.

$b_w = 0.00146$

$c_w = 0.04391$

VMF1 Grid:

The VMF1 coefficients "a" are given on a global grid of 2.5×2.0 degrees, with 2.0 degrees sampling from north to south and 2.5 degrees from east to west. For each coefficient a_h (hydrostatic coefficient) and a_w (wet coefficient) there are four files per day at time 0, 6, 12, 18 UT. The first two digits of the file name indicate whether it is for ah or aw. The next five digits indicate the year and the day of the year. The file extension shows the hour of the day. The first line in each file shows the values in degrees for north, south, west, east, spacing north-south, and spacing west-east. The remaining of the file includes parameters in latitude bands running from north to south, and from west to east within each band. The hydrostatic coefficients ah refer to zero height; therefore, correction for the gridded and station heights is needed. In addition to the ah and aw coefficients, the hydrostatic and wet zenith delays are also provided on the grid in meters, and their files are starting with zh and zw for hydrostatic and wet zenith delays respectively.

To use VMF1 an input file, which contains the VMF1 coefficients, is needed. The VMF1 coefficients files are provided for IGS, (GPS), IVS (VLBI), and IDS (DORIS) stations. For IGS stations the files are available at (ECMWF1, 2008). Each file contains a time series of records, containing the following information: station name, modified Julian date, hydrostatic coefficient "a_h", wet coefficient "a_w", hydrostatic zenith delay in meter, wet zenith delay in meter, mean temperature in Kelvin (to covert the wet zenith delay into Integrated Precipitated Water (IPW)), pressure at the station in hPa, temperature at the

station in degree Celsius, water vapour pressure at the station in hPa, and the approximate orthometric height.

Global mapping Function (GMF)

GMF, a spherical harmonic fit to the VMF1, is a less precise mapping function, which can be used as a backup for VMF1 (Kouba 2007). Similar to NMF, GMF is an empirical mapping function that can be estimated from station latitude, longitude, height and day of the year.

The GMF is determined by using 15 x 15 global grids of mean profiles for pressure, temperature, and humidity for each month from the European Centre for Medium-Range weather Forecast (ECMWF) from 40 years of reanalyzed data. From September 1999 till August 2002, the coefficients a_h and a_w were determined by applying the same strategy for VMF1. Using the empirical equations of b and c from VMF1, the parameters a, were derived by a single raytrace at 3.3° initial elevation angle. Therefore, for the 312 grid points, 36 monthly values a_h and a_w were obtained. The hydrostatic coefficients at the mean sea level were obtained by using the height correction given by Niell (1996). The mean value, a_o and the annual amplitudes, A of the sinusoidal function in Equation (2.38) were fitted to the times series of the, a parameters at each grid point, with phases referred to January 28, corresponding to NMF.

$$a = a_0 + A.\cos\left(\frac{doy - 28}{365} \cdot 2\pi\right) \qquad \textbf{(3.46)}$$

where:

$$a_0 = \sum_{n=0}^{9}\sum_{m=0}^{n} P_{nm}(\sin\phi)\cdot\left[A_{nm}\cdot\cos(m.\lambda) + B_{nm}\cdot\sin(m\cdot\lambda)\right] \qquad \textbf{(3.47)}$$

Then, the global grid of the mean values, a_0 and of the amplitudes, A for the hydrostatic and wet coefficients of the continued fraction form were expanded into spatial spherical harmonic coefficients up to degree and order of 9 according to Equation 3.47 in the least square sense. The hydrostatic and wet coefficient a can be determined for any site by using Equation 3.46.

3.6 Tropospheric Delay Models in GPSpace

In GPSpace, there are two options to deal with the tropospheric delay. In the first option, the hydrostatic component is substituted using empirical tropospheric delay model, where the ZWD is considered as one of the least-squares solution parameters that are estimated epoch by epoch. In the second option the ZHD *and* ZWD are evaluated using empirical tropospheric delay models and mapped to the slant direction using their corresponding mapping functions. In the first option, a-priori value of the zenith wet delay is needed, and obtained using an empirical tropospheric delay model. Hopfield model is the default tropospheric model and Chao model is given as another option. In the second option, when tropospheric zenith path delay is not a one of the least-squares parameter, the Hopfield model is used to evaluate the *ZPD* at each epoch. When the VMF1 is used as mapping function: instead of obtaining ZHD and ZWD using the empirical models, the values are provided within the VMF1 input file, which are based on numerical weather prediction model.

3.7 Implementation of NOAA Tropospheric Delay Corrections into GPSpace

The current version of the GPSpace® software does not include the NOAA model. Therefore, part of this research deals with the implementation of the NOAA model corrections into the GPSpace. This is done through the modification of the VMF1 input file by replacing the ZHD and ZWD values in the VMF1 input file by the NOAA model values. The VMF1 input file was further modified to contain 24 epochs per day instead of 4 epochs.

4 STOCHASTIC CHARACTARICTICS OF RESIDUAL TROPOSPHERIC DELAY

As mentioned in Chapter one, a complete modelling of the tropospheric delay must account for the residual tropospheric delay, which results from the deficiencies in the current empirical tropospheric delay models. A complete model includes functional and stochastic parts.

This chapter includes in sections one through six the methodology we followed to stochastically model the Hopfield-, Saastamoinen-, and NOAA-based residual tropospheric delays. In the first section of this chapter we will highlight the theory of random processes and time series autocovariance. We will show the methodology used to calculate the residual tropospheric delay and its estimated autocovariance function (ACF). Finally we will present how the estimated ACF is used to fit empirical autocovariance models.

Section seven provides different results of stochastic modelling steps. Results include residuals tropospheric delay generation, autocovariance functions generation and empirical autocovariance functions fittings. Stochastic modelling results include results of modelling Saastamoinen- and Hopfield-based residuals tropospheric delay for five stations over Canada and United States as well as results of NOAA-based regional

stochastic models for North America. Results of the regional stochastic models are based on data from ten IGS station spanned over North America.

4.1 Random Processes

A random process is a stochastic model which describes the probability structure of a time series (Box and Jenkins 1976). Classes of stochastic models for stationary processes include the following processes: Gauss-Markov, Periodic Random, and Random Walk, which are explained in the sub sections below

4.1.1 Gauss-Markov (GM) Process

Gauss-Markov (GM) random process is a stationary process that has an exponential autocovariance function. GM process is useful in various engineering applications since it describes and provides a good approximation for many physical random processes. The general formula of the autocovariance function of p-order GM is given in Gelb (1974) as:

$$R_{xx_p}(\tau) = \sigma_x^2 e^{-\beta_p|\tau|} \sum_{n=0}^{p-1} \frac{(p-1)!(2\beta_p|\tau|)^{p-n-1}}{(2p-2)!n!(p-n-1)!} \tag{3.48}$$

The autocovariance function of a zero mean first-order GM process is defined by a decaying exponential of the form:

$$R_{xx}(\tau) = \sigma_x^2 e^{-\beta_1|\tau|} \tag{3.49}$$

and the second-order GM autocovariance function is given by:

$$R_{xx}(\tau) = \sigma_x^2 e^{-\beta_2|\tau|}\left(1+\beta_2|\tau|\right) \tag{3.50}$$

where σ_x is the standard deviation, β_1 is the reciprocal of the correlation time and τ is the time lag.

The autocovariance time (i.e., the 1/e point) equals $1/\beta_1$ for first-order GM and $2.1461945/\beta_2$ for second-order GM. Table 4.1 shows the correlation times for GM processes with different orders.

Table 4.1 The ACF and correlation time for different order GM processes (Gelb, 1974)

Order of GM process	ACF	Correlation time
1	$\sigma_x^2 e^{-\beta_1\|\tau\|}$	$\frac{1}{\beta_1}$
2	$\sigma_x^2 e^{-\beta_2\|\tau\|}\left(1+\beta_2\|\tau\|\right)$	$\frac{2.14619450}{\beta_2}$
3	$\sigma_x^2 e^{-\beta_3\|\tau\|}\left(1+\beta_3\|\tau\|+\frac{1}{3}\beta_3^2\|\tau\|^2\right)$	$\frac{2.90462999}{\beta_3}$
4	$\sigma_x^2 e^{-\beta_4\|\tau\|}\left(1+\beta_4\|\tau\|+\frac{2}{5}\beta_4^2\|\tau\|^2+\frac{1}{15}\beta_4^3\|\tau\|^3\right)$	$\frac{3.51264850}{\beta_4}$
5	$\sigma_x^2 e^{-\beta_5\|\tau\|}\left(1+\beta_5\|\tau\|+\frac{3}{7}\beta_5^2\|\tau\|^2+\frac{2}{21}\beta_5^3\|\tau\|^3+\frac{1}{105}\beta_5^4\|\tau\|^4\right)$	$\frac{4.03422535}{\beta_5}$
. . .	. . .	. . .
P	$\sigma_x^2 e^{-\beta_p\|\tau\|}\sum_{n=0}^{p-1}\frac{(p-1)!(2\beta_p\|\tau\|)^{p-n-1}}{(2p-2)!n!(p-n-1)!}$	Solved when $R_{xx_p}(\tau_{c_p}) = \frac{\sigma_x^2}{e}$

4.1.2 Periodic Random (PR) Process

It is a random process that has an autocovariance function with periodic behaviour. A Periodic Random (PR) process can be represented by an exponential and periodic function as:

$$R_{xx}(\tau) = \sigma_x^2 e^{-\beta|\tau|}.\cos(\alpha|\tau|) \tag{3.51}$$

where β and α are positive quantities that have the same dimension $(1/time)$.

4.1.3 Random Walk Process

A random walk process is a process where the current value of a variable is composed of its previous value plus an error term defined as white noise. The discrete expression of the random walk process is given in Tralli and Lichten (1990) as:

$$x(t+\tau) = m * x(t) + \sqrt{\tau} * w_{rw} \tag{3.52}$$

where m is the correlation time, τ is the lag, and w is a zero mean white noise. The random walk process noise rate can be given as:

$$\sigma_{rw} = \sqrt{\frac{x(t+\tau) - x(t)^2}{\tau}} \tag{3.53}$$

4.2 Residual Tropospheric Delay Time Series

In this section we present the methodology followed in forming the Hopfield-, Saastamoinen-, and NOAA-based residual tropospheric delay time series.

4.2.1 Data and Data Sources

At the beginning of this research we used data from five reference IGS stations; namely, ALGO, JPLM, MDO1, PRDS, and USNO (see **Figure 4.1**). This data, which is for many

days over 2006, included: new IGS tropospheric product, metrological data (met RINEX files), and the NOAA tropospheric model grid files. The new IGS tropospheric product was used as the reference to generate residual tropospheric delays. The met RINEX files were used as input to the Hopfield and the Saastamoinen models to compute tropospheric ZTD. The NOAA grid files were used to generate the NOAA tropospheric delays using the NOAA model software. More data from another five stations, including AMC2, FLIN, HLFX, HOLB, and NLIB (see **Figure 4.1**), was collected to emphasize the NOAA-base residual tropospheric delays.

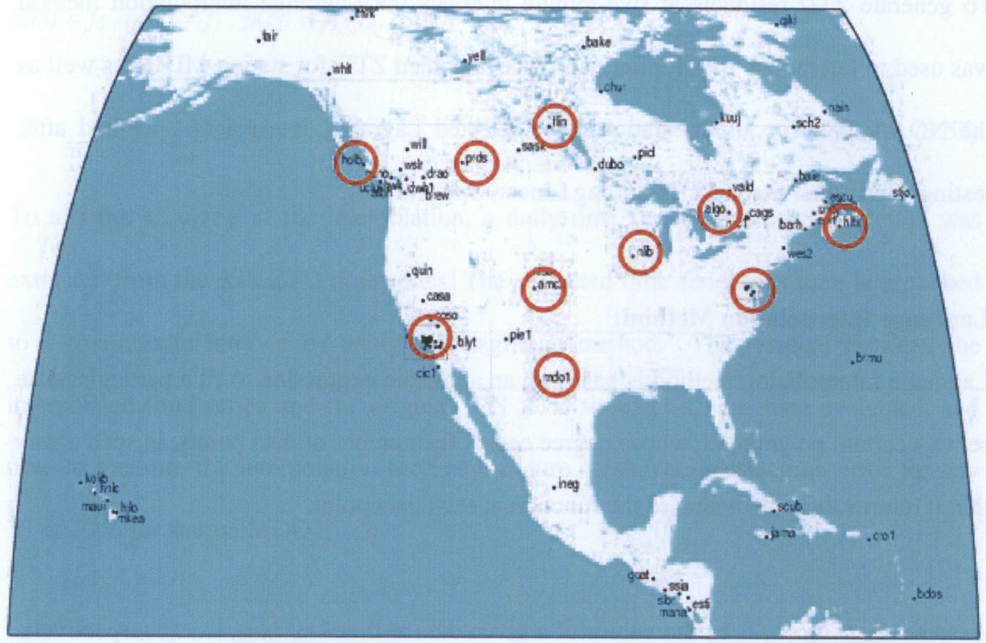

Figure 4.1 IGS station distribution in North America (IGS, 2008)

Using the Hopfield and the Saastamoinen models, a five-minute interval daily time series of ZTD were generated for the first stations except MDO1, which its time series interval was 15 minute. For all the ten stations a daily time series of five-minute interval of new

IGS ZTD were also generated. The precise station coordinates in the NAD83 datum were used as input for the NOAA software to estimate the NOAA-based total zenith tropospheric delays at each of the above mentioned stations. The output of the NOAA software included records of estimated and predicted dry, wet, and total zenith tropospheric delays; recorded every one hour. From these records, daily time series at one hour interval of ZTD were retrieved.

4.2.2 Interpolation of ZTD Data

To generate *ZTD* residuals at five-minute intervals the Lagrange interpolation method was used to interpolate the Hopfield and Saastamoinen ZTD for station MDO1 as well as the NOAA *ZTD* for all the stations. We selected Lagrange interpolation method after testing a few other methods (including Linear, Spline... etc).

Lagrange Interpolation Method:

Lagrange Interpolation method is based on an algebraic expression to fit a particular data set to a certain polynomial, whose degree equals the number of data points, in such a way that it returns the exact value of the function at each data point.

Assume $f_0, f_1, f_2, \ldots, f_n$ be the values of a given data at times $t_0, t_1, t_2, \ldots, t_n$, respectively. The approximated value of f, denoted by $p(t)$, at any time t is given by (Spiegel, 1999):

$$p(t) = a_0 f_0 + a_1 f_1 + a_2 f_2 + \cdots + a_n f_n = \sum_{i=0}^{n} a_i f_i \qquad (3.54)$$

where:

$$a_i = \frac{(t-t_0)(t-t_1)\cdots(t-t_{i-1})(t-t_{i+1})\cdots(t-t_n)}{(t_i-t_0)(t_i-t_1)\cdots(t_i-t_{i-1})(t_i-t_{i+1})\cdots(t_i-t_n)} \qquad (3.55)$$

Since the coefficient a_i is a function of t, it can be referred to as $L_i(t)$ which is called Lagrange operator. Now, substituting t by $t_0, t_1, t_2, \ldots. t_n$ in Equation 4.8 we get:

$$a_i = L_i(t) = \begin{cases} 1 & for\ t = t_i \\ 0 & otherwise \end{cases} \qquad (3.56)$$

Substituting again t by $t_0, t_1, t_2, \ldots. t_n$ in Equation 4.7 we get:

$$p(t_0) = f_0,\ p(t_1) = f_1,\ p(t_2) = f_2,\ \ldots,\ p(t_n) = f_n$$

$$p(t) = \sum_{i=0}^{n} L_i(t) f_i \qquad (3.57)$$

To test the accuracy of the interpolation, a daily time series of one hour interval was extracted from the IGS ZTD time series. The extracted time series was then interpolated to a five-minute interval by using the Lagrange method. The residual between the interpolated time series and the original IGS ZTD time series was then evaluated, and used to measure the interpolation accuracy. Figure 4.2shows interpolation error for day 15 of 2006 for station MDO1.

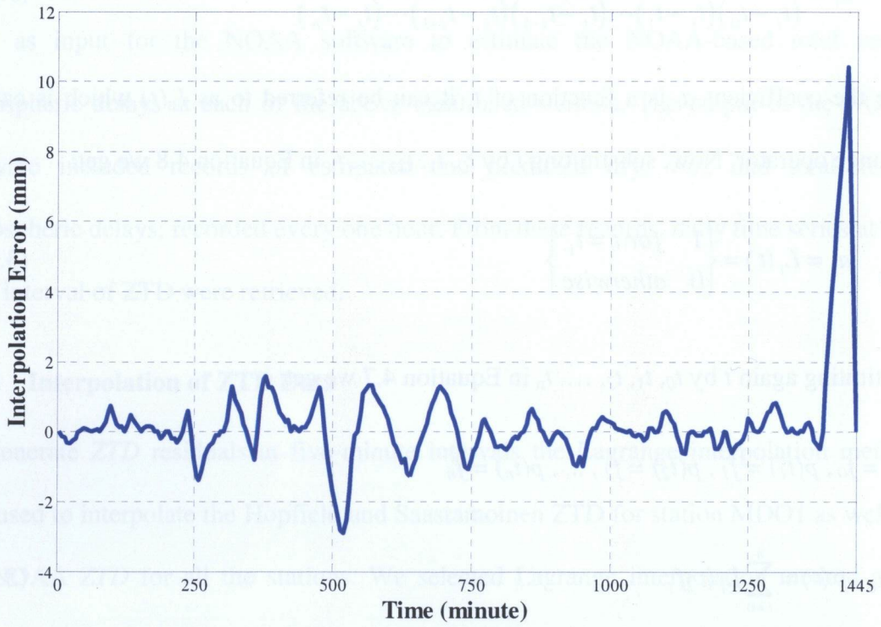

Figure 4.2 Lagrange interpolation error for day 15 of 2006 at station MDO1

The disadvantage of Lagrange interpolation method is that its accuracy degrades at the beginning and the end of the data (as seen in Figure 4.2); to overcome this limitation we added more data points at the beginning and the end in order to avoid having large interpolation error.

4.2.3 Residuals Zenith Total Tropospheric Delay

To develop the stochastic models, residual zenith tropospheric delay data series were generated for the Saastamoinen, Hopfield and NOAA tropospheric correction models. To compute the residuals, values of the new IGS tropospheric delay product were subtracted

from the corresponding values of the Saastamoinen, Hopfield and NOAA tropospheric correction models (see Equations 3.58, 3.56, and 3.57).

$$\Delta ZTD_{NOAA} = ZTD_{NOAA} - ZTD_{IGS} \tag{3.58}$$

$$\Delta ZTD_{SAAS} = ZTD_{SAAS} - ZTD_{IGS} \tag{3.59}$$

$$\Delta ZTD_{HOP} = ZTD_{HOP} - ZTD_{IGS} \tag{3.60}$$

where Δztd_{NOAA}, Δztd_{SAAS} and Δztd_{HOP} are the NOAA- , Saastamoinen- and Hopfield-based residual tropospheric delays, respectively. ztd_{NOAA}, ztd_{SAAS}, and ztd_{HOP} are the total tropospheric delays from the NOAA, Saastamoinen and Hopfield models respectively. ztd_{IGS} is the new IGS total tropospheric delay. **Figure 4.3** shows an example of residual tropospheric delays for each of the above models for day 147 of 2006 for MDO1 station.

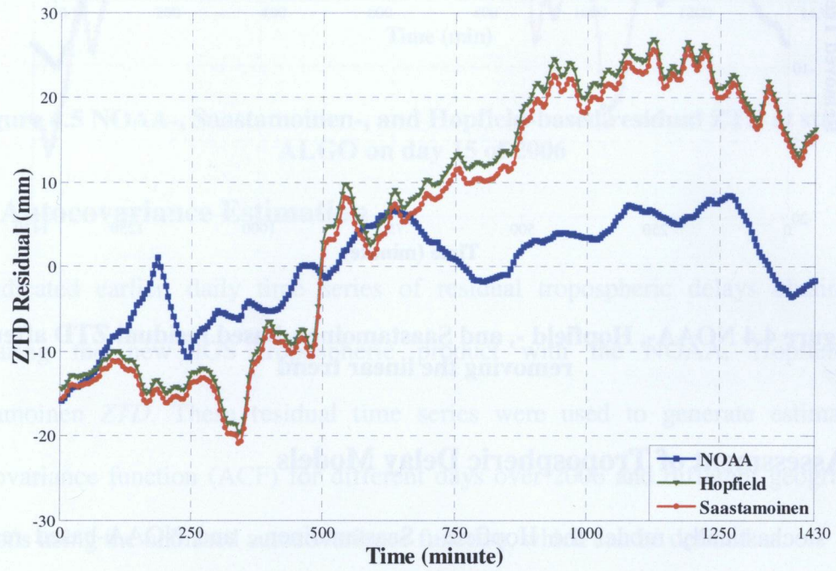

Figure 4.3 NOAA-, Hopfield -, and Saastamoinen-based residual ZTD before removing the linear trend

4.3 Linear Trend Removal

As seen in, **Figure 4.3** some residual data series exhibit linear trends. To avoid distortion in the estimated autocovariance functions, linear trends from all daily residual data series were removed using MATLAB. **Figure 4.4** shows the residual tropospheric delays data series for day 147 of 2006 for MDO1 station without the linear trend.

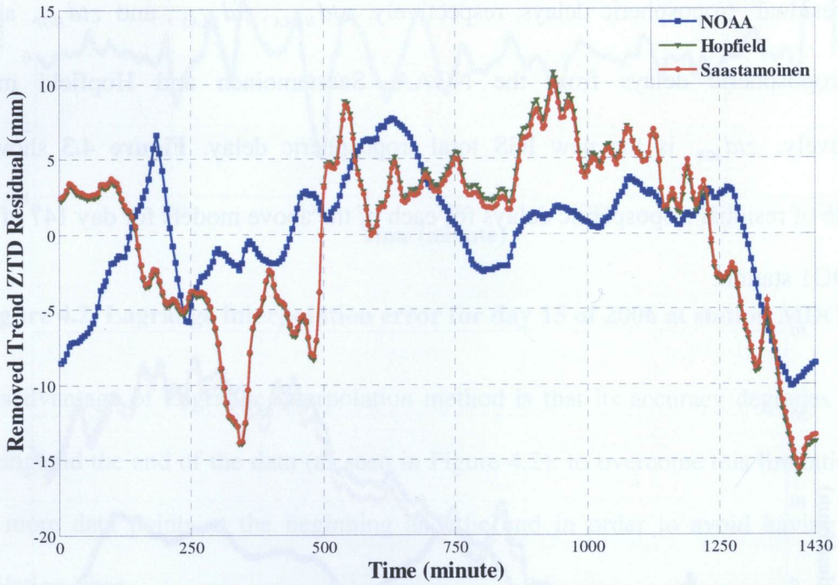

Figure 4.4 NOAA-, Hopfield -, and Saastamoinen-based residual ZTD after removing the linear trend

4.4 Assessment of Tropospheric Delay Models

Before stochastically model the Hopfield-, Saastamoinen-, and NOAA-based residual ZTD, we used them to assess their tropospheric delay models. The assessment criteria is the based on the size of the residual. The assessment's result revealed that the NOAA residual was the least, compared to the Saastamoinen and Hopfield. The results for the

Saastamoinen and Hopfield models followed a similar trend with almost the same offset. **Figure 4.5** shows residuals comparison of the three models on a typical day. For more plots see Appendix I.

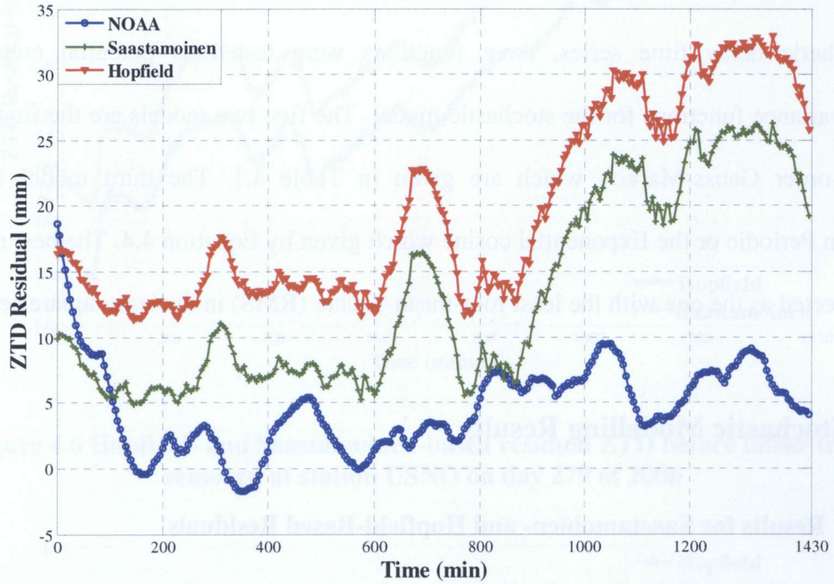

Figure 4.5 NOAA-, Saastamoinen-, and Hopfield-based residual ZTD at station ALGO on day 15 of 2006

4.5 Autocovariance Estimation

As indicated earlier, daily time series of residual tropospheric delays obtained by comparing the new IGS tropospheric product with the NOAA, Hopfield and Saastamoinen *ZTD*. These residual time series were used to generate estimates of autocovariance function (ACF) for different days over 2006 and different geographical locations using the unbiased autocovariance function, which can be defined as:

$$R_{xx}(\tau) = \frac{1}{N-|\tau|} \sum_{t=0}^{N-|\tau|-1} x(t)x(t+\tau) \tag{3.61}$$

where, t is the time, τ is the time lag and N is the series total number of points.

4.6 Empirical Autocovariance Models

To have an empirical representation of the autocovariance function of residual total tropospheric delay time series, three functions were tested as potential empirical autocovariance functions for the stochastic model. The first two models are the first- and second-order Gauss-Markov which are given in Table 4.1. The third model is the Random Periodic or the Exponential cosine which given by Equation 4.4. The best model was selected as the one with the least root-mean-square (RMS) in the least-square sense.

4.7 Stochastic Modelling Results

4.7.1 Results for Saastamoinen- and Hopfield-Based Residuals

The daily Saastamoinen- and Hopfield-based residual tropospheric delay data series described in sections 4.2.3 and 4.3 (e.g. see **Figure 4.6** and **Figure 4.7**) were used to develop the empirical autocovariance function. The estimated autocovariance functions for the residuals were computed using Equation 3.59. To avoid distortion at large lags, only the first 10% of the data record of the estimated autocovariance were considered in developing the empirical covariance function.

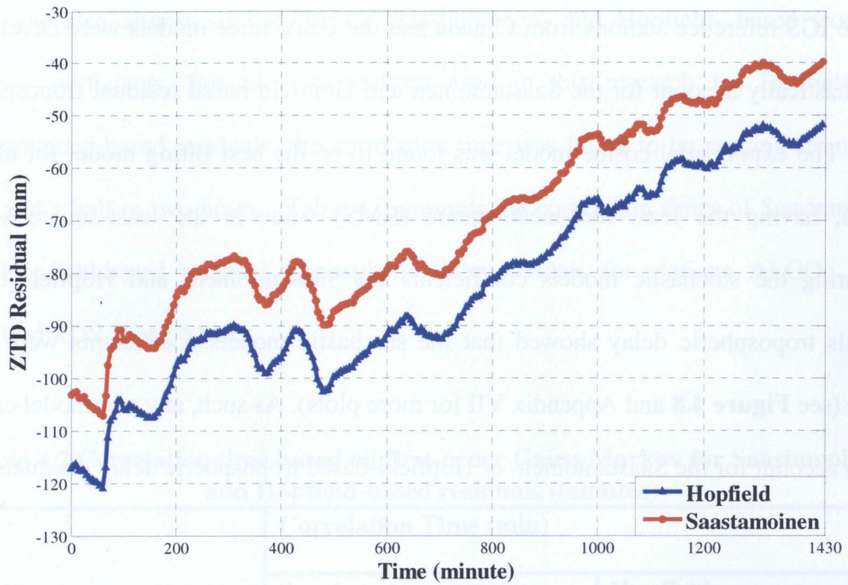

Figure 4.6 Hopfield- and Saastamoinen-based residual ZTD before linear trend removed at station USNO on day 279 of 2006

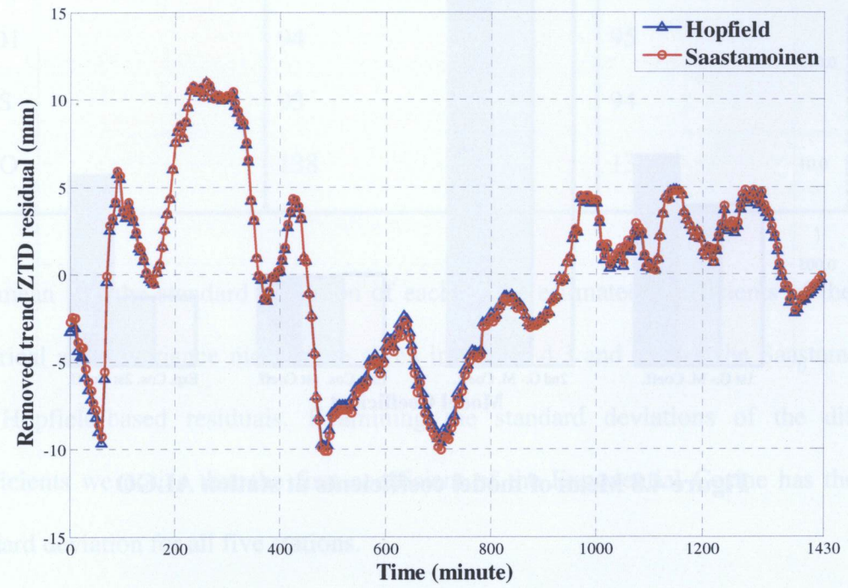

Figure 4.7 Hopfield- and Saastamoinen-based residual ZTD after linear trend removed at station USNO on day 279 of 2006

For five IGS reference stations from Canada and the USA, three models were developed to stochastically account for the Saastamoinen and Hopfield-based residual tropospheric delays. The exponential cosine model was found to be the best fitting model for all the stations, having the least root-mean-square (RMS) value in the least-square sense. Comparing the stochastic models coefficients for Saastamoinen- and Hopfield-based residuals tropospheric delay showed that the stochastic models coefficients were very similar (see **Figure 4.8** and Appendix VII for more plots). As such, any one model can be used to account for the Saastamoinen- or Hopfield-based tropospheric delay residuals.

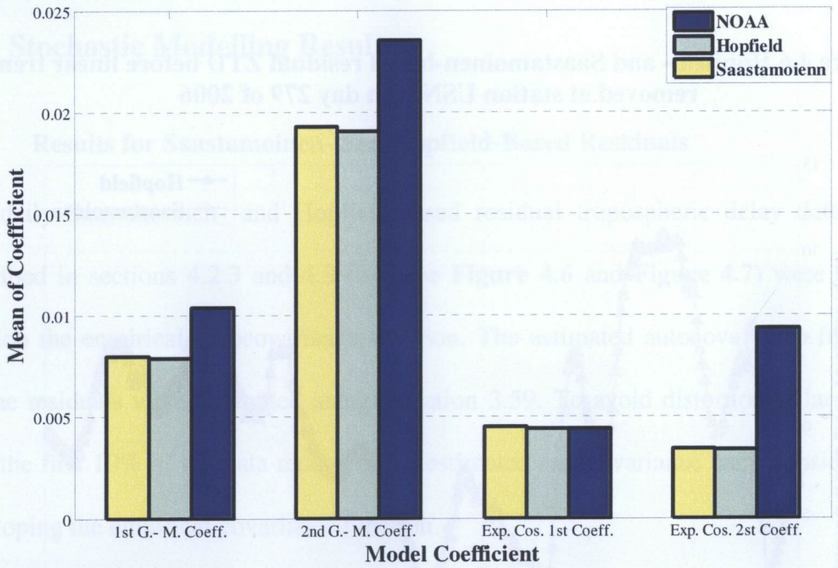

Figure 4.8 Mean of model coefficients at station ALGO

Using the first-order Gauss Markov model, we were able to compute the correlation times for the Saastamoinen- and Hopfield-based ZTD residuals. As expected, the correlation

time was also almost similar for the Saastamoinen- and Hopfield- based stochastic models coefficients. For the five stations used in this research for Hopfield- and Saastamoinen-based residuals, the correlation time was found to be ranging from about hour and a half to two hours. Table 4.2 presents the correlation times of Saastamoinen- and Hopfield-based residual tropospheric delay models for stations ALGO, JPLM, MDO1, PRDS, and USNO.

Table 4.2 Correlation time based on first-order Gauss Markov for Saastamoinen- and Hopfield-based residuals (minutes)

Station	Correlation Time (min)	
	Saastamoinen	Hopfield
ALGO	125	127
JPLM	119	117
MDO1	94	95
PRDS	93	94
USNO	138	139

The mean and the standard deviation of each of the estimated coefficients of the three empirical autocovariance models are given in Tables 4.3 and 4.4 for the Saastamoinen- and Hopfield-based residuals. Examining the standard deviations of the different coefficients we notice that the first coefficient of the Exponential Cosine has the least standard deviation for all five stations.

Table 4.3 Coefficients mean and standard deviation of empirical ACF for Saastamoinen-based residuals

Empirical ACF Model	First-order Gauss-Markov Coefficient		Second-order Gauss-Markov Coefficient		Exponential Cosine 1st Coefficient		Exponential Cosine 2nd Coefficient	
Station	Mean	STD	Mean	STD	Mean	STD	Mean	STD
ALGO	0.00799	0.0055	0.01928	0.0103	0.00451	0.0043	0.003431	0.0074
JPLM	0.00837	0.0052	0.01989	0.0093	0.00491	0.0033	0.005029	0.0065
MDO1	0.01064	0.0124	0.02434	0.0239	0.00671	0.0088	0.005408	0.0109
PRDS	0.01071	0.0060	0.02407	0.0107	0.00639	0.0034	0.006586	0.0067
USNO	0.00726	0.0043	0.01794	0.0078	0.00407	0.0028	0.003114	0.0072

Table 4.4 Coefficients mean and standard deviation of empirical ACF models for Hopfield-based residuals

Empirical ACF Model	First-order Gauss-Markov		Second-order Gauss-Markov		Exponential Cosine 1st Coefficient		Exponential Cosine 2nd Coefficient	
Station	Mean	STD	Mean	STD	Mean	STD	Mean	STD
ALGO	0.00787	0.0053	0.01905	0.0099	0.00442	0.0039	0.003374	0.0074
JPLM	0.00857	0.0051	0.02027	0.0092	0.00499	0.0034	0.005372	0.0064
MDO1	0.01051	0.0125	0.02413	0.0241	0.00661	0.0088	0.005404	0.0108
PRDS	0.01061	0.0062	0.02388	0.0109	0.00627	0.0033	0.006588	0.0067
USNO	0.00717	0.0043	0.01776	0.0079	0.00401	0.0028	0.002978	0.1029

4.7.2 Results for NOAA-Based Residuals

A total of 1350 daily data series at five-minute intervals of NOAA-based ZTD residuals for the ten stations were generated. The residual data series were spanned over many days representing the various seasons of 2006 (see **Figure 4.9**). **Figure 4.10**shows an example

of the NOAA-based residual daily time series for eight stations on day 20 of 2006. More daily plots for the other seasons of the year are available in Appendix II.

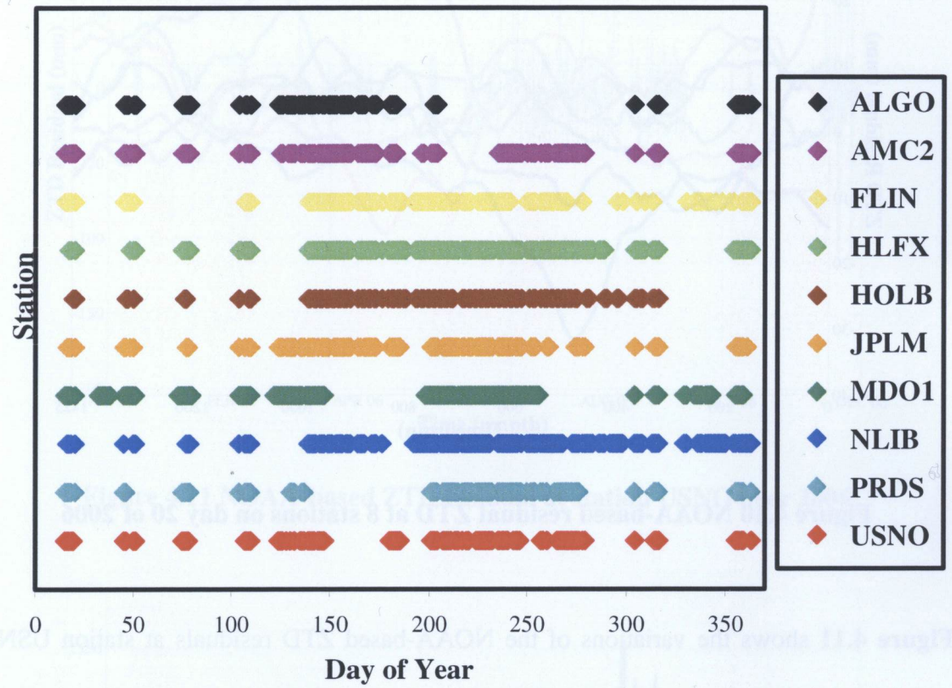

Figure 4.9 Distribution of days processed for NOAA-based ZTD residuals at 10 stations over 2006

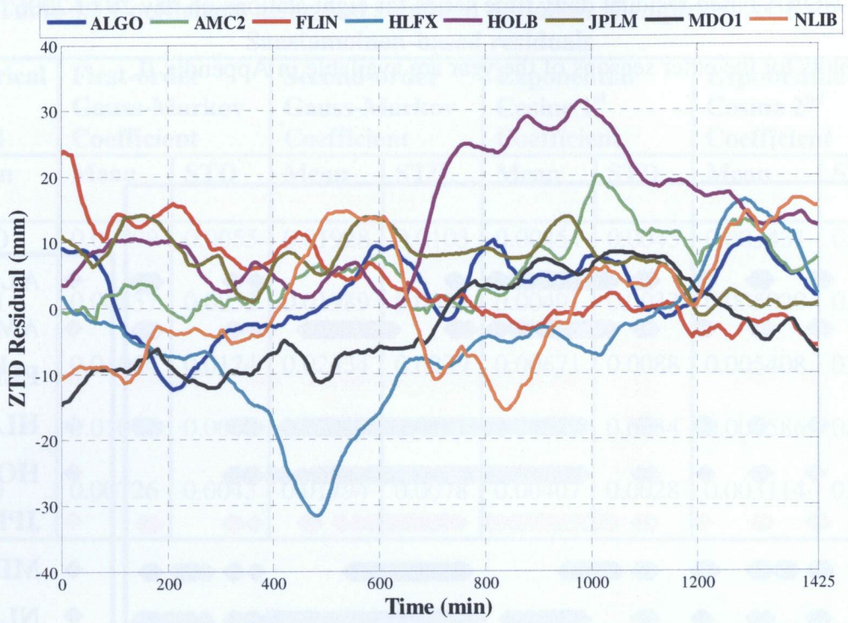

Figure 4.10 NOAA-based residual ZTD at 8 stations on day 20 of 2006

Figure 4.11 shows the variations of the NOAA-based ZTD residuals at station USNO over 2006. Except for a few spikes, the NOAA-based residual can be considered to have no significant variations over the whole year. This indicates that the NOAA model accounts for the seasonal variations quite well; which was confirmed again by Figures 4.12 and 4.13 that show the trend of the new IGS ZTD and the NOAA ZTD, respectively. For more examples of plots of NOAA-based residual over 2006 see Appendix IV. Investigation of the spikes in the NOAA-based ZTD residuals data series showed that they exist as a result of odd records of the ZTD in the NOAA model output. **Figure 4.14** shows an example of such odd records.

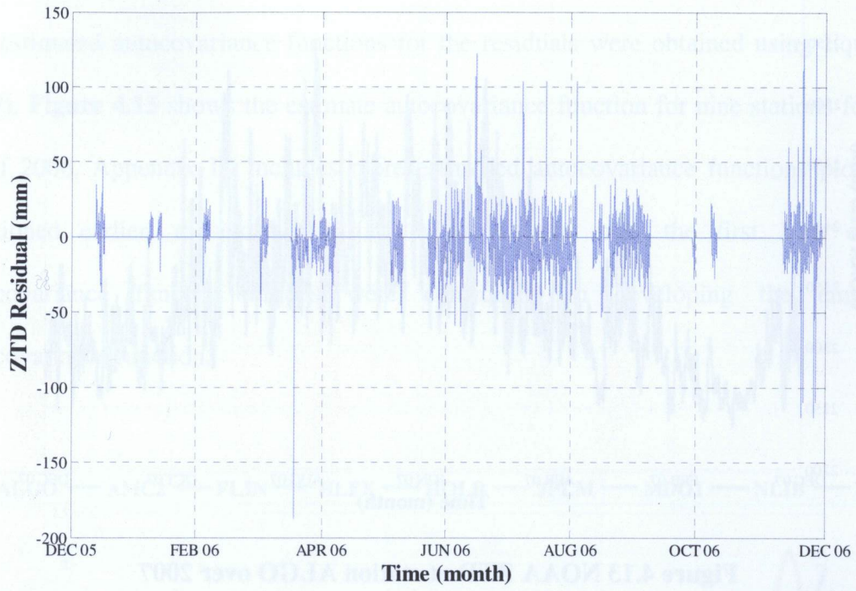

Figure 4.11 NOAA-based ZTD residual at station USNO over 2006

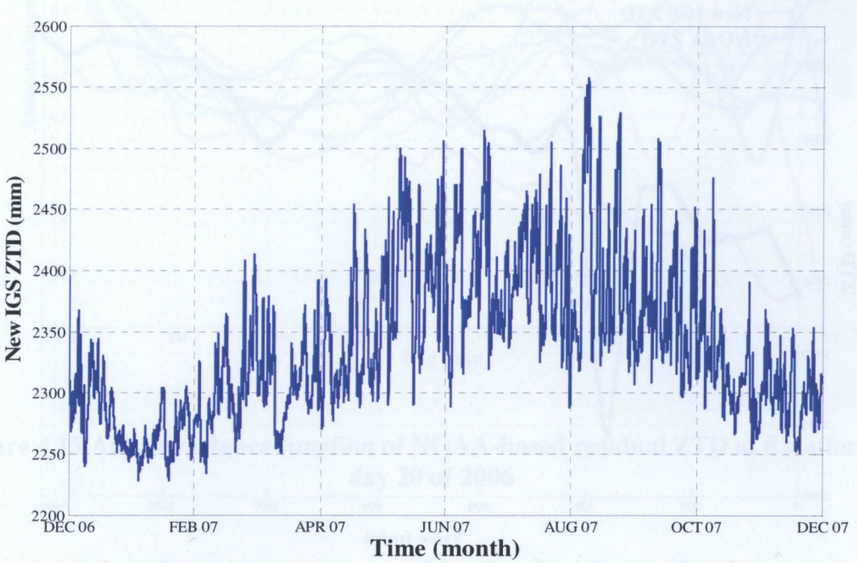

Figure 4.12 IGS new ZTD product at station ALGO over 2007

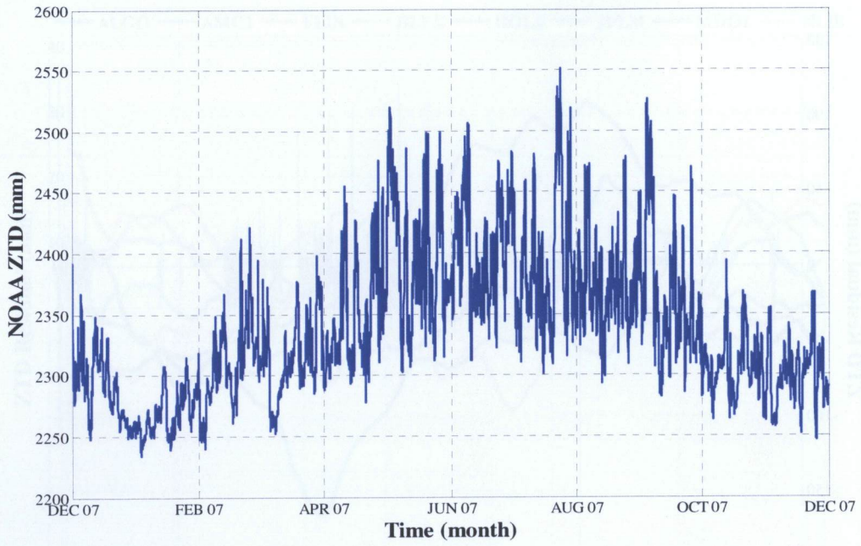

Figure 4.13 NOAA ZTD at station ALGO over 2007

Figure 4.14 Spike in NOAA ZTD at station USNO on day 75 of 2006

The Estimated ACF of NOAA-Based Residual Tropospheric Delay

The estimated autocovariance functions for the residuals were obtained using Equation (3.17). **Figure 4.15** shows the estimate autocovariance function for nine stations for day 20 of 2006. Appendix III includes more estimated autocovariance functions plots. As mentioned earlier: to avoid distortion at large lags, only the first 10% of the autocovariance function values were considered in developing the empirical autocovariance function.

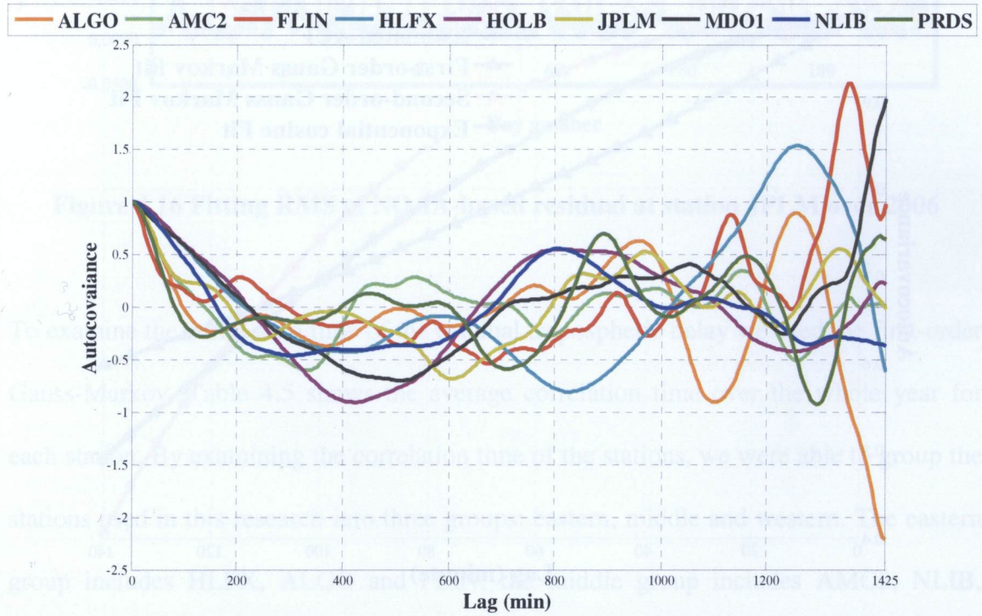

Figure 4.15 Autocovariance function of NOAA-based residual ZTD at 8 stations on day 20 of 2006

The estimated autocovariances were used to develop the empirical autocovariance function models through the least-squares (LS) estimation technique. The same three empirical models that were considered earlier for the Saastamoinen and Hopfield

residuals are utilized again: the first-order Gauss-Markov, the second-order Gauss-Markov and the exponential cosine models. Inspection of the RMS of LS model fits show that the exponential cosine model provided the best fit most of the time for all the stations. **Figure 4.16** shows an example of the three models least squares fit for day 280 of year 2006 for the NLIB station. For more fitting plots see Appendix V. **Figure 4.16** shows fitting RMS at station JPLM over 2006, Appendix VI contains similar plots for some other stations.

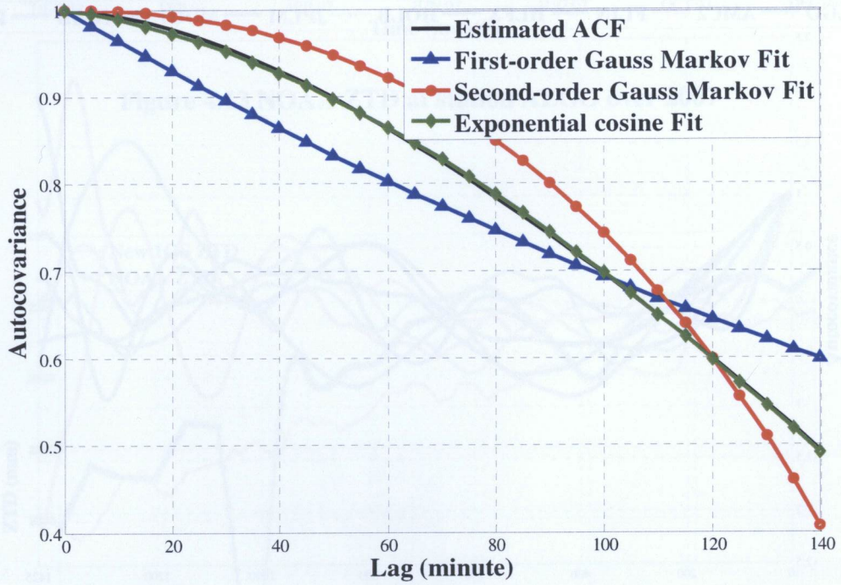

Figure 4.16 Fitting of ACF of NOAA-based residual at station NLIB on day 280 of 2006

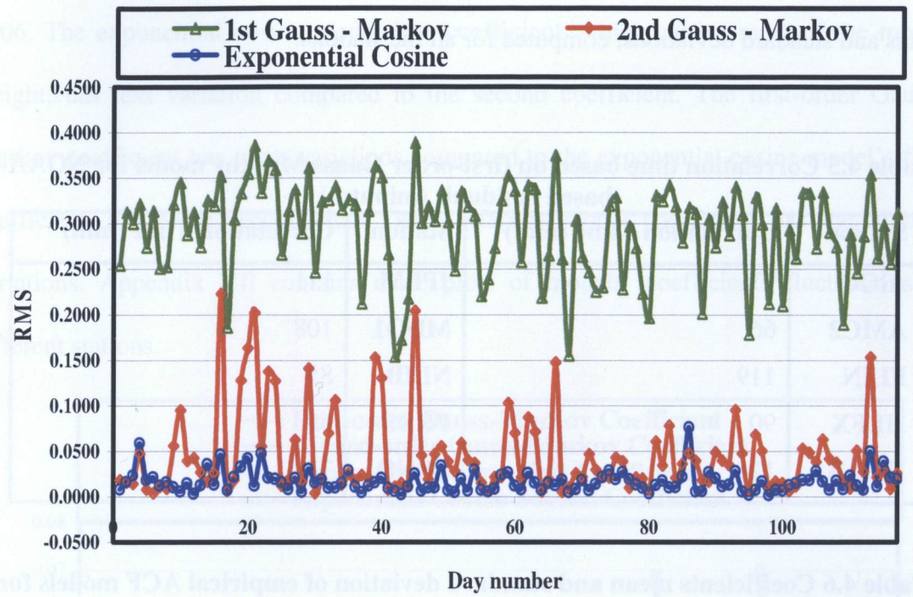

Figure 4.16 Fitting RMS of NOAA-based residual at station JPLM over 2006

To examine the correlation time of the residual tropospheric delay we used the first-order Gauss-Markov. Table 4.5 shows the average correlation time over the whole year for each station. By examining the correlation time of the stations, we were able to group the stations used in this research into three groups: eastern, middle and western. The eastern group includes HLFX, ALGO and FLIN; the middle group includes AMC2, NLIB, PRDS and USNO: and the western group includes HOLB, JPLM and MDO1. The correlation time for the three groups was in the range of 100 minutes, 75 minutes and 110 minutes for the eastern, middle, and western groups, respectively. Results of the correlation time indicated that the proposed stochastic model, first order Gauss-Markov,

was geographically dependent. Tables 4.6 shows the empirical ACF models coefficients means and standard deviations, computed for all the stations.

Table 4.5 Correlation time based on first-order Gauss Markov model for NOAA-based residuals (minutes)

Station	Correlation Time (min)	Station	Correlation Time (min)
AlGO	97	**JPLM**	111
AMC2	66	**MDO1**	108
FLIN	119	**NLIB**	85
HLFX	90	**PRDS**	63
HOLB	128	**USNO**	73

Table 4.6 Coefficients mean and standard deviation of empirical ACF models for NOAA-based residuals

Empirical ACF Model	First-Order Gauss- Markov		Second-Order Gauss-Markov		Exponential Cosine 1st Coefficient		Exponential Cosine 2nd Coefficient	
Station	Mean	STD	Mean	STD	Mean	STD	Mean	STD
ALGO	0.01036	0.0054	0.02353	0.0095	0.00439	0.0027	0.009328	0.0052
AMC2	0.01510	0.0068	0.03190	0.0117	0.00700	0.0036	0.011600	0.0058
FLIN	0.01110	0.0070	0.02470	0.0121	0.00440	0.0034	0.008300	0.0077
HLFX	0.00780	0.0042	0.01900	0.0074	0.00280	0.0021	0.006700	0.0067
HOLB	0.00840	0.0058	0.01990	0.0101	0.00350	0.0028	0.006000	0.0076
JPLM	0.00897	0.0051	0.02099	0.0091	0.00362	0.0024	0.007373	0.0067
MDO1	0.00924	0.0057	0.02153	0.0101	0.00391	0.0031	0.007428	0.0069
NLIB	0.01170	0.0059	0.02580	0.0102	0.00450	0.0032	0.010000	0.0060
PRDS	0.01584	0.0070	0.03294	0.0119	0.00647	0.0030	0.012625	0.0058
USNO	0.01378	0.0067	0.02943	0.0114	0.00585	0.0030	0.011420	0.0055

Figure 4.17 shows example of models' coefficients fluctuations throughout the year 2006. The exponential cosine model first coefficient, which carries most of the model weight, has less variation compared to the second coefficient. The first-order Gauss-Markov coefficient has more variations compared to the exponential cosine model's first coefficient, while the second-order Gauss Markov model coefficient has the highest variations. Appendix VII contains more plots of models' coefficients fluctuations at different stations.

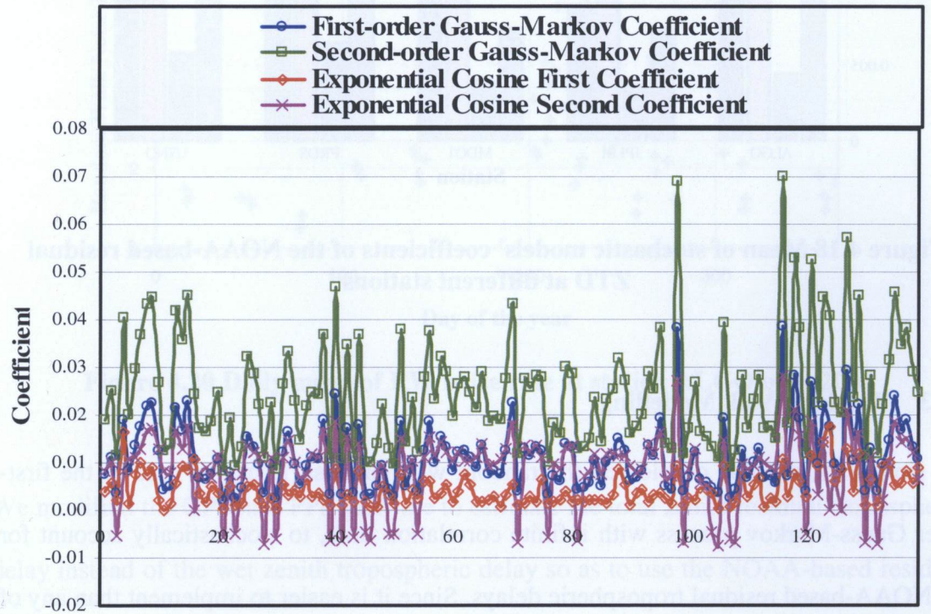

Figure 4.17 Fluctuations of coefficients of NOAA-based stochastic models at station FLIN over 2006

Figure 4.18, shows the mean of the NOAA-based residual stochastic models at different stations. For similar plots for the Hopfield- and Saastamoinen-based residuals refer to Appendix VIII.

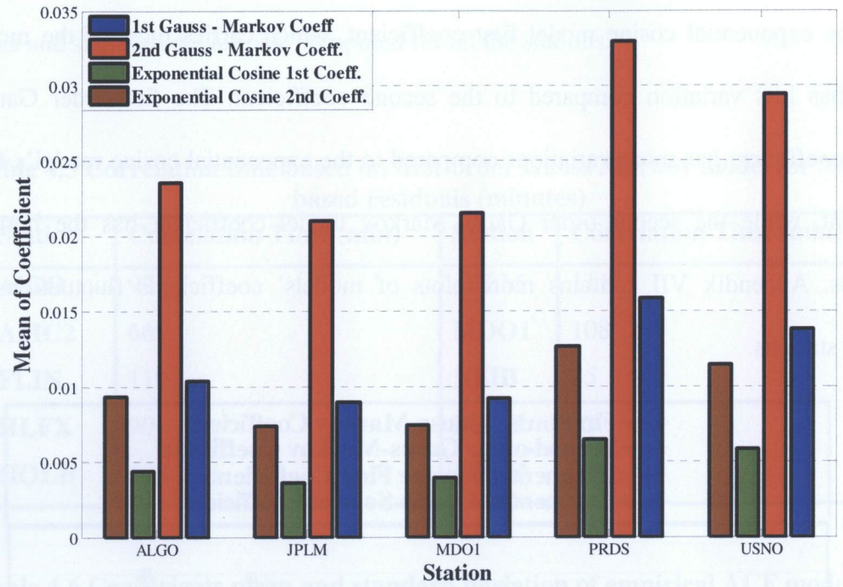

Figure 4.18 Mean of stochastic models' coefficients of the NOAA-based residual ZTD at different stations

4.7.3 Random Walk Modelling

For simplicity, we also considered the random walk process, a special case of the first-order Gauss-Markov process with infinite correlation time, to stochastically account for the NOAA-based residual tropospheric delays. Since it is easier to implement than any of the other empirical covariance models, the random walk process was used to account for the zenith total residual tropospheric delay within the GPSpace PPP software. We obtained the random walk process noise rate for each of the ten reference stations in this study by using Equation 3.9. Figure 4.20 shows the daily mean random walk process noise rate at station ALGO over 2006. For the other 9 stations, daily mean random walk rate see Appendix VIII. From the plots we can conclude that the daily mean random walk

rate is seasonal dependent. It starts at about 2 mm/√hour at the beginning of the year to reach a maximum of about 5 mm/√hour around the middle of the year and then reverts to 2 mm/√hour at the end of the year.

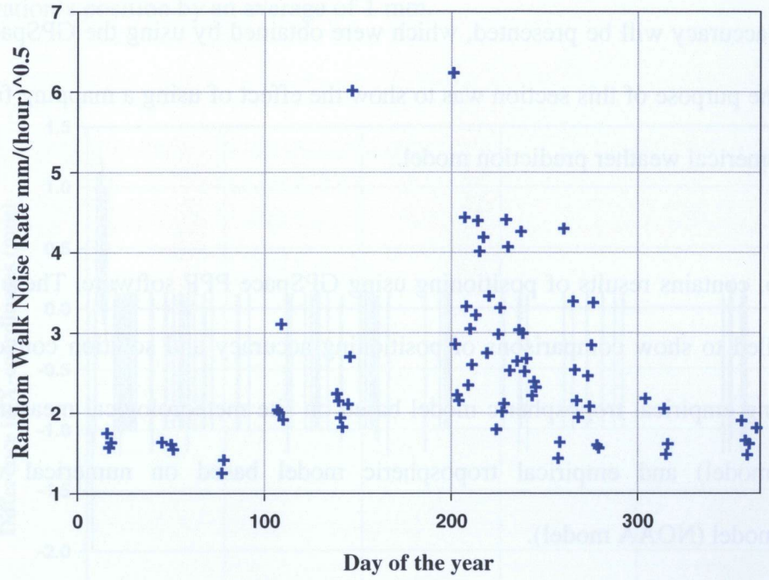

Figure 4.20 Daily mean of RW noise rate at station ALGO over 2006

We modified the GPSpace PPP software to estimate the total zenith residual tropospheric delay instead of the wet zenith tropospheric delay so as to use the NOAA-based residual random walk model The NOAA hydrostatic and wet zenith delays were used along with the corresponding VMF1 values to correct for the tropospheric delay, while the residual zenith tropospheric delay was estimated along with other unknown parameters using the method of least squares.

5 RESULTS AND ANALYSIS

In the first section of this chapter, results comparing the effects of NMF and VMF1 on positioning accuracy will be presented, which were obtained by using the GPSpace PPP software. The purpose of this section was to show the effect of using a mapping function based on numerical weather prediction model.

Section two, contains results of positioning using GPSpace PPP software. These results were compiled to show comparisons of positioning accuracy and solution convergence time by using empirical tropospheric model based on site meteorological measurements (Hopfield model) and empirical tropospheric model based on numerical weather prediction model (NOAA model).

In section three, we present results of using the RW stochastic model of the NOAA-based residual tropospheric delays along with NOAA tropospheric corrections. Each of the figures in this section contains two plots for two GPSpace positioning solutions. The first solution when tropospheric delay parameter is the ZTD, and the second when the tropospheric delay parameter is the residual ZTD with its RW stochastic model.

5.1 VMF1 vs. NMF

To show the advantage of using NWM-based mapping function, the GPSpace PPP software was used to estimate station's coordinates for two cases. In the first case the

VMF1 was used while in the second case the NMF was selected. Figure 5.1, 5.2 and 5.3 show the improvement in station's coordinates' accuracy when the VMF1 was compared to NMF. From the figures, we can see that using VMF1 improved the three components of the station's position by an average of 1 mm.

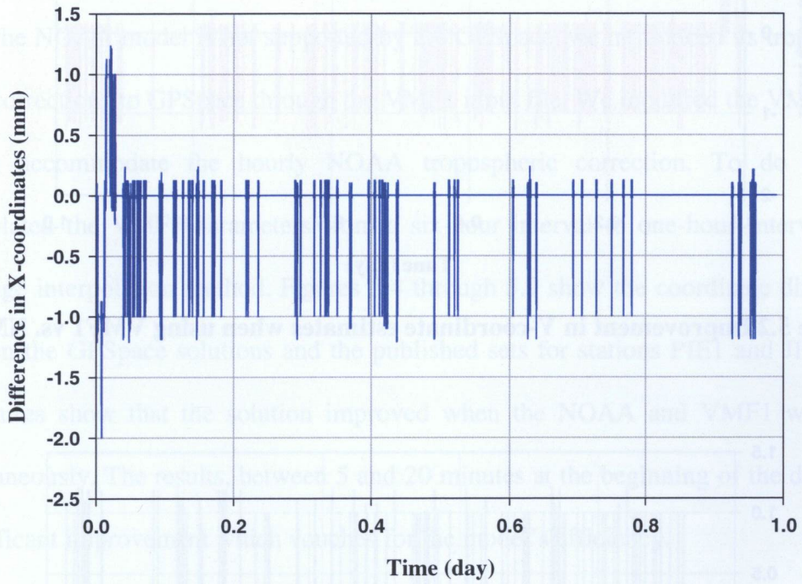

Figure 5.1 Improvement in X-coordinates when using VMF1 vs. NMF

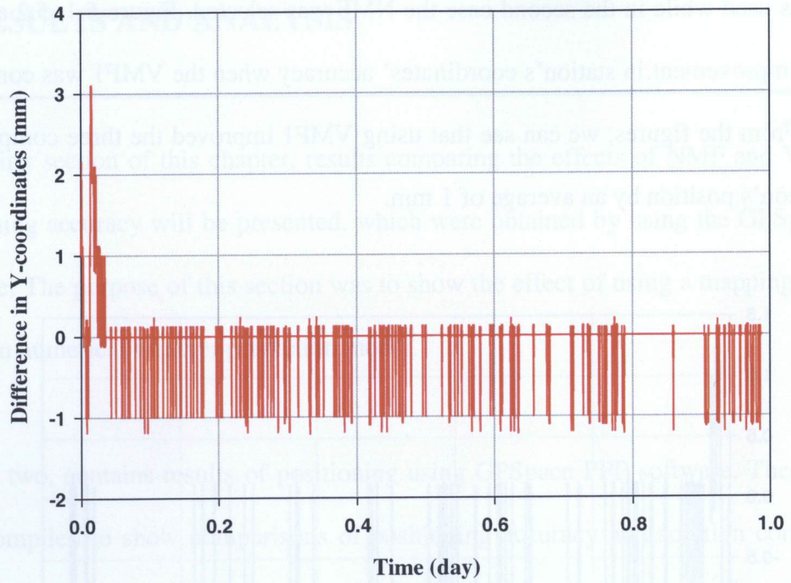

Figure 5.2 Improvement in Y-coordinate estimates when using VMF1 vs. NMF

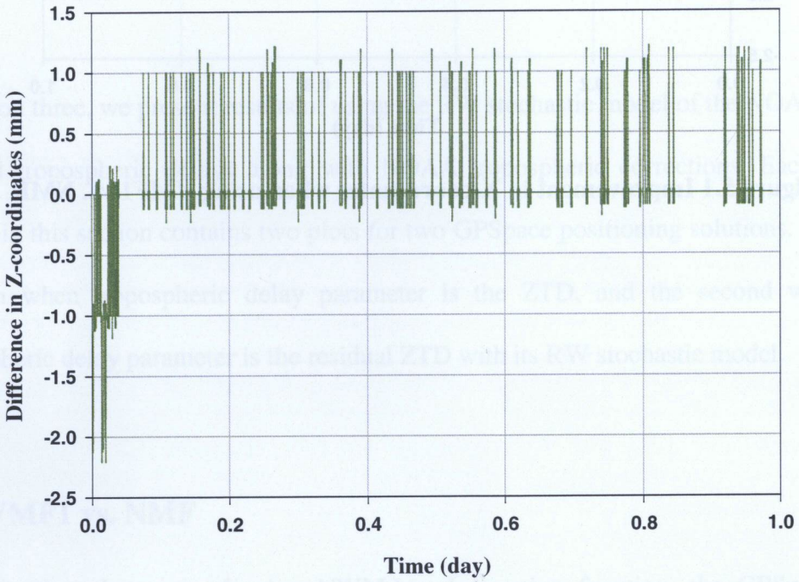

Figure 5.3 Improvements in Z-coordinate estimates when using VMF1 vs. NMF

5.2 NOAA-VMF1 vs. Hopfield-NMF

To estimate stations' coordinates using the Hopfield model as tropospheric delay model and NMF as the mapping function by using the GPSpace PPP software, 30 daily observation files were processed. We then compared those coordinates with the corresponding sets obtained by using the NOAA tropospheric model and the VMF1. Since the NOAA model is not supported by the GPSpace, we introduced its tropospheric delay corrections to GPSpace through the VMF1 input file. We modified the VMF1 input file to accommodate the hourly NOAA tropospheric correction. To do this, we interpolated the VMF1 parameters from a six-hour interval to one-hour interval using Lagrange interpolation method. Figures 5.4 through 5.9 show the coordinate differences between the GPSpace solutions and the published sets for stations PIE1 and JPLM. All the figures show that the solution improved when the NOAA and VMF1 were used simultaneously. The results, between 5 and 20 minutes at the beginning of the day, show a significant improvement which vouches for the model's efficiency.

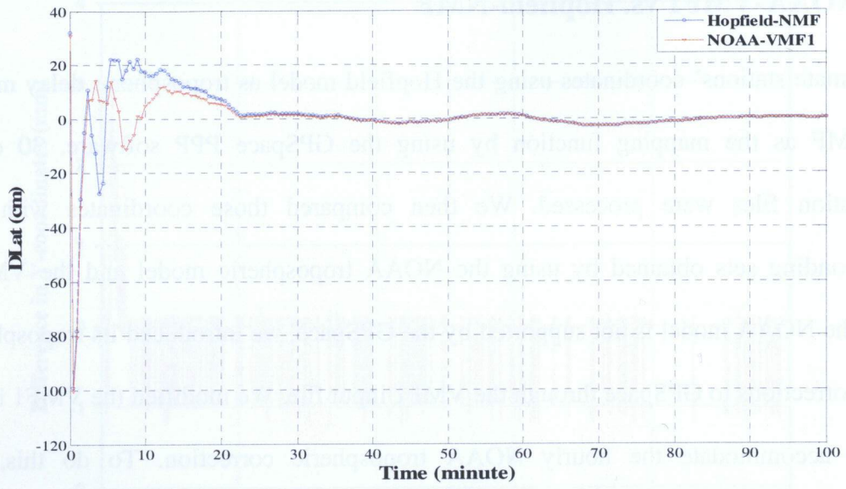

Figure 5.4 Comparing Latitude estimates using NOAA and VMF1 vs. Hopfield and NMF at station PIE1 on day 15 of 2006

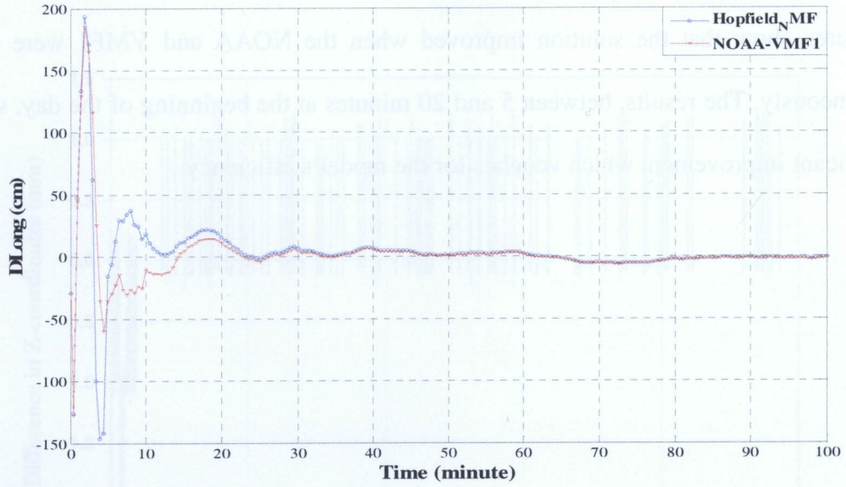

Figure 5.5 Comparing Longitude estimates using NOAA and VMF1 vs. Hopfield and NMF at station PIE1 on day 15 of 2006

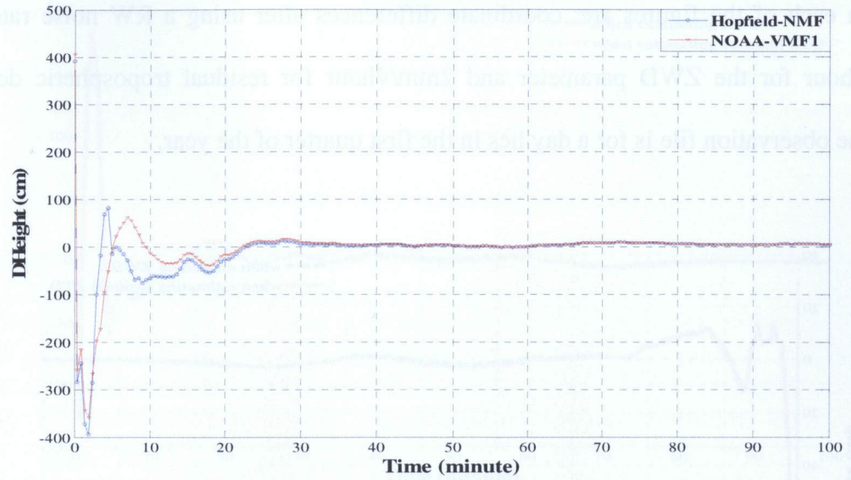

Figure 5.6 Comparing height estimates using NOAA and VMF1 vs. Hopfield and NMF at station PIE1 on day 15 of 2006

5.3 Implementation of Random Walk Stochastic Model

As mentioned earlier, the default tropospheric delay parameter to be estimated within GPSpace is the ZWD. The ZHD is obtained using Hopfield or Chao tropospheric delay models. To test our RW model, we modified the GPSpace software to accept in addition to the ZHD correction the ZWD. In this case instead of estimating the ZWD parameter the GPSpace will estimate the total zenith tropospheric delay residual. A suitable value of residual tropospheric delay random walk noise rate will be used for the purpose to account for the residual tropospheric delay fluctuation.

A comparison was made between the coordinates obtained with the GPSpace before and after the modification mentioned above. Figures 5.7 through 5.9 show the latitude, longitude and ellipsoidal height differences for station PIE1 on day 15 of 2006. The two

plots in each of the figures are: coordinate differences after using a RW noise rate of 5mm/√hour for the ZWD parameter and 2mm/√hour for residual tropospheric delay, since the observation file is for a day lies in the first quarter of the year.

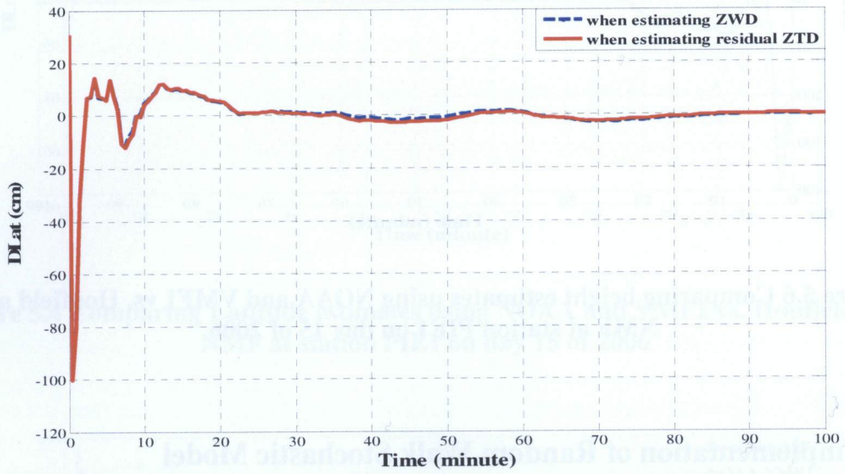

Figure 5.7 Comparing Latitude estimate when ZTD RW stochastic model is used vs. residual ZTD RW stochastic model at station PIE1 on day 15 of 2006

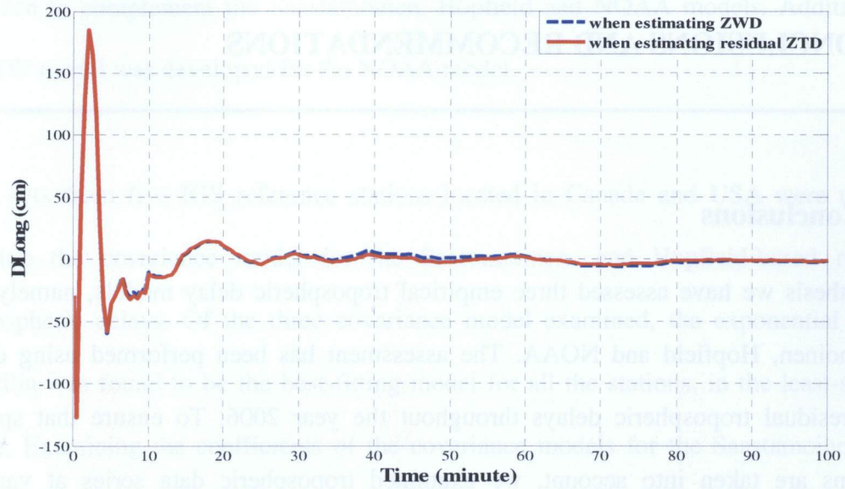

Figure 5.8 Comparing Longitude estimates when ZTD RW stochastic model is used vs. residual ZTD RW stochastic model at station PIE1 on day 15 of 2006

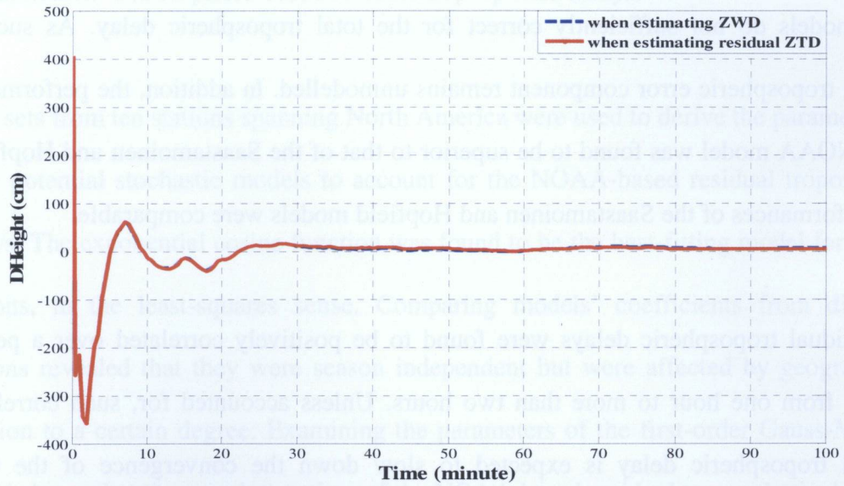

Figure 5.9 Comparing height estimates when ZTD RW stochastic model is used vs. residual ZTD RW stochastic model at station PIE1 on day 15 of 2006

6 CONCLUSIONS AND RECOMMENDATIONS

6.1 Conclusions

In this thesis we have assessed three empirical tropospheric delay models, namely the Saastamoinen, Hopfield and NOAA. The assessment has been performed using daily zenith residual tropospheric delays throughout the year 2006. To ensure that spatial variations are taken into account, we examined tropospheric data series at various geographical locations across North America. The new highly accurate IGS tropospheric correction product was used as a reference. It has been shown that all three tropospheric delay models do not sufficiently correct for the total tropospheric delay. As such, a residual tropospheric error component remains unmodelled. In addition, the performance of the NOAA model was found to be superior to that of the Saastamoinen and Hopfield. The performances of the Saastamoinen and Hopfield models were comparable.

The residual tropospheric delays were found to be positively correlated over a period varying from one hour to more than two hours. Unless accounted for, such correlated residual tropospheric delay is expected to slow down the convergence of the GPS solution. In addition, an overestimation of the accuracy of both the observations and the resulting position estimates would be expected.

To account for the residual tropospheric delays, three stochastic models, namely first- and second-order Gauss Markov models and the exponential cosine, were developed in this

research to complement the Saastamoinen, Hopfield and NOAA models. Additionally, the RW model was developed for the NOAA model.

Data sets from five IGS reference stations located in Canada and USA were used to develop the covariance model for the Saastamoinen- and Hopfield-based residual tropospheric delays. Of the three covariance model examined, the exponential cosine function was found to be the best-fitting model for all the stations, in the least-squares sense. Examining the coefficients of the covariance models for the Saastamoinen- and Hopfield-based residual tropospheric delays showed that they are almost identical. This indicates that only one stochastic model can be used to account for either of the Saastamoinen- and Hopfield-based residual tropospheric delays.

Data sets from ten stations spanning North America were used to derive the parameters of three potential stochastic models to account for the NOAA-based residual tropospheric delays. The exponential cosine function was found to be the best-fitting model for all the stations, in the least-squares sense. Comparing models' coefficients from different stations revealed that they were season independent but were affected by geographical location to a certain degree. Examining the parameters of the first-order Gauss-Markov model shows that the correlation time of the NOAA-based residual tropospheric delays is varies in the range of 100 minutes, 75 minutes and 110 minutes for the eastern, middle, and western regions, respectively.

When VMF1 was selected in the GPSpace software, the positioning accuracy was improved by an average of 1mm compared to NMF. Additionally, implementation of the NOAA tropospheric corrections also improved the positioning accuracy within the convergence time by a few centimetres. After convergence, the improvement in positioning accuracy was insignificant.

Implementation of the RW stochastic model to account for NOAA-based residual tropospheric delay showed that it is insignificant within the convergence time zone; however, it showed minor improvement after the convergence time.

6.2 Recommendations for Future Research

To benefit from the foundation laid by this research, future research should concentrate on the following recommendations.

- As NOAA-based tropospheric residuals are season-independent, more data from other years would improve the robustness of the stochastic models developed in this research.
- To rigorously account for residual tropospheric delays, it is recommended that stochastic models developed in this study be used to modify the GPS observation's covariance matrix. Although this leads to fully populated covariance matrix, its inverse, which is needed in the least-squares estimation, will be a block diagonal when first-order Gauss Markov model is used.
- A Kalman filter-based algorithm, which uses first-order Gauss Markov model to account for residual tropospheric delay, is recommended to be developed.

- For real-time applications, stochastic models of the NOAA-based residual tropospheric delays should be developed using the predicted part of NOAA tropospheric corrections.
- More data from stations spanning North America are needed to develop regional stochastic models for Hopfield- and Saastamoinen-based residual tropospheric delays.
- A global stochastic model could be developed for Hopfield and/or Saastamoinen models using well-distributed worldwide IGS stations.

REFERENCES

Ahn YW, Lachapelle G, Skone S, Gutman S, Sahm S (2006) Analysis of GPS RTK Performance Using external NOAA Tropospheric Corrections Integrated with a Multiple Reference Station Approach. GPS Solutions Vol. 10, No. 3, pp. 171-186.

Baby, H.B., P. Golé, and J. Lavergnat (1988). "A model for the tropospheric excess path length of radio waves from surface meteorological measurements." Radio Science, Vol. 23, No. 6, pp. 1023-1038.

Bisnath. S., David D., Allen C., Michael P. (2004) " Analysis of the Utility of the NOAA-Generated Tropospheric Refraction Corrections for the Next Generation Nationwide DGPS Service" Institute of Navigation, National Technical Meeting , 21-24 September, Long Beach, CA, pp. 1288-1297.

Boehm J. and Schuh H. (2003). "Vienna Mapping Functions", Proceedings of the 16th Working Meeting on European VLBI for Geodesy and Astronomy, May 9-10, Leipzig, Germany, pp. 131-143.

Boehm J., Niell A., Tregoning P. and Schuh H. (2006). "Global Mapping Function (GMF): A new empirical mapping function based on numerical weather model data", Journal of Geophysical Research Letters, VOL. 33, L07304, DOI: 10.1029/2005GL024361.

Box G.E.P and G.M. Jenkins. (1976). "Time Series Analysis, Forecasting and Control". Holden-Day Inc., San Francisco, California, USA.

Byun S H, Y E, Bar-Sever, Gendt G (2005). "The New Tropospheric Product of the International GPS Service", Proceedings of the ION GNSS 2005, 14-16 September, Long beach, CA, pp. 241-249.

Byun S. H., Bar-Server Y. E., Gendt G. (2005) " The New Tropospheric Product of the International GNSS Service" Institute of Navigation, National Technical Meeting , 13-16 September, Long Beach, CA, pp. 241-249.

CDDIS (2006). Crustal Dynamics data Information system. ftp://cddis.gsfc.nasa.gov/pub/gps/products/trop_new (Accessed on December 14, 2006).

ECMWF (2008). European Centre for Medium-Range Weather Forecast home page. (http://mars.hg.tuwien.ac.at/~ecmwf1/GPS) (Accessed on June 10, 2008).

El-Rabbany A (1994) "The Effect of Physical Correlation on the Ambiguity Resolution and Accuracy Estimation in GPS Differential Positioning", Ph.D. thesis. New Brunswick University.

El-Rabbany, A. (2006). Introduction to GPS: The Global Positioning System, 2nd Edition, Artech House Inc., Norwood, Massachusetts.

Feng Y., Bai Z.,Fang P., Williams A. (2001)."GPS Water Vapour Experimental Results From Observations of the Australian Regional GPS Network (ARGN)" 2001-A Spatial Odyssey: 42nd Australian Surveyors Congress.

Gao, Y, S Skone, K Chen, N A Nicholson (2004) "Real-Time Sensing Atmospheric Water Vapor Using Precise GPS Orbit and Clock Products". Proceedings of the ION GSNN 2005, 21-24 September, Long Beach, CA, pp. 2343-2352.

Gelb, A. (ED.) (1974). "Applied Optimal Estimation" Massachusetts Institute of Technology, Cambridge.

GPS-System. (GPS-explained) (2008). ULR: www.kowoma.de/en/gps/multipath.gif (retrieved on June 29, 2008).

Gutman, S., T. Fuller-Rowell, D. Robinson (2003). "Using NOAA Atmospheric Models to Improve Ionospheric and Tropospheric Corrections." U.S. Coast Guard DGPS Symp., Portsmouth, VA, 19 June.

Hay, C., and Wong, J. "Enhancing (2000). GPS: Tropospheric Delay Prediction at the Master Control Station" GPS World, Vol. 11, No. 1, January 2000, pp. 56-62.

Héroux P.,Kouba J., Collins P. and Lahaye F. (2001). "GPS Carrier-Phase Point Positiong with Precise Orbit Products." Proceedings of the International Symposium on Kinematic Systems in Geodesy, Geomatics and Navigation, Banff, Canada, pp. 518-528.

Hofmann-Wellenhof, B., Lichtenegger, H., and Collins, J. (2001). "Global Positioning System: Theory and Practice", Springer-Verlag Wien, New York.

Hofmann-Wellenhof, B., Lichtenegger, H., and Wasle, E. (2008). "Global Navigation Satellite Systems GPS, GLONASS, Galileo & more", Fourth, revised edition. Springer-Verlag Wien, New York.

IGS (2004). International GPS Service Homepage. http://igscb.jpl.nasa.gov/.

IGS (2007). International GPS Service Homepage. ftp://sideshow.jpl.nasa.gov/pub/igs_trop/trop_new.

IGS (2008) International GPS Service Homepage http://igscb.jpl.nasa.gov/network/maps/all_nam.html.

JPL (2006). Jet Propulsion Laboratory. ftp://sideshow.jpl.nasa.gov/pub/igs_trop/trop_new (Accessed on July 20, 2006).

Kouba J, Heroux P (2001) "Precise Point Positioning Using Orbit and Clock Products" GPS Solutions vol. 5, No. 2, pp. 12-28.

Kouba J., (2007). "Implementation and testing of the gridded Vienna Mapping Function 1 (VMF1)", Journal of Geophysics Research.

Kouba, J. (2003). "A Guide to Using International GPS Service (IGS)." Available at http://igscb.jpl.nasa.gov/igscb/resource/pubs/GuidetoUsingIGSProducts.pdf.

Leick, A. (1995). "GPS Satellite Surveying", 2nd Edition, John Wiley & sons, Inc.

Leick, A. (2004). "GPS Satellite Surveying", 3rd Edition, John Wiley & sons, Inc.

Manning D. (2005)."NGA GPS Monitor Station High-Performance Cesium Frequency Standard Stability: From NGA Kalman filter Clock Estimates", Journal of IEEE pp. 840-847.

Marini, J. W. (1972). "Correction of satellite tracking data for an arbitrary tropospheric profile." Radio Science, Vol. 7, No. 2, pp. 223-231.

Mendes, V. B. (1999). "Modeling Modelling the neutral-atmosphere propagation delay in radiometric space techniques.", Ph.D. dissertation, Department of Geodesy and Geomatics Engineering Technical Report No. 199, University of New Brunswick, Fredericton, New Brunswick, Canada, 353 pp.

NASA (2008). ULR: http://visibleearth.nasa.gov/) (retrieved on June 29, 2008).

Niell, A. E. (1996) "Global mapping functions for the atmosphere delay at radio wavelengths." Journal of Geophysical Research, Vol. 101, No. B2, pp. 3227-3246.

Spiegel, M.R. (1999). "*Mathematical Handbook of Formulas and Tables*." McGraw Hill.

Teunissen, P. J. G, and A. Kleusberg (eds.) (1998)."GPS for Geodesy", 2nd Edition, New York Springer-Verlag.

The Aerospace Corporation (2008) .ULR: www.aero.org/.../crosslink/summer2002/03.html (retrieved on June 15, 2008).

Tralli D. and Lichten S. (1990)."Stochastic Estimation of Tropospheric Path Delays in Global Positioing System geodetic Measurements", Journal of Geodesy, VOL. 64, No. 2, DOI: 10.1007/BF02520642 pp. 127-159.

Vey S, Fritche M, Dietrich R, Rothacher M, Rülke A, Steigenberger P (2006) "Influence of mapping Function Parameters on Global GPS Network Analyses: Comparison between NMF and IMF" Journal of Geophysics Research DOI:10.1029/2005GL024361.

Vollath U., Brockmann E.and Chen X. (2003)."Troposphere: Signal or Noise?" Institute of Navigation, GPS/GNSS, 9-12 September, Portland, OR, pp. 1709-1717.

Xia, L. (2004)." Multipath in GPS Navigation and Positioning, GPS Solutions", 8, April, pp. 49-50.

Xu G. (2007)." GPS Theory, Algorithms and Applications". 2nd edition. Springer-Berlin, Heidelberg, New York.

APPENDIX I: DAILY RESIDUAL TROPOSPHERIC DELAY TIME SERIES FOR SAASTAMOINEN, HOPFIELD AND NOAA MODELS

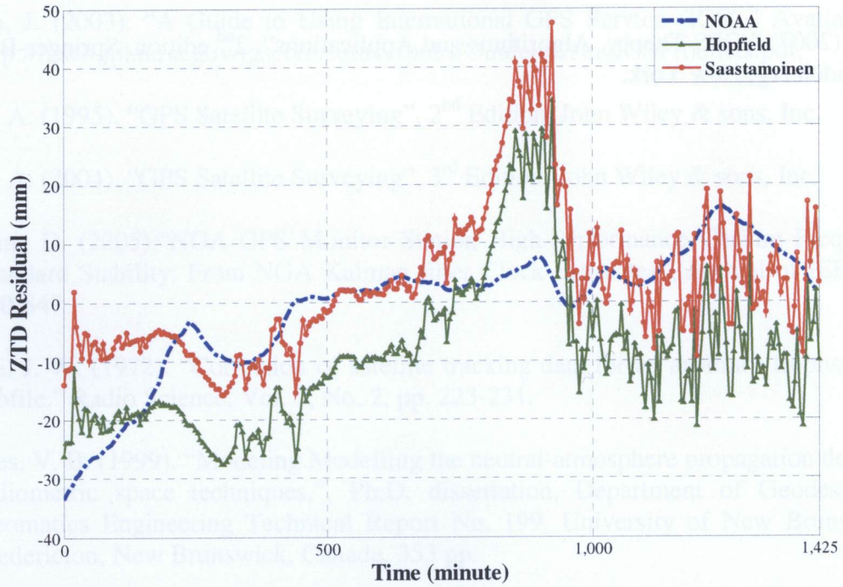

Figure I.1 NOAA-, Hopfield-, and Saastamoinen-based ZTD at station PRDS on day 201 of 2006

APPENDIX II: DAILY RESIDUAL TROPOSPHERIC DELAY TIME SERIES FOR NOAA MODEL

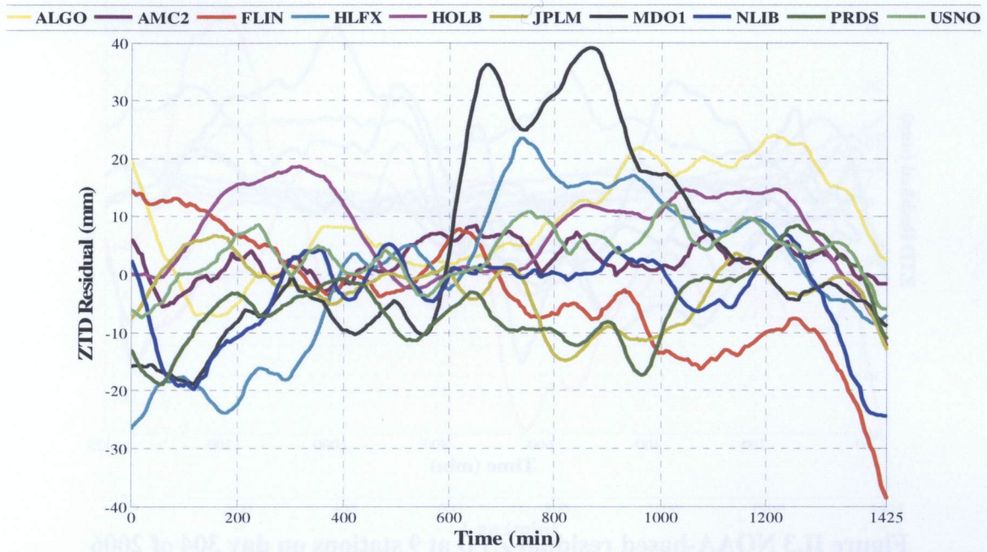

Figure II.1 NOAA-based residual ZTD at 10 stations on day 110 of 2006

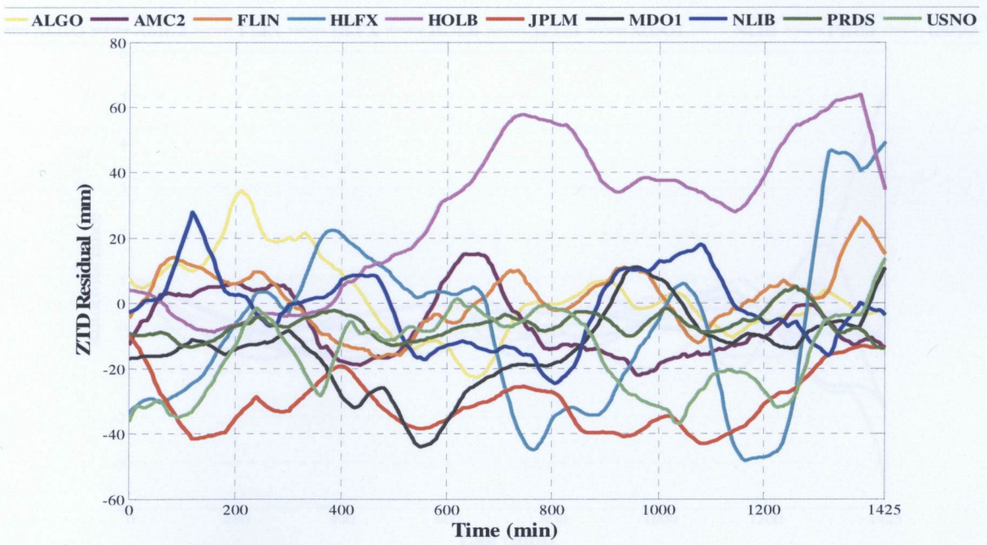

Figure II.2 NOAA-based residual ZTD at 10 stations on day 202 of 2006

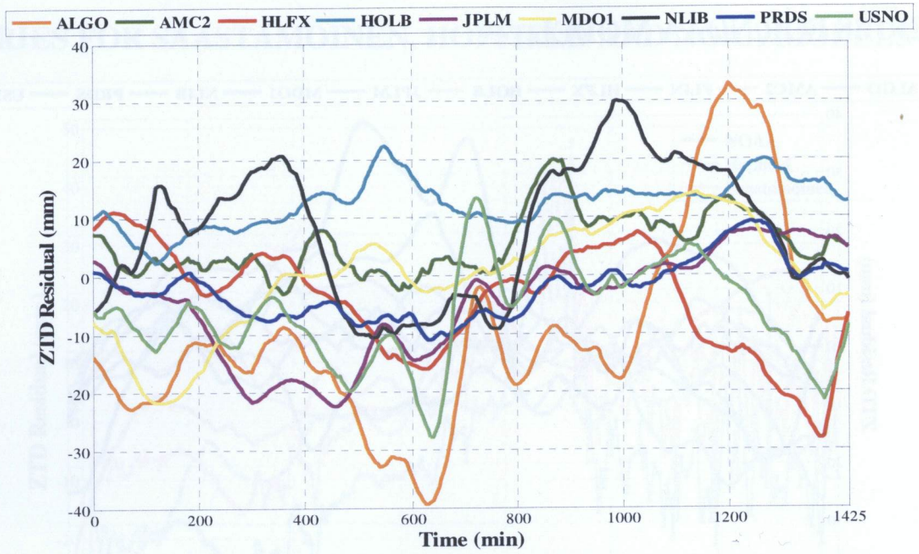

Figure II.3 NOAA-based residual ZTD at 9 stations on day 304 of 2006

APPENDIX III: ESTIMATED AUTOCOVARIANCE FUNCTION OF RESIDUAL TROPOSPHERIC DELAY

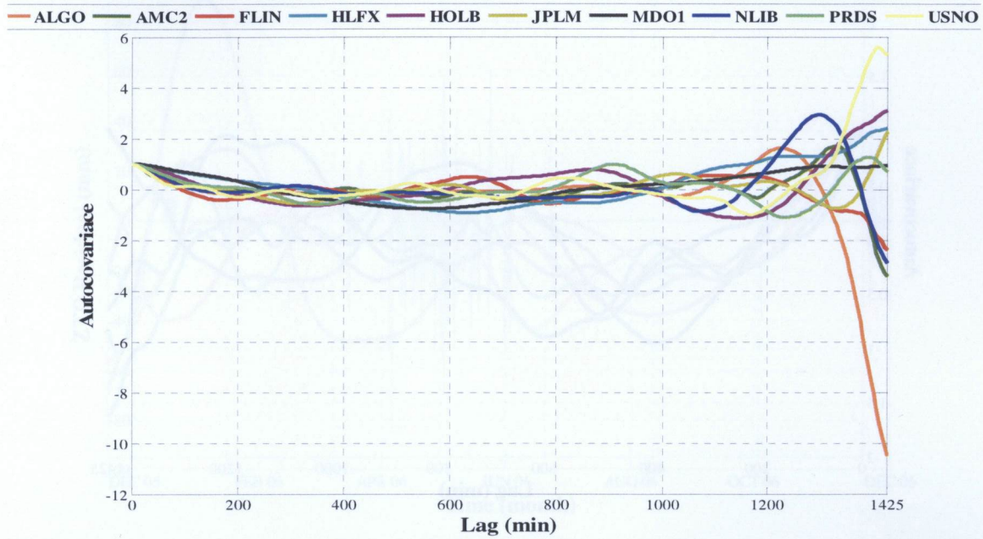

Figure III.1 ACF of NOAA-based residual ZTD at 9 stations on day 110 of 2006

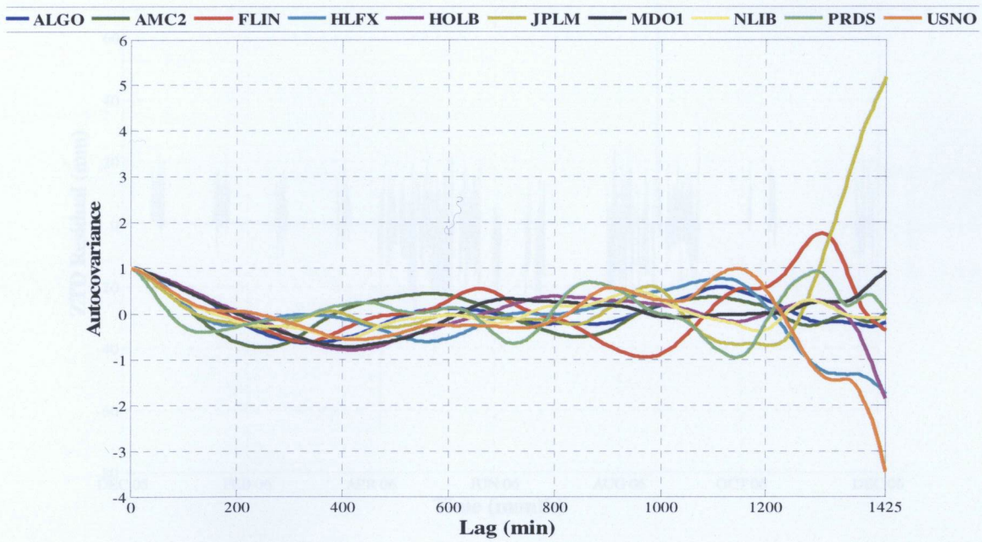

Figure III.2 ACF of NOAA-based residual ZTD at 10 stations on day 202 of 2006

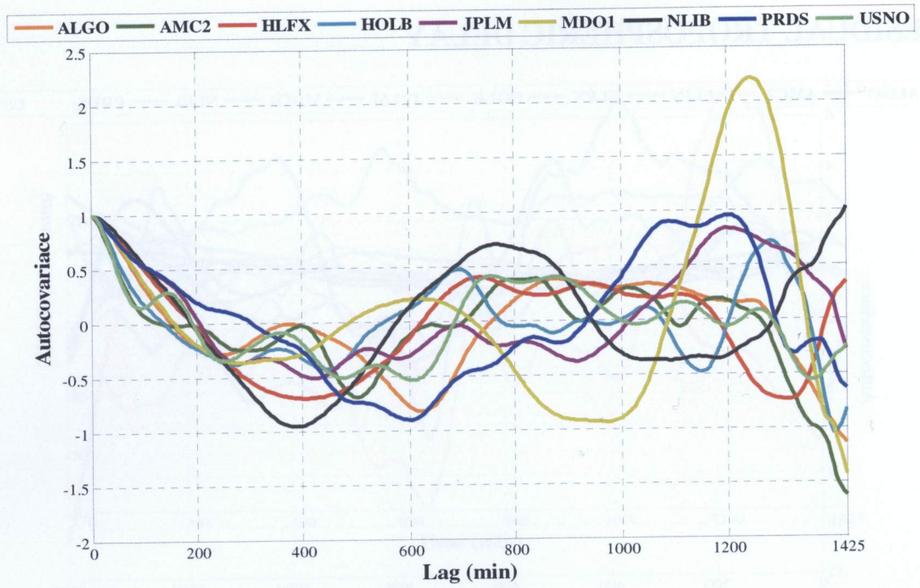

Figure III.3 ACF of NOAA-based residual ZTD at 10 stations on day 304 of 2006

APPENDIX IV: RESIDUAL TROPOSPHERIC DELAY OVER THE YEAR

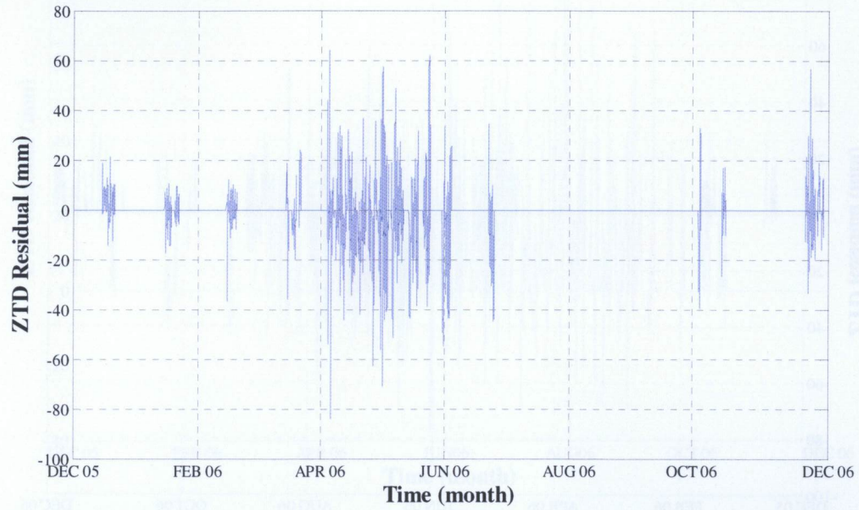

Figure IV.1 NOAA-based residual ZTD at station ALGO over 2006

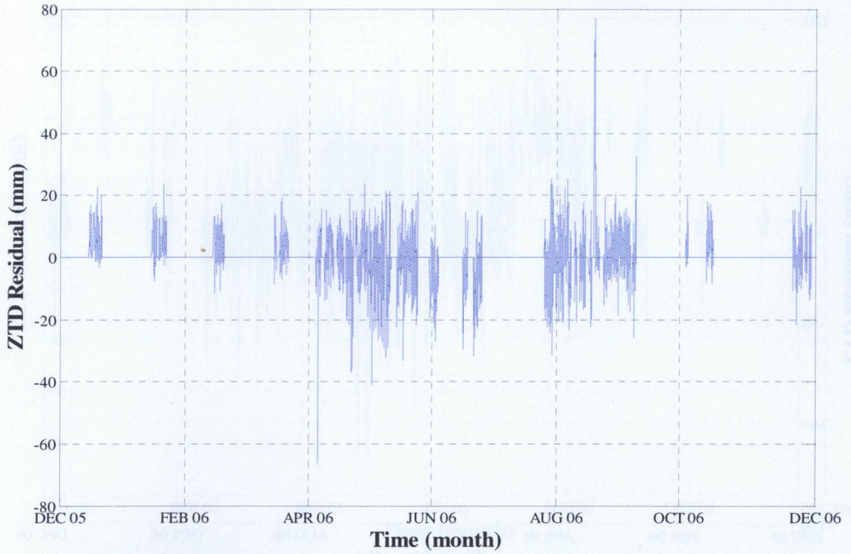

Figure IV.2 NOAA-based residual ZTD at station AMC2 over 2006

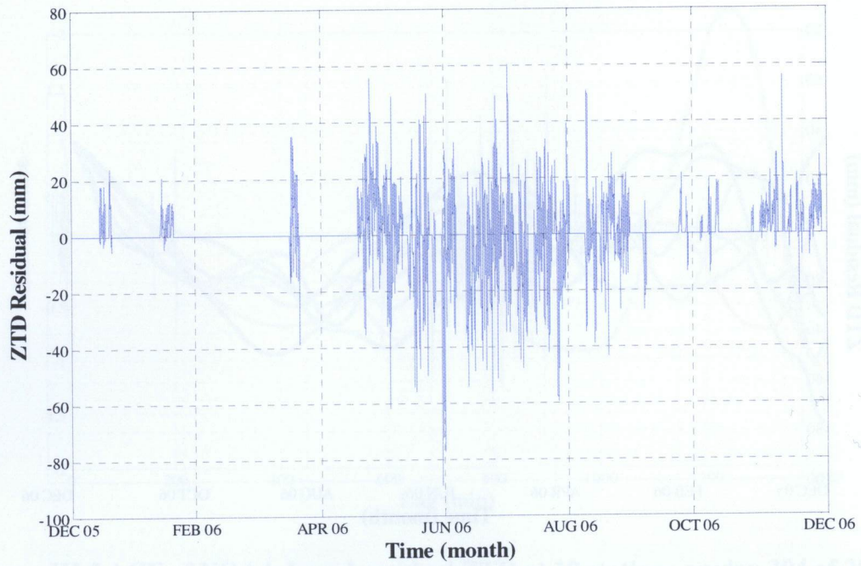

Figure IV.3 NOAA-based residual ZTD at station FLIN over 2006

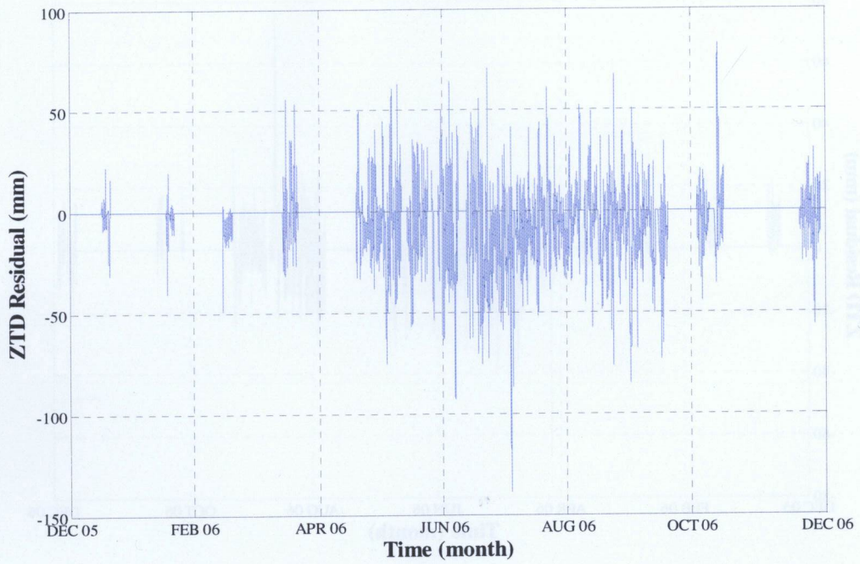

Figure IV.4 NOAA-based residual ZTD at station HLFX over 2006

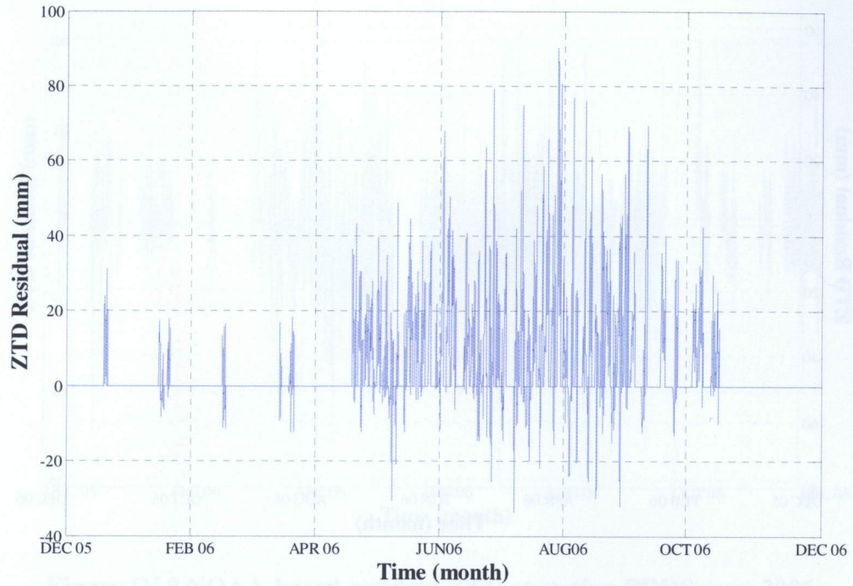

Figure IV.5 NOAA-based residual ZTD at station HOLB over 2006

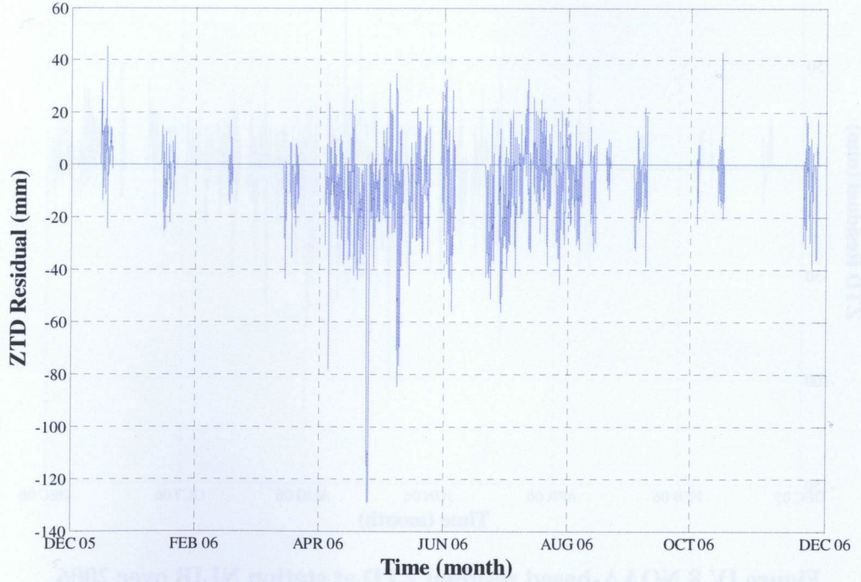

Figure IV.6 NOAA-based residual ZTD at station JPLM over 2006

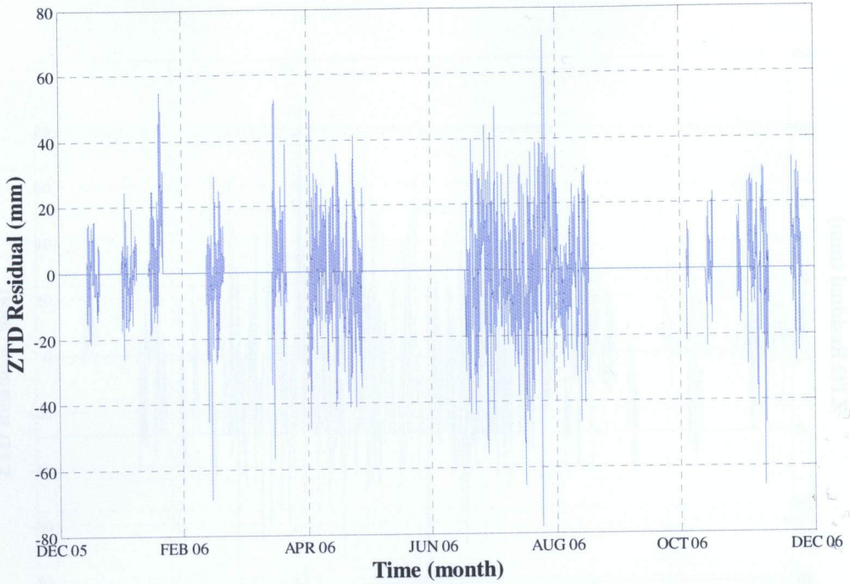

Figure IV.7 NOAA-based residual ZTD at station MDO1 over 2006

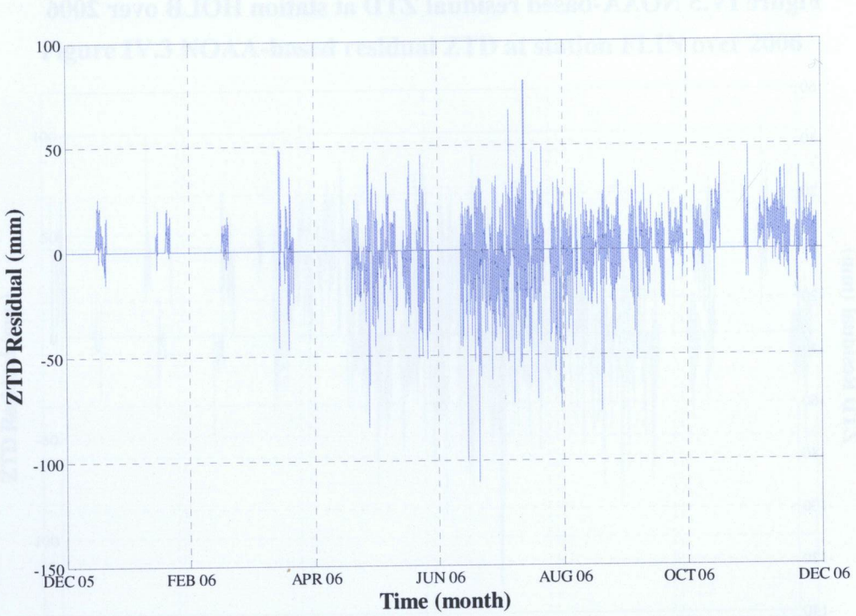

Figure IV.8 NOAA-based residual ZTD at station NLIB over 2006

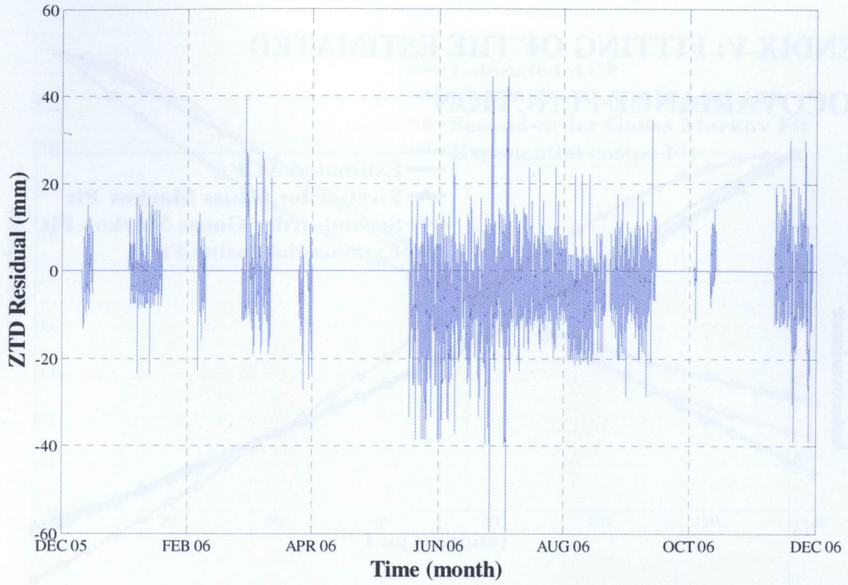

Figure IV.9 NOAA-based residual ZTD at station PRDS over 2006

APPENDIX V: FITTING OF THE ESTIMATED AUTOCOVARIANCE FUNCTION

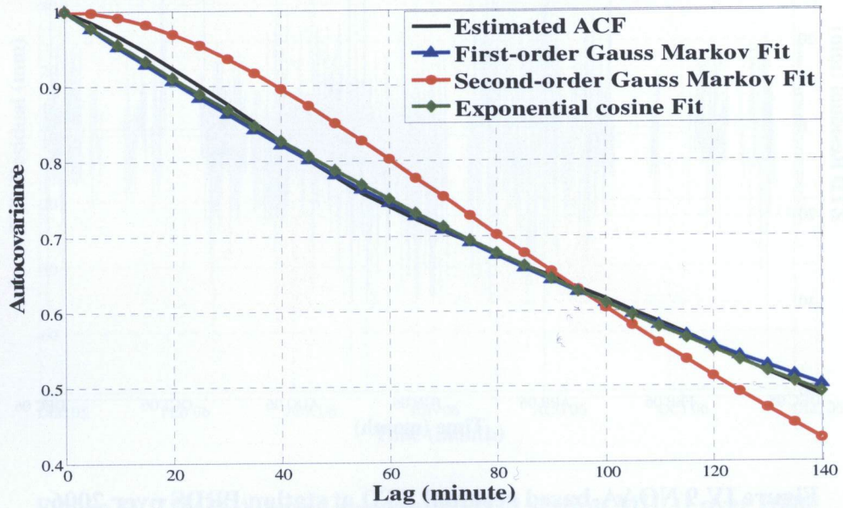

Figure V.1 Fitting of autocovariance of NOAA-based residual at station JPLM on day 215 of 2006

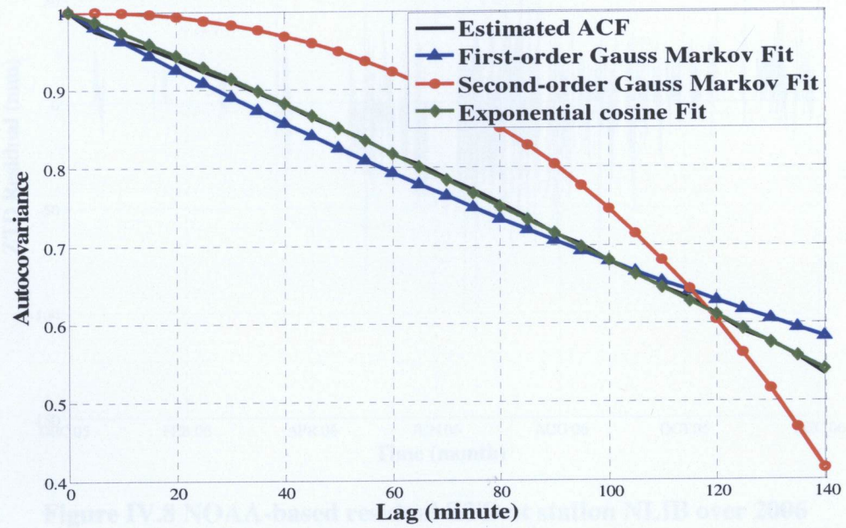

Figure V.2 Fitting of ACF of Hopfield-based residual at station JPLM on day 215 of 2006

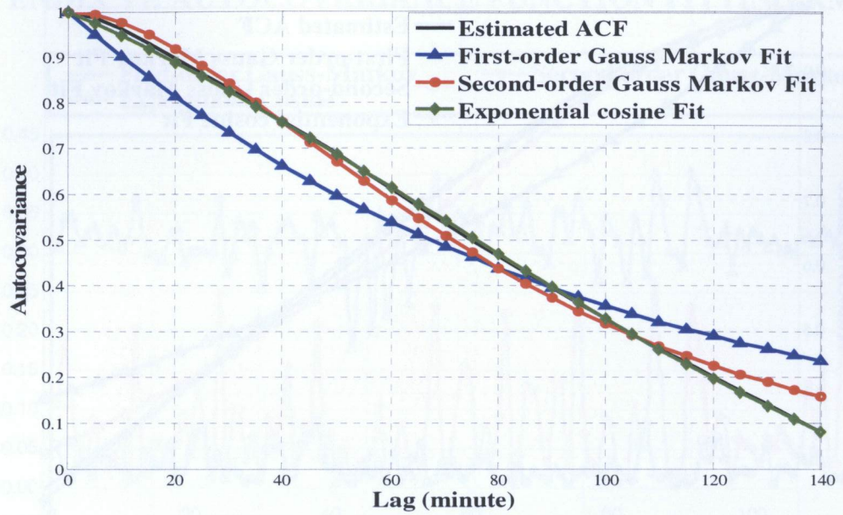

Figure V.3 Fitting of ACF of Hopfield-based residual at station MDO1 on day 45 of 2006

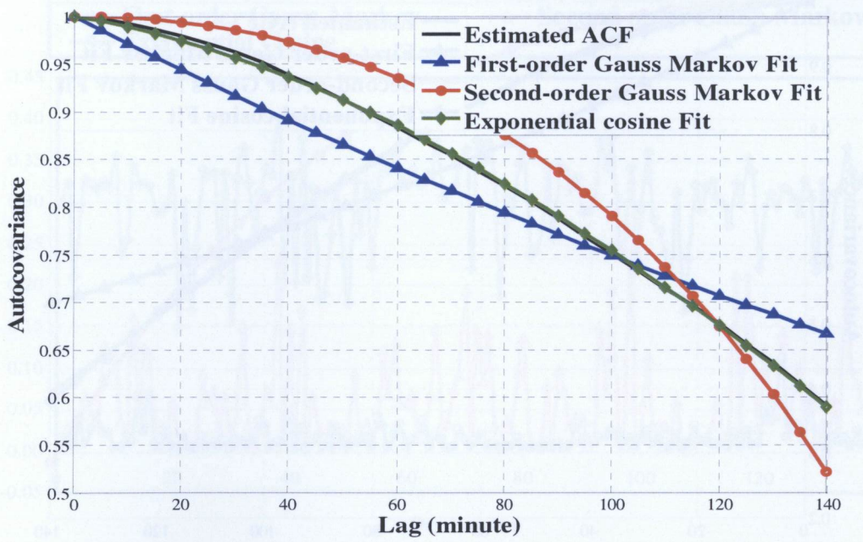

Figure V.4 Fitting of ACF of Saastamoinen-based residual at station USNO on day 180 of 2006

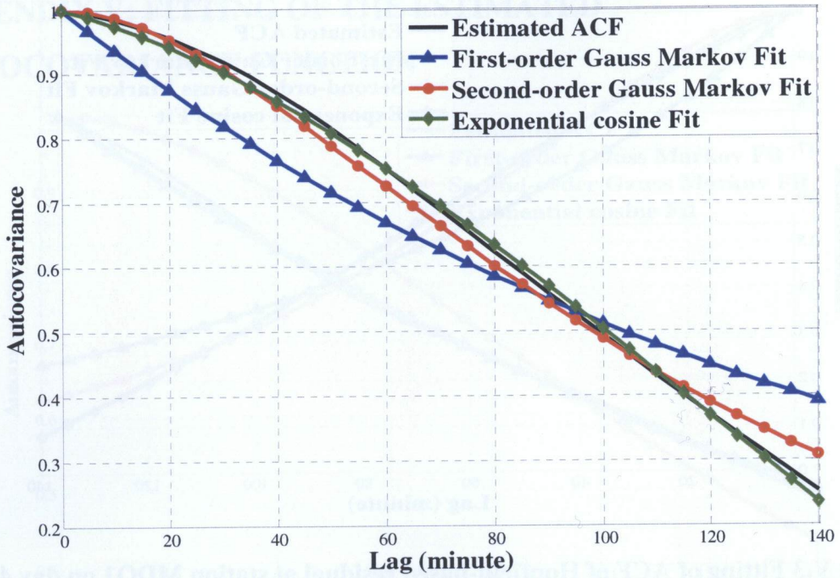

Figure V.5 Fitting of ACF of NOAA-based residual at station HLFX on day 104 of 2006

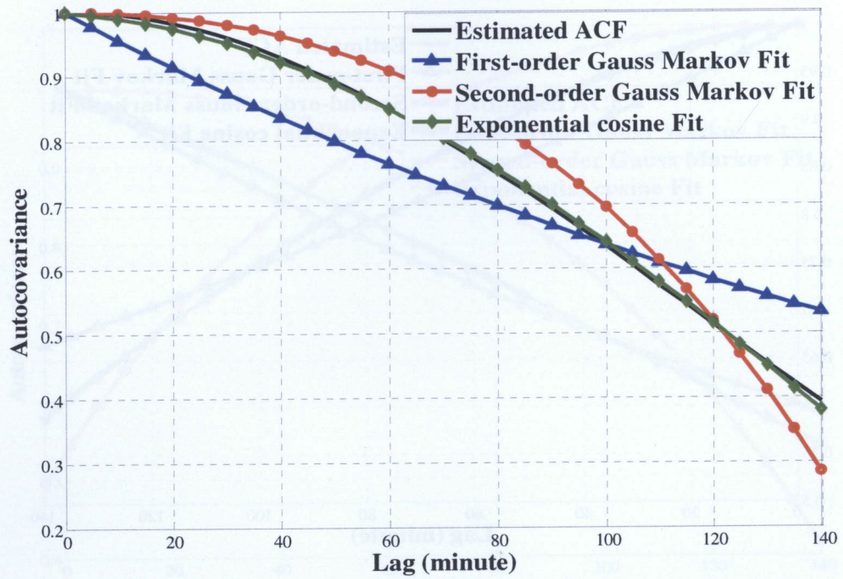

Figure V.6 Fitting of ACF of NOAA-based residual at station HLFX on day 158 of 2006

APPENDIX VI: AUTOCOVARIANCE FUNCTION FITTING RMS

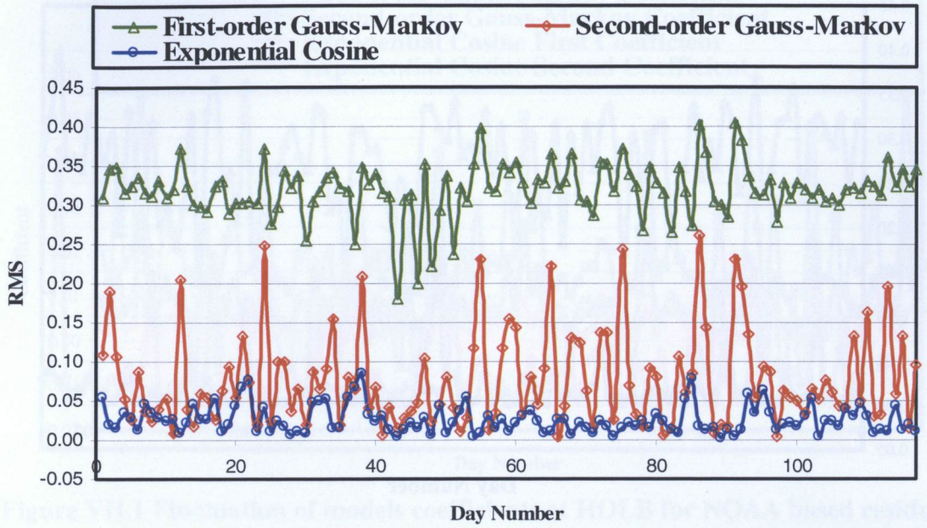

Figure VI.1 Fitting RMS of NOAA-based residual at station AMC2 over 2006

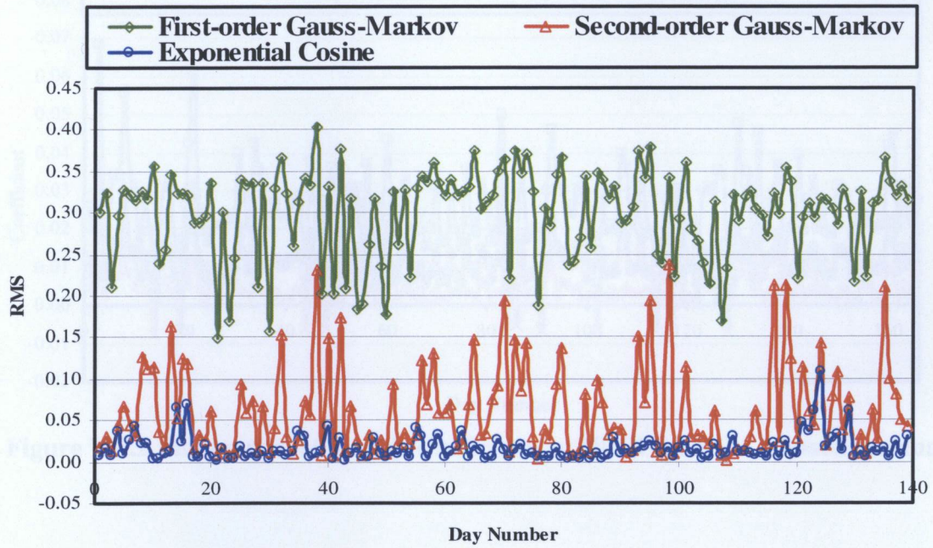

Figure VI.2 Fitting RMS of NOAA-based residual at station FLIN over 2006

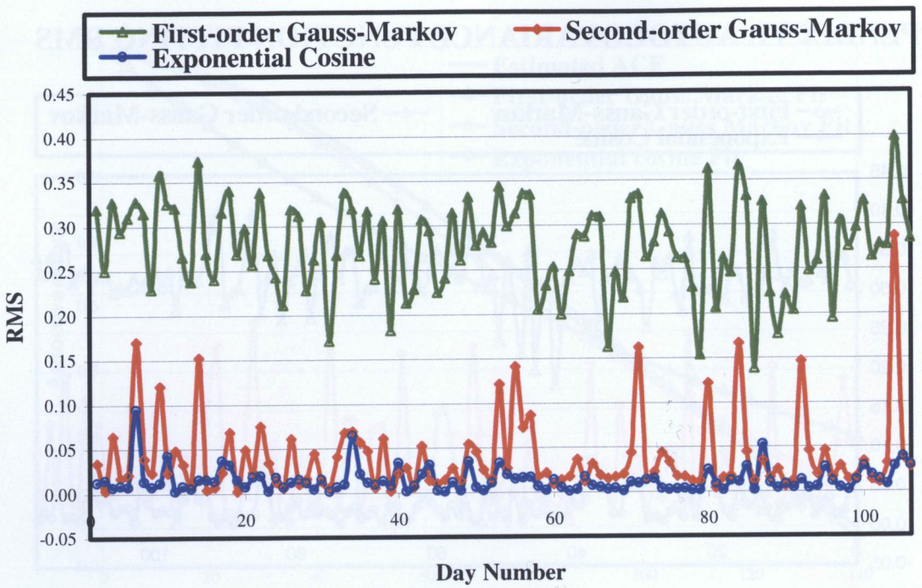

Figure VI.3 Fitting RMS of NOAA-based residual at station FLIN over 2006

APPENDIX VII: FLUNCTUATION OF MODELS' COEFFIEINETS

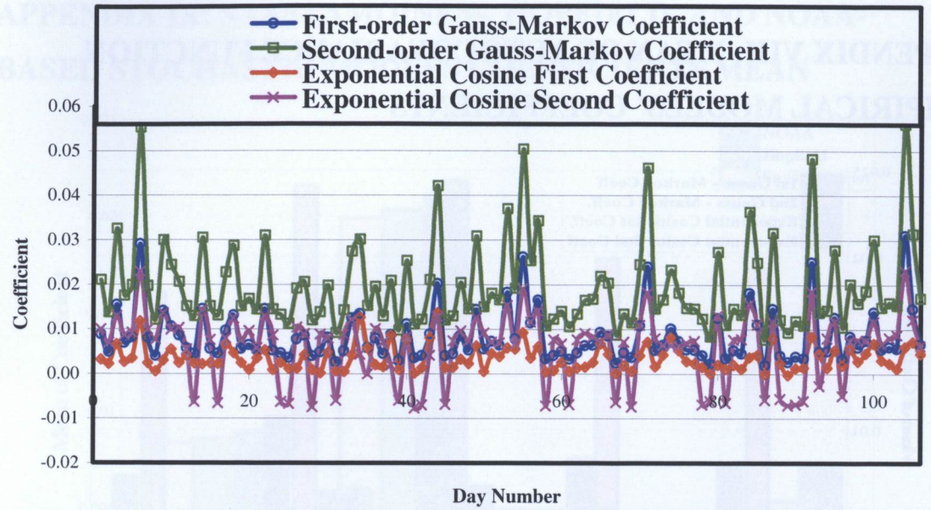

Figure VII.1 Fluctuation of models coefficients at HOLB for NOAA based residual

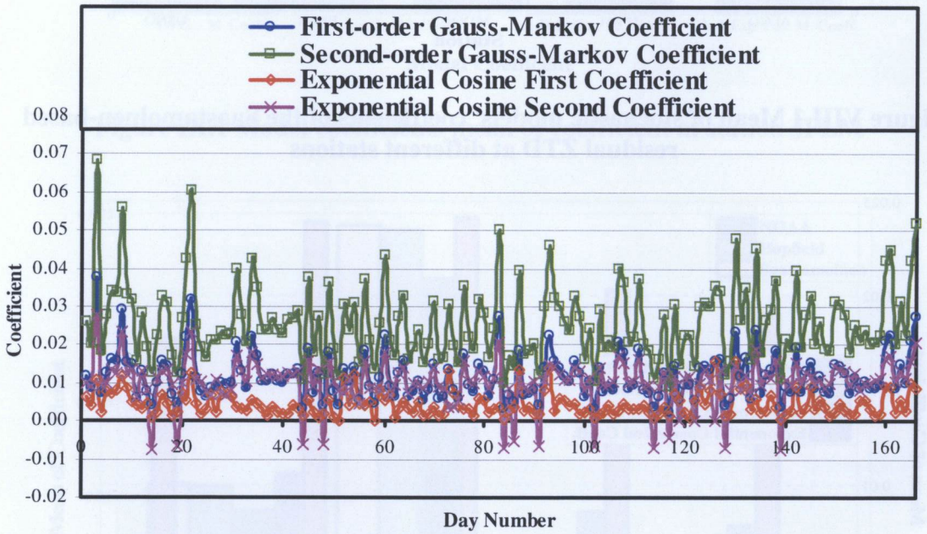

Figure VII.2 Fluctuation of models coefficients at NLIB for NOAA based residual

APPENDIX VIII: MEAN OF AUTOCOVARIANCE FUNCTION EMPIRICAL MODELS' COEFFICIENTS

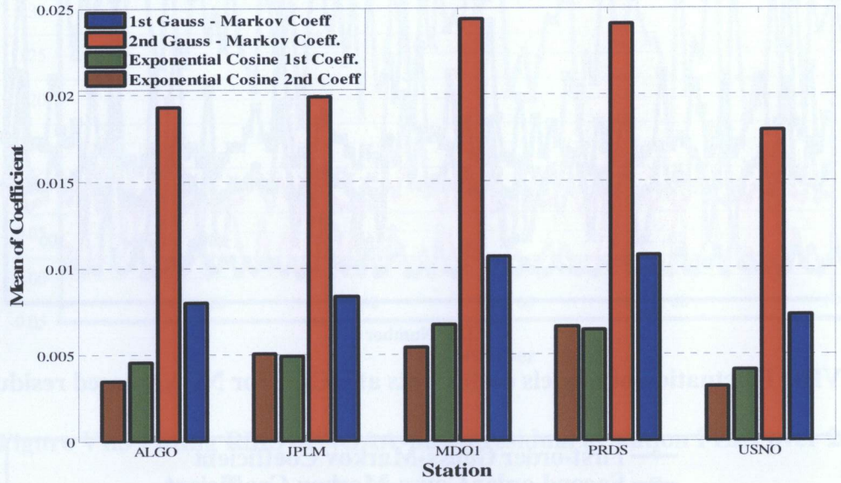

Figure VIII.1 Mean of stochastic models' coefficients of the Saastamoinen-based residual ZTD at different stations

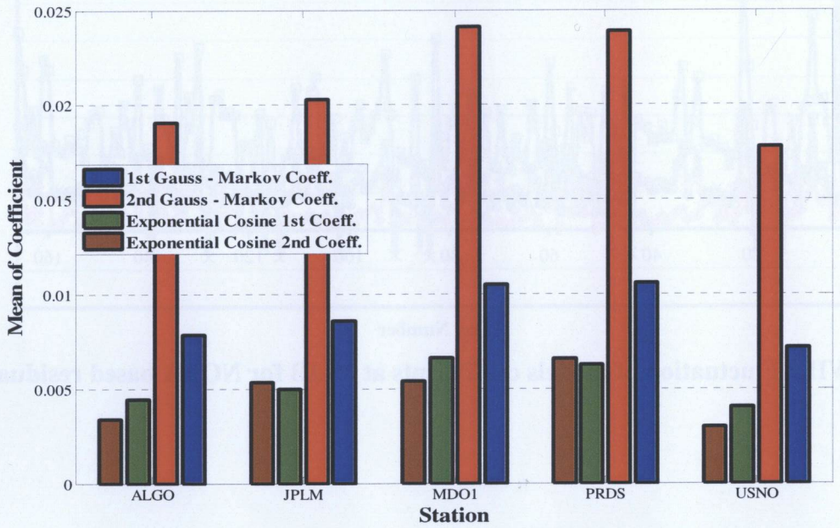

Figure VIII.2 Mean of stochastic models' coefficients of the Hopfield-based residual ZTD at different stations

APPENDIX IX: SAASTAMOINEN-, HOPFIELD- AND NOAA-BASED STOCHASTIC MODLES COEFFICIENTS MEAN

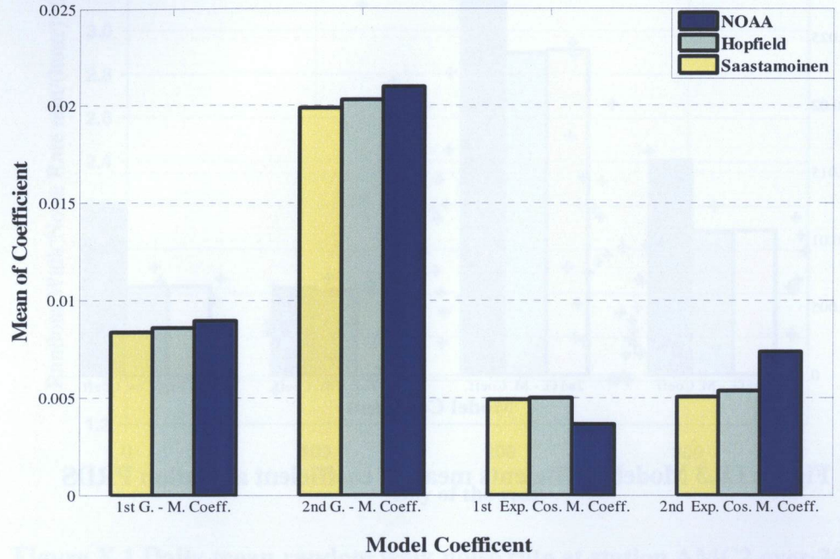

Figure IX.1 Model coefficients mean of coefficient at station JPLM

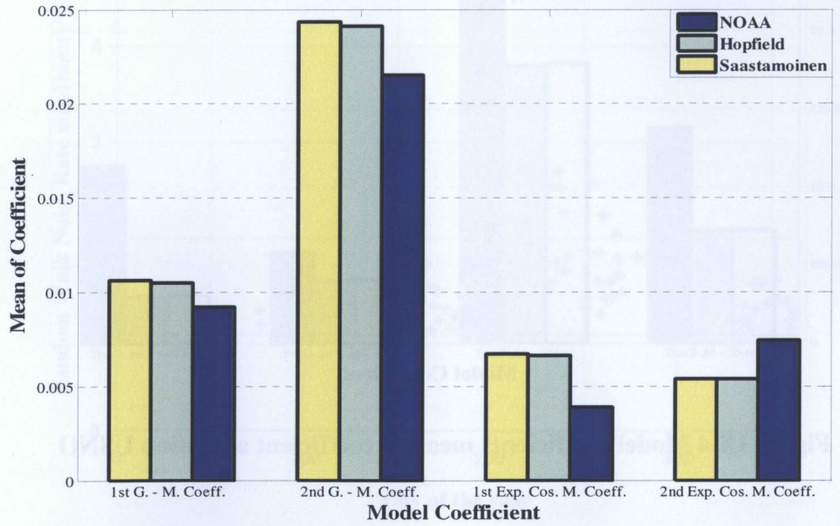

Figure IX.2 Model coefficients mean of coefficient at station MDO1

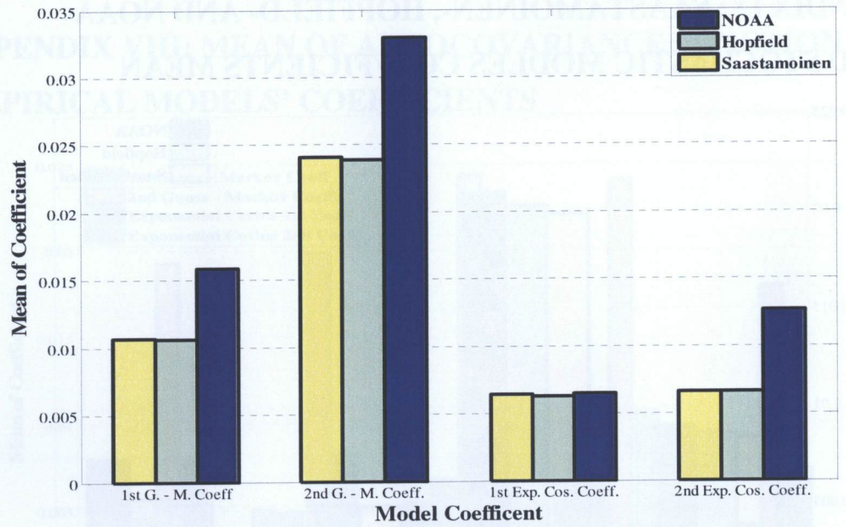

Figure IX.3 Model coefficients mean of coefficient at station PRDS

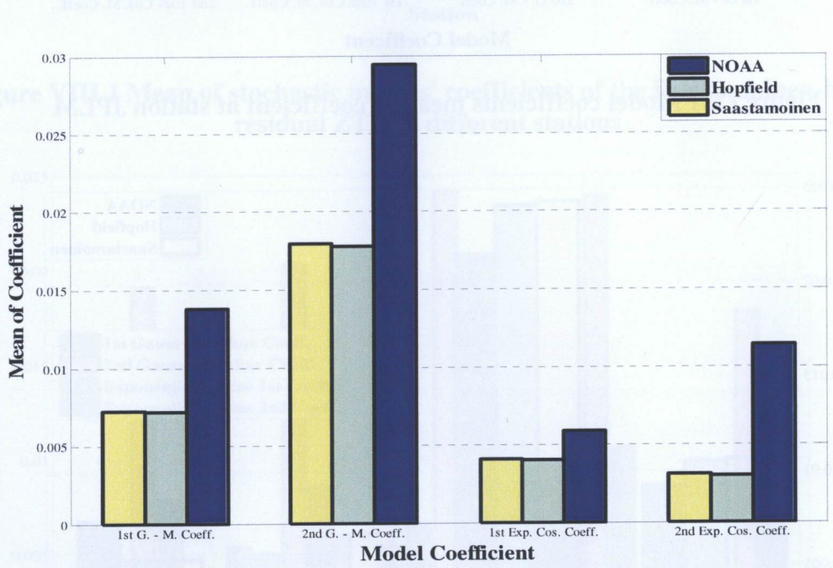

Figure IX.4 Model coefficients mean of coefficient at station USNO

APPENDIX X: DAILY MEAN OF RANDOM WALK NOISE RATE

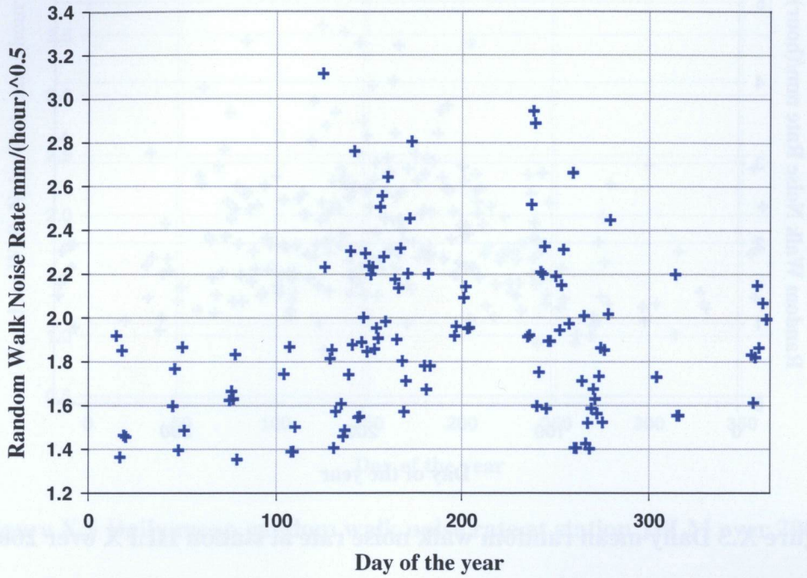

Figure X.1 Daily mean random walk noise rate at station AMC2 over 2006

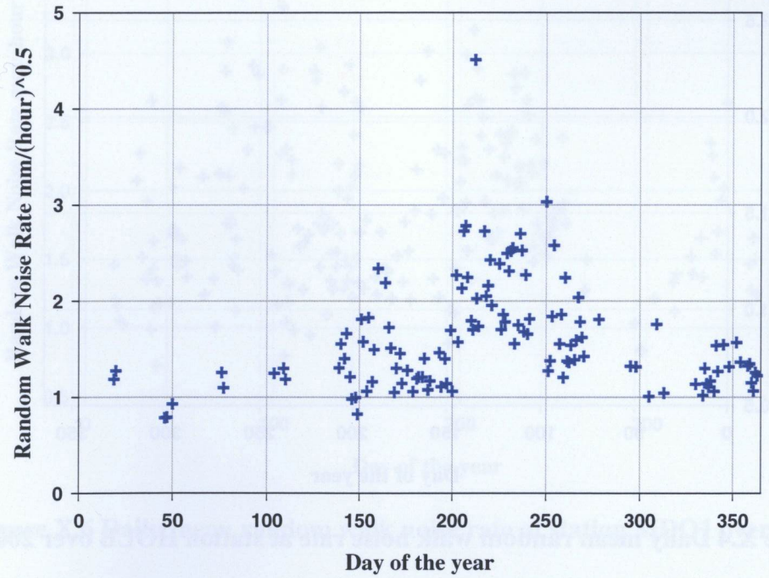

Figure X.2 Daily mean random walk noise rate at station FLIN over 2006

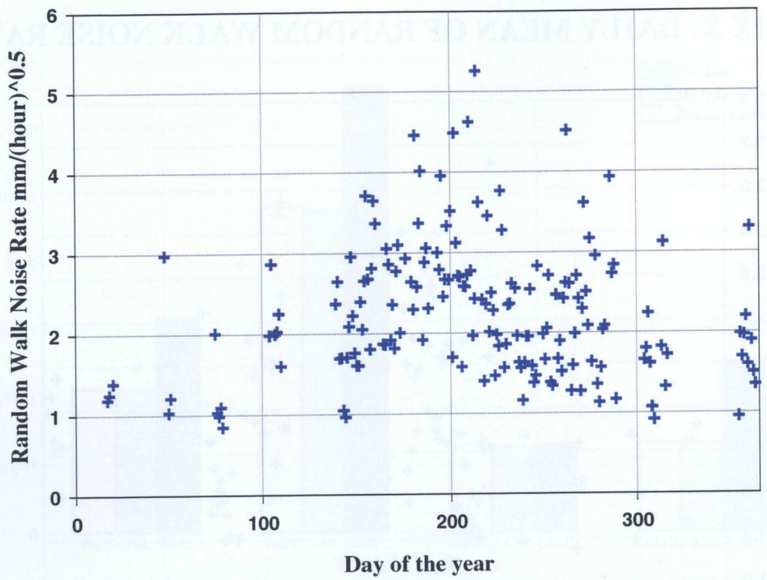

Figure X.3 Daily mean random walk noise rate at station HLFX over 2006

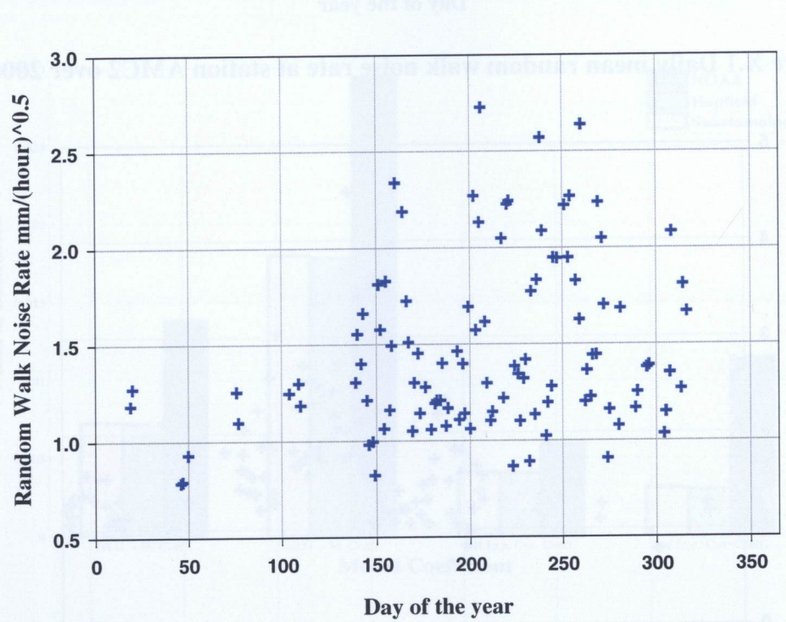

Figure X.4 Daily mean random walk noise rate at station HOLB over 2006

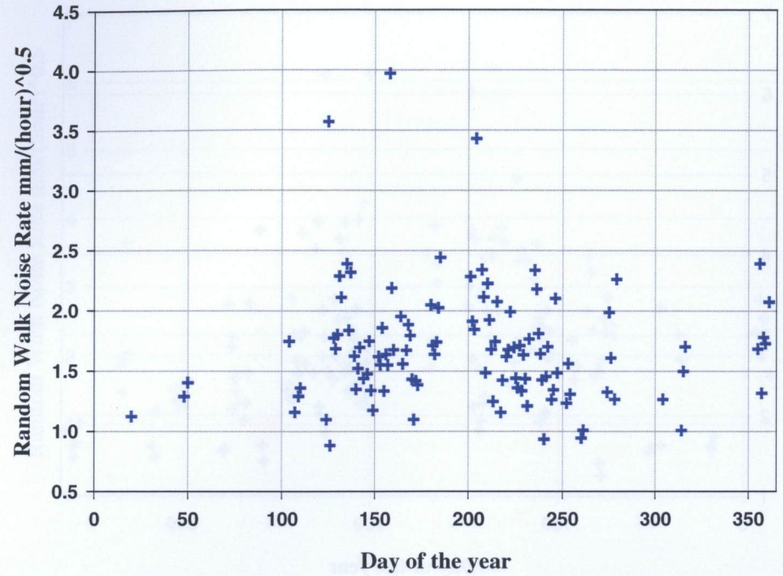

Figure X.5 Daily mean random walk noise rate at station JPLM over 2006

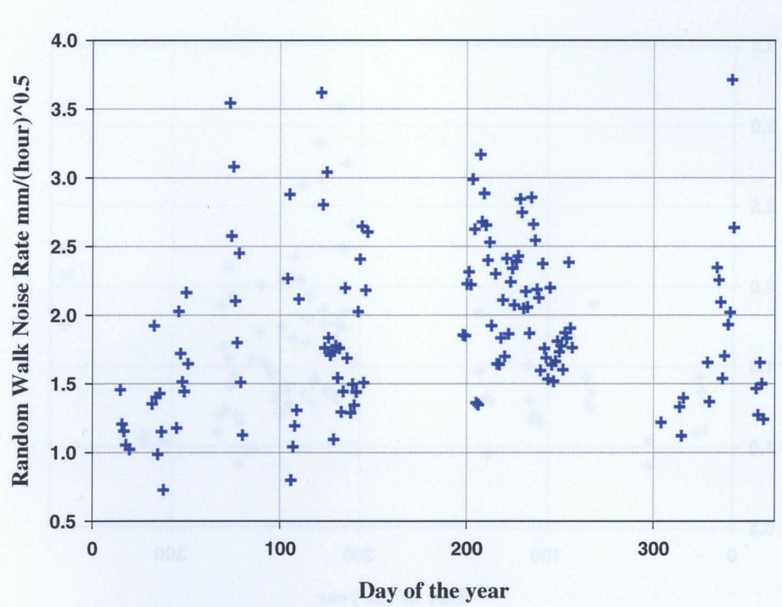

Figure X.6 Daily mean random walk noise rate at station MDO1 over 2006

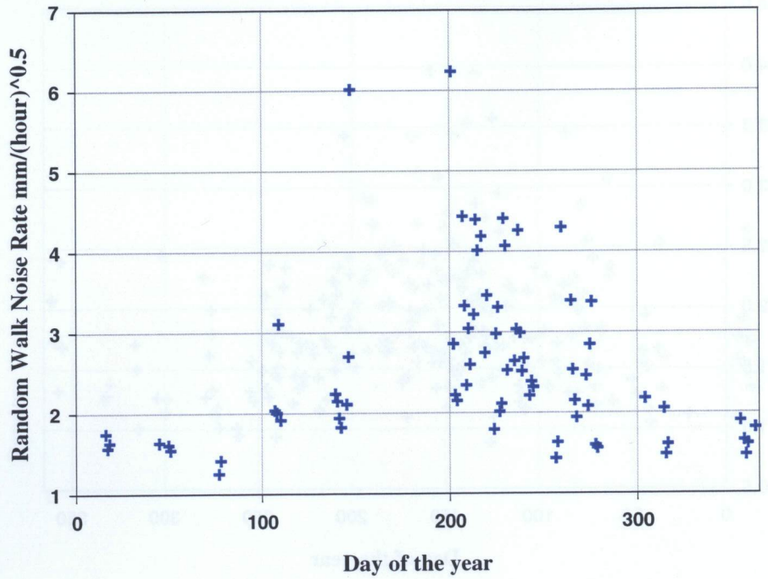

Figure X.7 Daily mean random walk noise rate at station NLIB over 2006

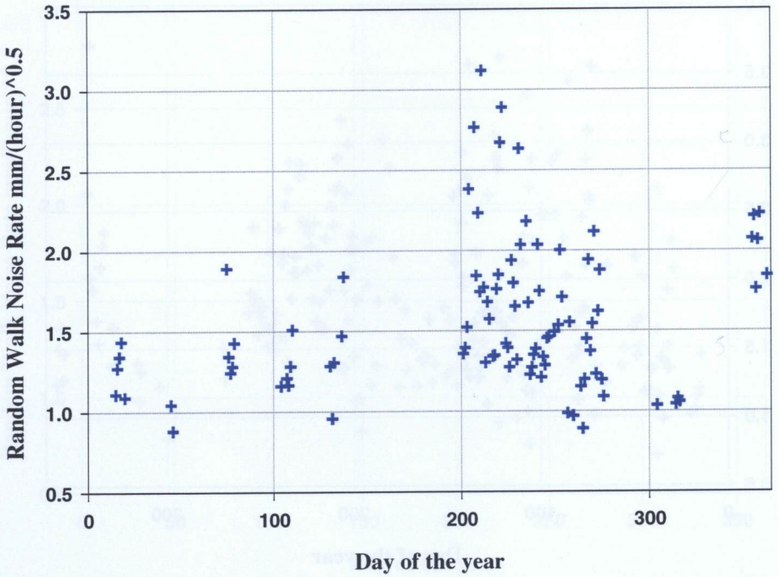

Figure X.8 Daily mean random walk noise rate at station PRDS over 2006

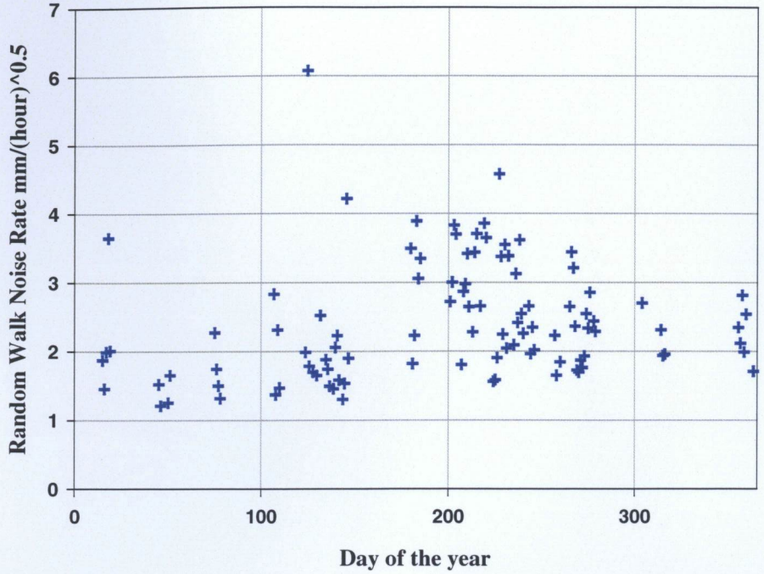

Figure X.9 Daily mean random walk noise rate at station USNO over 2006

Day of the year

Figure X.8 Daily mean random walk noise rate at station PRDS over 2006

Φ Bk-72-5.1